NSWCCD-TR-97/009   14 July 1997

Wall Pressure Signatures of Organized Turbulent Motions

by

Steven J. Russell

19980422 160

DTIC QUALITY INSPECTED 3

Naval Surface Warfare Center
Carderock Division
West Bethesda, Maryland 20817-5700

Wall Pressure Signatures of Organized Turbulent Motions

by

Steven J. Russell

REPORT DOCUMENTATION PAGE

Public reporting burden for this collection of information is estimated to average 1 hour per response, including the time for reviewing instructions, searching existing data sources, gathering and maintaining the data needed, and completing and reviewing the collection of information. Send comments regarding this burden estimate or any other aspect of this collection of information, including suggestions for reducing the burden, to Washington Headquarters Services, Directorate for Information Operations and Reports, 1215 Jefferson Davis Highway, Suite 1204, Arlington, VA 22202-4302, and to the Office of Management and Budget, Paperwork Reduction Project (0704-0188), Washington, DC 20503.

1. AGENCY USE ONLY *(Leave blank)*	2. REPORT DATE	3. REPORT TYPE AND DATES COVERED
	14 July 1997	Final

4. TITLE AND SUBTITLE

Wall Pressure Signatures of Organized Turbulent Motions

5. FUNDING NUMBERS

6. AUTHOR(S)

Steven J Russell

7. PERFORMING ORGANIZATION NAME(S) AND ADDRESS(ES)

Naval Surface Warfare Center
Carderock Division (Code 725)
9500 MacArthur Boulevard
West Bethesda MD 20817-5700

8. PERFORMING ORGANIZATION REPORT NUMBER

NSWCCD-TR-97/009

9. SPONSORING/MONITORING AGENCY NAME(S) AND ADDRESS(ES)

Naval Surface Warfare Center
Carderock Division (Code 725)
9500 MacArthur Boulevard
West Bethesda MD 20817-5700

10. SPONSORING/MONITORING AGENCY REPORT NUMBER

11. SUPPLEMENTARY NOTES

12a. DISTRIBUTION/AVAILABILITY STATEMENT

Approved for public release; distribution is unlimited

12b. DISTRIBUTION CODE

13. ABSTRACT *(Maximum 200 words)*

An extensive database of simultaneously obtained wall pressure and velocity measurements was acquired for a high Reynolds number, equilibrium turbulent flow. These data were obtained in both streamwise and spanwise measurement planes using an array of wall pressure transducers. Analyses of these data were performed to examine the spatial extent and convective features of turbulence producing structures. Several signal processing techniques were shown to extract detailed structural features of the turbulent motions. These techniques included digital band-pass filtering to discriminate between turbulent scales and a localized variance method for the detection of clusters of high frequency turbulent activity. Cross-spectral, cross-correlation, and conditional sampling methods applied to these data clearly show the dynamical relationships between coherent turbulent motions as well as their induced wall pressure signatures. Both pressure-velocity correlation results and conditionally averaged maps of the flow field sampled on peak wall pressure events, reveal a consistent correlation between large scale motions and near-wall, small scale turbulent production activity. The large scale vortical motions (or shear layers) extend across the turbulent boundary layer and exhibit Reynolds stress (turbulent production) characteristics. These findings are consistent with many of the proposed conceptual models of organized motions.

14. SUBJECT TERMS			15. NUMBER OF PAGES
Wall Pressure Fluctuations	Signatures	Organized Motions	204
Hydroacoustics	Turbulence Production		**16. PRICE CODE**

17. SECURITY CLASSIFICATION OF REPORT	18. SECURITY CLASSIFICATION OF THIS PAGE	19. SECURITY CLASSIFICATION OF ABSTRACT	20. LIMITATION OF ABSTRACT
UNCLASSIFIED	UNCLASSIFIED	UNCLASSIFIED	SAR

NSN 7540-01-280-5500

Standard Form 298 (Rev. 2-89)
Prescribed by ANS' Std. Z39-18
298-102

Abstract

An extensive database of simultaneously obtained wall pressure and velocity measurements was acquired for a high Reynolds number, equilibrium turbulent flow. These data were obtained in both streamwise and spanwise measurement planes using an array of wall pressure transducers. Analyses of these data were performed to examine the spatial extent and convective features of turbulence producing structures.

Several signal processing techniques were shown to extract detailed structural features of the turbulent motions. These techniques included digital band-pass filtering to discriminate between turbulent scales and a localized variance method for the detection of clusters of high frequency turbulent activity.

Cross-spectral, cross-correlation, and conditional sampling methods applied to these data clearly show the dynamical relationships between coherent turbulent motions as well as their induced wall pressure signatures. Both pressure-velocity correlation results and conditionally averaged maps of the flow field sampled on peak wall pressure events, reveal a consistent correlation between large scale motions and near-wall, small scale turbulent production activity. The large scale vortical motions (or shear layers) extend across the turbulent boundary layer and exhibit Reynolds stress (turbulent production) characteristics. These findings are consistent with many of the proposed conceptual models of organized motions.

Contents

List of Figures

List of Tables

Nomenclature

a_{ij}, b_{ij}	X-wire calibration coefficients
A, B	King's law constants
C_f	coefficient of skin friction
d	diameter
E	voltage
f	function or frequency, Hz
$\mathcal{F}$	Fourier transform
G	Clauser shape factor, $U_e(H-1)/(u_\tau H)$
H	conventional shape factor, δ^*/θ
K_T	turbulence kinetic energy, $(u_1^2 + u_2^2 + u_3^2)/2$
l	hot wire/X-wire sensing length
n	King's law exponent
N	number of samples
p	fluctuating pressure
R	correlation function
Re_θ	Reynolds number based on momentum thickness
t	time
t_s	digital sampling interval
t_ν	viscous or wall time scale, ν/u_τ^2
T	averaging time or temperature
Δt	event duration
ΔT	time between events
u	fluctuating streamwise velocity
u_i	fluctuating velocity component in the ith direction
u_τ	shear velocity, $(\tau_w/\rho)^{1/2}$
U	mean streamwise velocity
U_c	streamwise convection velocity
U_e	streamwise velocity at boundary-layer edge
U_i	mean velocity component in the ith direction
v	fluctuating wall-normal velocity
V	mean wall-normal velocity
x, y, z	Cartesian coordinates in the streamwise, outward wall-normal, and transverse directions, respectively

δ	boundary-layer thickness, where $U = 0.99U_e$
δ^*	boundary-layer displacement thickness
θ	boundary-layer momentum thickness
k	peak-event detection threshold
ν	kinematic viscosity
ρ	density
τ_w	wall shear stress
Φ	auto or cross spectral density
ω	frequency, rad/s
$\overline{(\ )}$	mean value or time average
D/Dt	substantial derivative, $\frac{\partial}{\partial t} + U_i \frac{\partial}{\partial x_i}$
$(\ )^+$	quantity scaled on wall variables l_ν or t_ν
$\langle\ \rangle$	mean value or ensemble average

Acknowledgements

Throughout this research effort and throughout my academic training, I have received valuable guidance from several individuals. My principal advisor, Dr. Mario Casarella, has generously devoted his valuable time to act as my academic counselor, research advisor, and friend. His contribution to this work, and to my ability to accomplish it, can not be overstated. I am forever indebted to him. I have also had the good fortune of having Dr. Theodore Farabee as my mentor for the past 10 years. His scientific expertise as well as friendly encouragement were critical to my academic and research success. The comments of my readers, Dr. John Gilheany and Dr. Sen Nieh, are also greatly appreciated.

I am also indebted to several individuals whose assistance with the data acquisition and laboratory computer systems allowed me to focus on the experiment and the analysis of the data. Dr. Pablo Penafiel and Mr. Srinath Jayasundera sacrificed many hours of their valuable time to solve problems which would have otherwise halted the progress of this research. I thank you both for your help and your friendship. I am also deeply indebted to Dr. Mark Kammeyer, whose dissertation work laid the groundwork for this investigation and enabled me to "hit the ground running". I would also like to acknowledge the friendly assistance of Mrs. Ruth Hicks who expedited my academic journey for many years.

Ultimately, none of this would have been possible without the patience, love, and understanding of my beautiful wife, Cher, and to my son, Matthew, who went to sleep too many nights without seeing his daddy. I dedicate this work to you both. To my parents and family who encouraged me throughout, I am forever indebted, especially to my sister Michele, whose stylistic recommendations made this document a much better read.

This work was supported by several organizations within the Department of

Chapter 1

INTRODUCTION

1.1 Motivation

When steady fluid flow along the surface of a body changes from laminar to turbulent, the surface becomes subjected to unsteady forces which can induce unwanted structural vibrations. These forces are the result of velocity fluctuations associated with the turbulent boundary layer. The nature of these fluctuating velocities, their origin, scales, locations, etc., have been the subject of both experimental and numerical fluid dynamics research for many years. These efforts have resulted in a limited understanding of the physical processes governing turbulence.

There is a consensus in the turbulence research community that organized motions play a key role in the physics of turbulent flow. Distinct turbulent structures which populate the turbulent boundary layer are believed to originate, in most cases, from near-wall flow eruptions or velocity excursions commonly known as the 'bursting' process. The bursting process is of fundamental importance since it is the inherent mechanism for the production and maintenance of turbulence in wall bounded flows.

Many investigators have also observed that the near-wall burst events, which are intermittent and relatively short in duration, produce large amplitude wall pressure footprints which contribute significantly to the unsteady excitation force on the

surface [26, 25, 44, 46]. The wall pressure footprint of organized turbulent structures, i.e., the spatial and temporal features of the the wall pressure field induced by these structures, has not yet been well established.

At the same time that scientists have been studying the fundamental properties of turbulence, engineers have been developing schemes to minimize turbulence related drag and vibration. Most of the control schemes developed were passive surface modifications (LEBUs, riblets, etc.) aimed at reducing drag. More recent attempts at turbulence control have focused on active techniques (suction/blowing, surface motion, etc.) wherein the boundary layer is acted upon at times determined by a control algorithm to reduce local turbulent activity. These control schemes are based on the detection of turbulence producing, "active" motions[1], and manipulating the flow field to affect or break-up these structures. The most commonly used detection schemes are based on the measurement of shear stress or wall pressure. The wall pressure based schemes require the knowledge of the distinct spatial and temporal characteristics, i.e., the wall pressure signature, of the turbulent structures.

The primary purpose of this experimental investigation is to identify the organized motions related to turbulent production, and to measure the spatial and temporal characteristics of these structures as seen in their wall pressure signatures. The results of this research can serve as a framework for the design of active or adaptive turbulence control systems.

1.2 Background

In this section, an overview of several topics relevant to this investigation is presented. This overview begins with a brief discussion of the criteria imposed to discriminate between "active" and "passive" turbulent structures. This is followed

---

[1]In the literature, those structures directly related to the production process are referred to as 'active' while others are often called 'passive' structures.

by a review of the current "state of the art" in the understanding of the types of structures which inhabit a turbulent boundary layer. Several recently proposed conceptual models for coherent structures are described to establish a foundation for discussion of the experimental results in this investigation. Finally, a brief summary of previous wall pressure research is provided.

1.2.1 Turbulence Production

Since this investigation will focus on organized motions which are involved in the turbulent production process, it is essential that an explicit criterion for turbulent production or "active" motions be established. This is achieved by examining the equation which governs the balance of turbulence kinetic energy. By decomposing the velocity in the ith direction into its mean and fluctuating components, $U_i + u_i$, and substituted it into the Navier-Stokes equations for incompressible flow, the equation for the turbulence kinetic energy $K_T = (u_1^2 + u_2^2 + u_3^2)/2 = u_i u_i/2$ can be obtained as:

$$\frac{D K_T}{Dt} = -\overline{u_i u_j}\frac{\partial U_i}{\partial x_j} - \nu\overline{\frac{\partial u_i}{\partial x_j}\frac{\partial u_i}{\partial x_j}} - \frac{\partial}{\partial x_j}\left[\overline{K_T u_j} + \frac{\overline{p u_j}}{\rho} - \nu\frac{\partial K_T}{\partial x_j}\right]$$

where D/Dt is the substantial derivative, ρ is the density, and p is the fluctuating pressure. Overbars represent time averages. This equation contains three terms which, from left to right, represent turbulent production, viscous dissipation, and turbulence transport (the bracketed terms). The focus of this investigation is the first term, turbulence production, characterized by the interaction of the Reynolds stresses $-\overline{u_i u_j}$ with the mean shear gradient.

For positive turbulent production to occur, the Reynolds stresses $-\overline{u_i u_j}$ must be positive, i.e., the product $u_i u_j$ must be negative. In the flow field studied in this investigation, positive production occurs when $u < 0$, and $v > 0$ or $u > 0, v < 0$, which correspond to the second and fourth quadrants of the u-v plane. These motions

3

are commonly referred to as Q2 and Q4 motions or *ejections* and *sweeps* of fluid. Turbulent motions or "coherent structures" characterized by Reynolds stresses in the Q2 and Q4 quadrants will be considered active motions.

1.2.2 Coherent Structures

Turbulent structures are commonly referred to in the literature as 'coherent structures' or 'organized motions'. Before discussing the current understanding of turbulent structures, it is important to precisely define what is meant by this expression. For this investigation, a general definition for "coherent motions" proposed by Robinson[44] is appropriate since many experimental correlation measurements will be presented. Robinson defined coherent motion as "*a three dimensional region of flow over which at least one fundamental flow variable (velocity component, density, temperature, etc.) exhibits significant correlation with itself or with another variable over a range of space and or time that is significantly larger than the smallest local scales of the flow.*"

In Robinson's review article, he compiled a thorough summary of types of turbulent structures identified experimentally and numerically by the turbulence community in the last 40 years. He divided these structures into eight categories:

1. Low speed streaks in the viscous sublayer.

2. Lifting and ejection of these streaks.

3. Subsequent sweep of high speed fluid inward.

4. Vortical structures of varying form.

5. Sloped near-wall shear layers with high spanwise vorticity.

6. Near wall pockets swept clean of marker fluid (splats).

4

7. δ-scale motions capped by the inner/outer interface.

8. Shear layer backs of these motions.

It is important to note that these structures are not only intermittent in time, but also different in size and shape, depending on their location relative to the wall.

Two fundamental questions that have challenged researchers are: which of these inner and outer layer structures play the dominant role in the physical mechanism governing turbulence, and to what extent do these structures interact during these production and maintenance processes? These questions are the subject of much controversy. Many investigators have proposed models for the turbulence production process in which some of these structures interact collectively. Nearly every model involves several of the structures listed above. Despite the controversy over what role these structures play in the turbulence production process, there is a general consensus in the turbulence community about the presence of these coherent motions. Robinson summarizes what he believes to be the "knowns" concerning coherent motions:

- The majority of turbulence production occurs in the near wall "buffer" region during violent outward ejections of low speed fluid (bursts) and during inrushes of high speed fluid toward the wall (sweeps).

- Horseshoe or hairpin-like vortices are embedded in the turbulent boundary layer and are believed to be critical in the turbulence production cycle and in momentum transport between the inner and outer layers.

- Three dimensional bulges in the outer region form the boundary between the turbulent and non-turbulent regions of the flow. High speed fluid impacting the upstream sides of these large scale motions form sloping δ-scale shear layers (backs).

5

- Outer layer structures have a (Reynolds number dependent) modulating influence on near wall events.

From the standpoint of controlling turbulence, knowledge of the dynamic features of the active structures is critical. The fact that nearly 80 percent of turbulence energy is produced during the quasi-periodic burst/sweep events [54] makes disrupting this process the key to active control. It is also believed that these burst/sweep events are self-regenerating, suggesting that to disrupt one event might affect future events. Breaking this chain of events will require a scheme for detecting the onset of a turbulent production event. As stated earlier, shear stress and wall pressure have shown promise as the turbulent properties to measure, however, the small (temporal and spatial) scales associated with the near wall production events make even the smallest micro-sensors look large, especially at high Reynolds number. If a link could be established between the near wall, turbulent production events and other larger scale structures in the outer flow (shear layers, backs, etc.) then detection of the large scale structures could pinpoint turbulent production events.

In summary, the central issues in understanding turbulence can be restated as the interaction between the inner and outer layer structures of the boundary layer, and their causal relationship in the turbulence production process. Kline and Robinson [29] summarize the three most commonly argued points of view on these issues:

- Outer-dominant, in which the inner layers are driven by fluctuations in the outer layer (not widely accepted).

- Wall-dominant, in which energetic actions including most of the turbulence production occur in the inner layer and hence the outer layers are merely collections of "tired" turbulence diffused outward from events near the wall.

6

- A third view in which the two layers interact so that both are important in the totality of structures which occur in the boundary layer.

The third view, a compromise between the first two, is gaining popularity as the complexity of the turbulence production process is continuously revealed in new research utilizing a broad range of flow visualization and quantitative measurement techniques.

1.2.3 Conceptual Models

Many researchers have proposed models which describe the kinematic and dynamic processes of turbulence. Theodorsen [49] first proposed a horseshoe or hairpin-like vortex model based on the vorticity transport form of the Navier-Stokes equations. Willmarth and Tu [55] proposed a model for the average near wall eddy structure based on space time correlations between wall pressure and velocity. Again, the hairpin vortex was the dominant theme; however, they extended the influence of the vortex to the outer edge of the boundary layer. Offen and Kline [38], Hinze [20], and many others suggested similar models based on the lift up and ejection of horseshoe-like vortical structures in the near wall region of the turbulent boundary layer. A relationship between coherent outer motions and the near wall turbulence production was presented by Praturi and Brodkey [42] where near wall ejections were induced by the passage of δ-scale shear layers. Falco [15] also suggested that large scale outer structures affect but do not govern near wall production.

The work of Thomas and Bull [50] has served as a basis for many recently proposed models. Using both shear stress and wall pressure as a detector of near wall burst/sweep motion, Thomas and Bull demonstrated that near wall, high frequency activities were associated with the passage of large scale organized flow structures (an inclined shear layer, See figure 1.1). Although unable to show what triggered

7
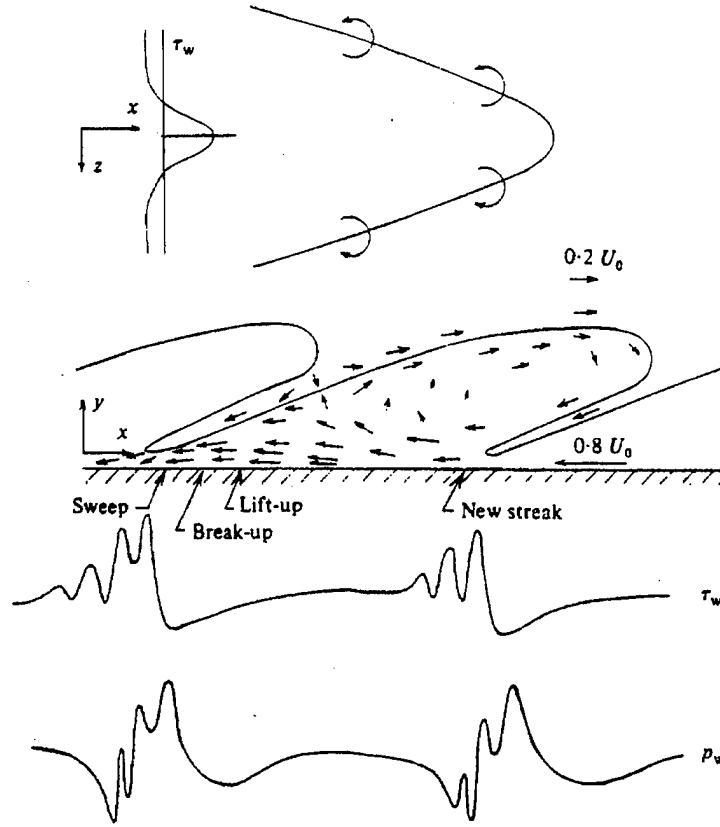
Figure 1.1: Large scale structure associated with the burst-sweep cycle and corresponding wall shear and wall pressure distributions. From Thomas and Bull (1983)

the near wall event, Thomas and Bull did rule out the pressure pattern of the passing large scale structures. Correlating large and small scale turbulent motions by filtering pressure and velocity data was a feature of their work. This aspect of their investigation motivated some of the filtering techniques used in the present investigation.

Valuable insight on turbulent structures has been obtained from the direct numerical simulation (DNS) studies on turbulence in a low Reynolds number (R_θ=1410) flat plate boundary layer by Spalart [47]. Kline (1992AFOSR) reviewed the overall results of DNS studies and found that two types of vortices are found to be "central structures":

- inner layer: tilted streamwise vortices (legs)

- outer layer: transverse vortices (heads)

The two forms overlap in the log-law region of the boundary layer. Kline further concluded that these structures are strongly related to the production process. Robinson [43] had earlier proposed a model consistent with these findings. It is based on hairpin-like vortices in which both streamwise and arch-like structures exist together, sometimes as part of the same vortical structure (See figure 1.2). Robinson attributes most of the eight structures listed earlier to these vortical structures, including the δ-scale shear layers.

Choi [11] attempted to combine all the ingredients of near wall turbulence mentioned above into a universal model (See figure 1.3). His model accounts for the regenerative property of turbulence through the interaction of near wall "bursts" and near wall transverse vortical filaments. Choi proposed that the counter-rotating legs of hairpin-like vortices generate the near wall burst by introducing high momentum fluid into the near wall region (stage 1), as a result, an upstream transverse vortex filament is lifted and stretched (stage 2) and ejected (stage 3).

Many other models with similar features have been proposed by Kovasnay [31], Laufer [34], Blackwelder & Eckelmann [4], Dinkelacker [13], Wallace [51], Fieldler [18], Adrian [1], Jimenez [23] and Kobashi & Ichijo [30]. Nonetheless, this brief survey illustrates a common theme; that is, sweeps and ejections play significant roles in maintaining turbulence and that hairpin-like vortices appear to be the dominant structures. An active control scheme that can disrupt this process will require the detection of oncoming burst/sweep events in the flow field. The wall pressure signature of these events may be used as a "detector function" if a pressure model could be adequately defined.
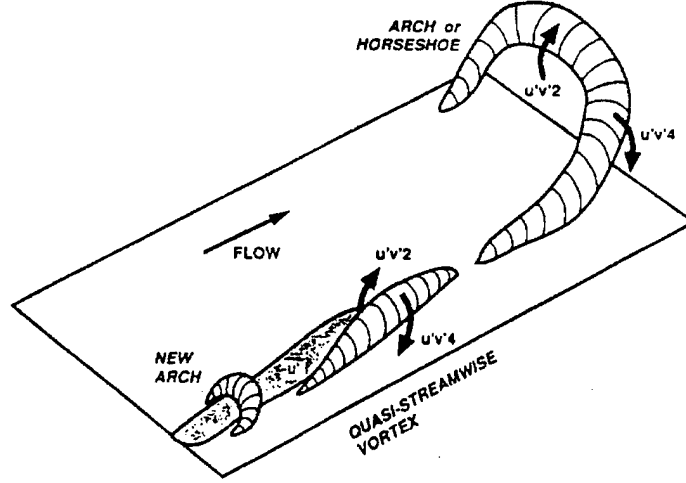
Figure 1.2: Conceptual model of the kinematical relationships between (1) ejection/sweep motions and quasi-streamwise vortices in the near wall and (2) ejection/sweep motions and arch-shaped vortical structures in the outer region. From Robinson (1991)

1.2.4 Wall Pressure Signatures

In an incompressible turbulent boundary layer, pressure fluctuations are caused by fluctuations of velocity. This relationship is governed by the Poisson Equation:

$$\frac{\partial^2 p}{\partial x_i^2} = -\rho \left[2\frac{\partial U_i}{\partial x_j}\frac{\partial u_j}{\partial x_i} + \frac{\partial^2}{\partial x_i \partial x_j}\left(u_i u_j - \overline{u_i u_j}\right) \right].$$

The right hand side of this equation indicates two sources of pressure fluctuations. The first term is the linear interaction of the mean shear $\left(\frac{\partial U_i}{\partial x_j}\right)$ with turbulence $\left(\frac{\partial u_j}{\partial x_i}\right)$. The second term is the non-linear interaction of turbulence with turbulence. The fluctuating pressure at the wall would be obtained by integrating the Poisson equation over the entire flow field. Turbulent sources of all scales throughout the flow field contribute to the wall pressure.

Farabee [16] studied the wall pressure field downstream of a surface disturbance. Based on scaling laws and spectral measurements, Farabee showed that the high-frequency pressure fluctuations were associated exclusively with sources near the wall. Farabee also demonstrated the influence of large scale, outer layer disturbances

Vortex filament

Near-wall
bursts

Stage 1

Flow

Stage 2

Ejection

Low-speed
region

Near-wall
bursts

Stage 3
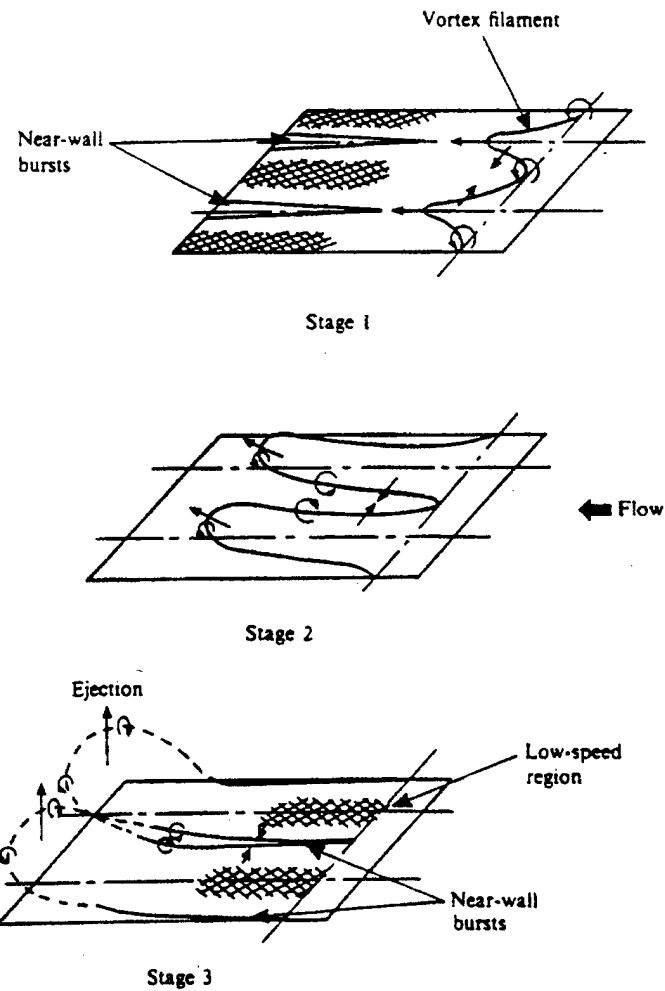
Figure 1.3: Conceptual model for the near wall turbulence activities of the boundary layer. From Choi (1996)

on the low frequency pressure fluctuations as well as the value of the RMS wall pressure. By correlating high pass and low pass filtered pressure and velocity data, Kobashi and Ichiho [30] also showed the location of high frequency pressure sources to be in the near wall region. They found that the low frequency sources correlated across the entire boundary layer.

Karangelen [26] explored the temporal, statistical, and spectral features of the wall pressure fluctuations in an equilibrium turbulent boundary layer. The fluctuating wall pressure was found to exhibit Gaussian-like behavior, zero mean and skewness close to zero, however, the distribution was decidedly non-Gaussian when examining higher moments. Karangelen's spectral results confirmed Farabee's findings regarding the inner/outer scaling as well as the cross spectral (convection velocity) behavior of the wall pressure spectrum. Karangelen's temporal analysis of large amplitude events also showed the dominance of these intermittent events on the RMS wall pressure. The average duration and time between events confirmed that large amplitude pressure events are footprints of the near-wall bursting cycle.

Wilczynski [53] carried Karangelen's analysis further by correlating wall pressure events with turbulent structures throughout the boundary layer. Through various signal processing and conditional sampling techniques, he was able to identify many of the turbulent structures classified by Kline and Robinson [29], as well as to correlate velocity events with wall pressure events. Wilczynski concluded that in the near-wall bursting process, ejections of low speed fluid were associated with local, temporal increases in the wall pressure, and that sweeps were associated with decreases in wall pressure. From his results, he proposed a model for the localized wall pressure footprint of the bursting process, suggesting that positive and negative pressure events as well as the oscillations that precede and follow them are often components of the ejection/sweep, or burst cycle (See figure 1.4). Johannson, Her,

12
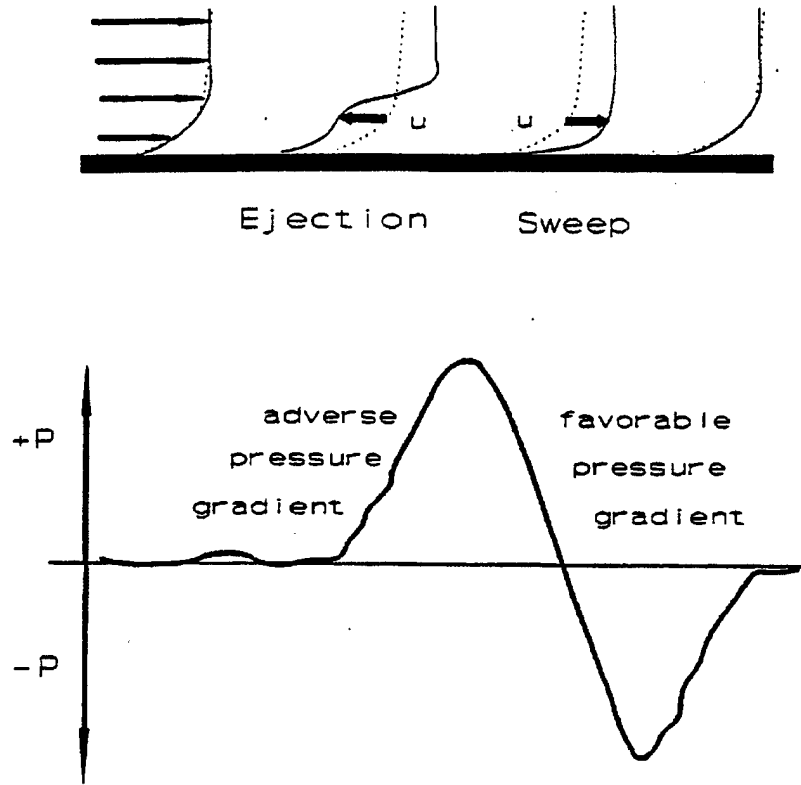
Figure 1.4: The wall pressure signature during the bursting process. From Wilczynski (1992)

and Haritonidis [24] also found that negative wall pressure peaks were associated with sweep-like motions.

By sampling wall pressure during periods of large $\partial u/\partial y$, Astolfi and Forestier [2] identified a wall pressure footprint associated with the passage of an inclined shear layer, similar to the model proposed by Wilczynski [53]. Their shear layer was preceded and followed by ejection and sweep like motions, respectively. Thomas and Bull [50] identified a similar shear layer with a pressure signature as shown in figure 1.1. At about the same time that Thomas & Bull's results were published, Schewe [45] was experimenting with an array of pressure transducers. Schewe was able to visually track pressure producing structures in time records and attributed

them to sources near the wall ($y^+ \leq 21$). Schewe also demonstrated the effectiveness of conditional sampling and averaging the array signals to measure the convection velocity of the structures. Schewe's success with an array of pressure transducers encouraged the use of an array in the present investigation, and his results will serve as a benchmark for some of the data being presented.

Kammeyer [25] examined the flow field associated with large amplitude wall pressure events using signal processing techniques such as wavelet filtering, and conditional sampling on clusters of events. Kammeyer observed the presence of an inclined vortical structure associated with large amplitude pressure events, similar to the findings of other investigators. The work by Kammeyer on flow structures and associated wall pressure events was quite promising and served as the framework for the analyses used in this investigation.

Structures associated with turbulence production, their movement, and interaction, have been demonstrated to impart a pressure signature at the wall. Unfortunately, passive structures (those not directly associated with production) also induce fluctuating wall pressures. Discrimination between the pressure signatures of active and passive structures will be necessary in any successful control scheme and this will inevitably require an understanding of their physical characteristics. The ability to track the active structures and to discriminate them from background turbulence is the major challenge of this research.

1.3   Objectives and Outline of Dissertation

The major goal of this research is to clarify the unresolved issues discussed above concerning the causality between organized motions and wall pressure fluctuations. To achieve this goal, new experiments were performed using an array of pressure transducers. The analyses of the acquired data will require a range of signal pro-

cessing techniques and the results can then provide the framework for validating or disproving many of the hypotheses regarding turbulent structures and their wall pressure signatures.

There are three fundamental objectives of the investigation:

1. To identify and discriminate the active structures from the passive structures in the turbulent boundary layer,

2. To demonstrate that the active structures can be tracked with an array of wall pressure transducers,

3. To obtain the 'total' wall pressure signature of the combined small and large scale turbulent-producing structures.

The detailed features of the total signature should include the streamwise and spanwise extent of the wall pressure signatures as well as the convective properties of the flow structures.

In Chapters 2 and 3 of this dissertation, the experiments performed and signal processing techniques employed to achieve these objectives are described. A transducer array was designed and built to enable the measurement of the streamwise and spanwise features of the wall pressure field. Digital band pass filtering was used to isolate selected frequency bands in the wall pressure and velocity spectra. The filters were designed based on results of previous investigators [16, 25] which showed certain frequency regions to be associated with near wall turbulent structures and other frequency regions to be associated with large scale outer layer activity.

Two distinct sets of experiments were performed using the transducer array:

1. Simultaneous wall pressure measurements from an eight element array, oriented both in the streamwise and spanwise directions.

2. Wall pressure measured from the array simultaneously with hot-wire velocity measurements throughout the boundary layer.

In Chapter 4, the results of the first set of experiments are presented. Here, the challenges of discriminating and tracking active and passive structures are first explored. The spatial extent of the wall pressure events as well as their convective properties are also examined. Using cross-correlation, and conditional sampling and averaging, the correlation between small scale and large scale wall pressure events is demonstrated. In the second set of experiments, flow structures associated with the wall pressure events are captured using cross-correlation as well as conditional sampling techniques. These results are presented in Chapter 5. Correlation between small and large scale structures is further demonstrated in the ensemble averaged flow field measurements. Chapter 6 contains a summary of the overall findings of this investigation followed by a discussion of its accomplishments and possible directions for future research.

Chapter 2

EXPERIMENTAL ARRANGEMENT AND TEST CONDITIONS

2.1 Experimental Facility and Instrumentation

2.1.1 The Wind Tunnel

The experiments in this investigation were conducted in the Catholic University of America (CUA) Low Noise Flow Facility shown schematically in figure 2.1. Features of the wind tunnel include a 16:1 contraction section preceded by a series of turbulence management screens, a 2.4 meter long square profile test section measuring 0.6 meters a side, and an acoustically treated 7° diffuser section. The tunnel is equipped with a low speed centrifugal blower driven by a 20 hp dc motor and acoustic mufflers are located upstream and downstream of the blower.

The facility was originally designed for the purpose of making wall pressure and velocity measurements in a low background noise environment. As described in Farabee [16], at a flow speed of approximately 15 m/s, the facility acoustic performance is excellent at frequencies above 50 Hz. Below 50 Hz, wall pressure signals are contaminated by blower generated acoustic standing waves. The tunnel itself can be operated at flow speeds between 3 and 30 m/s. The free stream turbulence
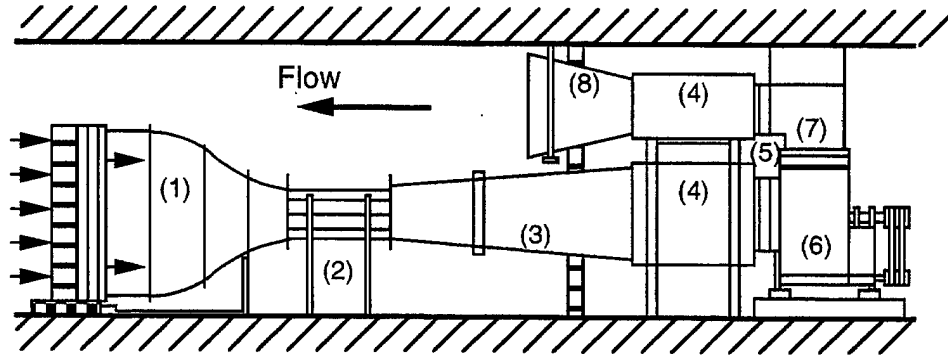
Figure 2.1: CUA Low Noise Flow Facility features (1) inlet section (2) test section (3) diffuser (4) muffler (5) coupler (6) blower/motor (7) turn vanes (8) return duct

Table 2.1: Summary of CUA Low Noise Flow Facility TBL characteristics (from Wilczynski 92)

U_0(m/s)	δ (cm)	δ^* (cm)	θ (cm)	u_τ/U_0	R_θ	δ^+
15.5	2.67	0.41	0.28	0.041	2945	1221
24.6	2.36	0.38	0.25	0.039	4431	1546

intensity level is approximately 0.2 %. Typical turbulent boundary layer (TBL) characteristics as measured by Wilczynski [53] near the midpoint of the test section at two tunnel speeds are shown in table 2.1.

All experiments in this investigation were conducted with an equilibrium turbulent boundary layer and a free stream velocity of approximately 16 m/s (50 ft/s). Detailed boundary layer characteristics are given in Section 2.3.

2.1.2   Instrumentation and Data Acquisition

The freestream velocity during all experiments was monitored using a test cell Pitot-static probe. The probe output was measured with an Edwards High Vacuum, 10 torr differential pressure transducer and Datametrics model 1174 electronic manometer. Atmospheric pressure and temperature were monitored using a Welch Scientific mercury barometer and thermometer. Atmospheric density was then computed with the perfect gas law for use in Pitot-static calibration. Free stream velocity was

computed with the measured Pitot-static difference and the calculated atmospheric density using Bernoulli's equation.

A schematic of the entire facility instrumentation is given in figure 2.2. Wall pressure measurements were made using Endevco model 8507-C2 piezo-resistive pressure transducers, which are described in detail in Section 2.2. The pressure transducers were powered with an Endevco model 109 power supply and the output signals were conditioned using four 2-channel model 106 piezo-resistive conditioners. The output of the signal conditioners was amplified by Ithaco model 451 inverting amplifiers with 20 dB gain with its built-in high pass filters set to a cutoff frequency of 1 Hz. Velocity measurements were made with a constant temperature anemometer (CTA) system. As depicted in figure 2.2, this system was comprised of the following components:

- TSI type 1261 A-T1.5 boundary layer probe or
- TSI type 1249 A-10 miniature cross-wire probe
- TSI model 1155 probe support
- DISA type 55M10 CTA standard bridge in type 55M01 main units
- DISA type 55M25 linearizers
- TSI type 1015C Correlator

Boundary layer characteristics were measured using a TSI type 1261 A-T1.5 miniature boundary layer probe. This probe had a single tungsten wire of length 1.52mm (active sensing length of 1.27 mm) and 0.0038 mm diameter. All two-component velocity measurements were made with a TSI type 1249 A-10 miniature "X" probe. The X probe consisted of two ceramic wires with a deposited platinum film. Each wire had an overall length of 1.27 mm (active sensing length of 0.51 mm) and a diameter of 0.0025 mm. The measurement volume of the cross-wire system was limited by the 1 mm separation distance between the two wires. The hot-wire
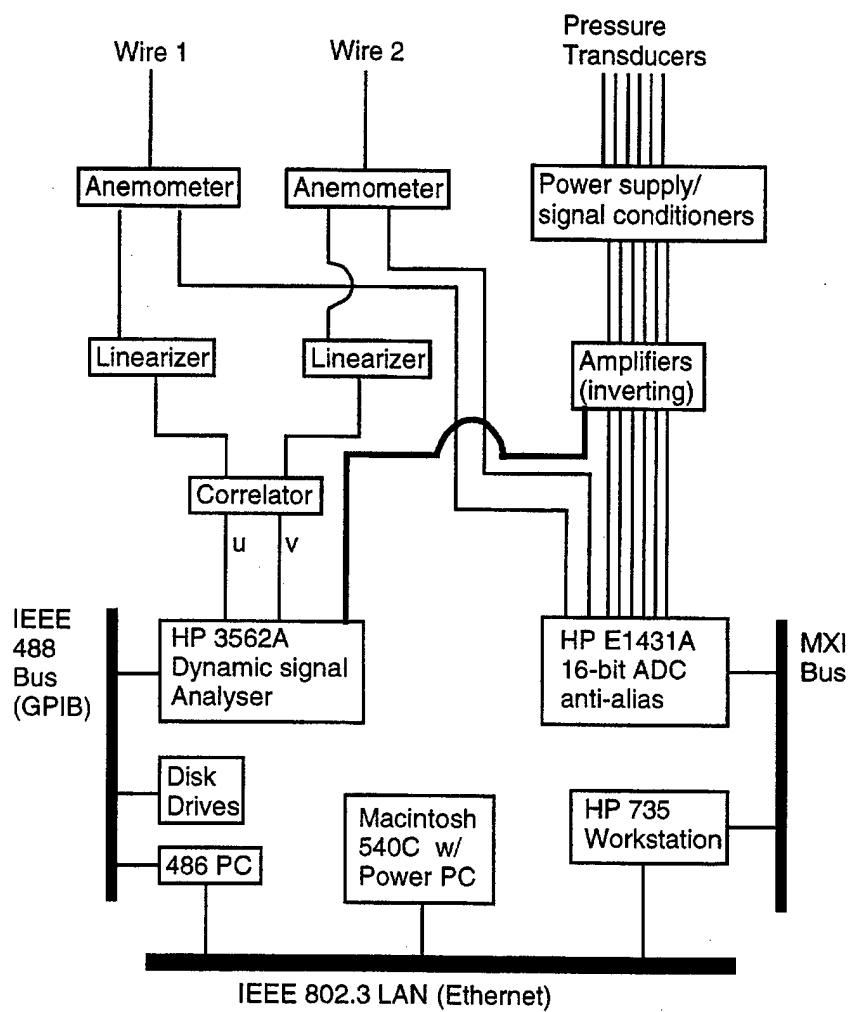
Figure 2.2: Schematic diagram of CUA data acquisition and processing system

and probe supports were mounted inside the tunnel test section on a motorized traverse system.

The single-wire boundary layer probe as well as the cross-wire probe were calibrated using methods similar to those of Kammeyer [25]. The single-wire calibration output voltages were converted to velocities using the conventional Kings Law approach

$$E^2 = A + BU^n,$$

where E is the anemometer output voltage, U is the velocity in m/s and A, B, and n are constants determined by a least squares method. The cross-wire probe calibration velocities were fit to fourth order, two dimensional polynomials using a least squares regression method. These methods are discussed in detail in Kammeyer [25].

For digital measurements, the output from the hot wire anemometers (bridge currents) and the output of the amplified pressure signals were input to the digital data acquisition system. This system is also described in detail in Kammeyer [25]. The primary component of the data acquisition system is the VXI-based Hewlett-Packard (HP) E1401-A C-size mainframe which contains the model E1431A, 25.6 kHz, 8 channel digitizer. The digitizer features include high sampling rates, built-in signal conditioning (anti-alias, etc.) and high-resolution, 16-bit, analog to digital conversion.

The system was controlled by an HP model 735 workstation on an MXI bus using a model E1482B VXI-to-MXI interface module in the mainframe. Data were acquired from the 1431A directly to the HP 735 memory at a rate of 32,768 samples/sec via software developed in-house [40]. The binary data were converted to ASCII format using conversion routines, developed in-house, which made the time

records available to MATLAB^{TM} for post processing and analysis. The post processing is described in chapter 3.

Linearized velocity data, as well as amplified pressure signals, were input to an HP 3562A Dynamic Signal analyzer. The HP 3562A is a two-channel fast Fourier transform (FFT) analyzer with 100 kHz bandwidth. Log resolution auto and cross spectral binary files were then transferred to a 486 PC and converted to ASCII format using HP Standard Data Format (SDF) utilities and made available for post processing with MATLAB^{TM}.

Velocity and pressure data were available to the HP 735 workstation as well as to the 486 PC and a Macintosh 540C (Power PC) laptop computer via an IEEE 802.3 local area network.

2.2 Pressure Transducers and Array Design

2.2.1 Transducers

The pressure transducers used to populate the measurement array were chosen based on several criteria including cost, configuration, ruggedness, sensitivity, and range. Several of the criteria such as diameter (configuration) and sensitivity are conflicting; as diameters get small, high sensitivity is more difficult to achieve. However, because the objective of the experiments was to resolve and track small scale turbulent structures with a multi-element array, small diameter and low cost drove the selection process.

In the initial part of this investigation, several single transducers were installed in the wind tunnel and tested. One of the transducers tested was the Endevco model 8507C–2. While this transducer lacked the sensitivity of the Bruel & Kjaer (B&K) microphones used by previous investigators [16, 53, 25], its smaller diameter and lower cost made it an attractive choice. The 8507C-2 was also shown to adequately
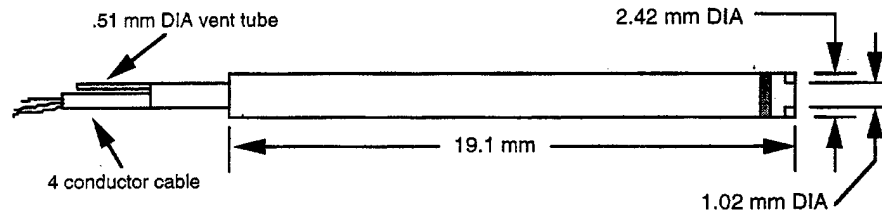
Figure 2.3: Physical characteristics of the Endevco model 8507C-2 pressure transducer

reproduce the spectral and statistical features of the wall pressure field as measured by the B&K condenser type microphones at tunnel speeds greater than approximately 10 m/s (33 ft/s). A detailed comparison of the performance of the Endevco and B&K sensors is provided in Appendix A.

The 8507C-2 is a piezo-resistive transducer with a range of 2 psig and a sensitivity of 150 mV/psi. The measured fluctuating pressures in the wind tunnel at tested flow speeds are on the order of 10^{-3} psi. The signal to noise achieved in the frequency range of interest (100 Hz to 5 kHz) is approximately 25 dB. The active sensing surface of the 8507C-2 is made of silicon and incorporates a four-arm Wheatstone bridge diffused into the silicon chip [14]. The surface of the silicon chip is raised to concentrate the stress at the location of the resistive elements in the bridge. The dimensions of the transducer are shown in figure 2.3. The outside diameter of the 8507C-2 is 2.42 mm; however, the sensing element is exposed to the flow through a holed cap. The hole diameter and hence the actual sensing diameter of the transducer is 1.02 mm; this is equivalent to approximately 39 viscous units for the boundary layer tested (see Section 2.3).

2.2.2 Wall Pressure Array

The purpose of the wall pressure array as defined in section 1.3 is to track and measure the spatial extent of near wall turbulent structures. To resolve the small

scales at which these structures exist, the sensing diameter of the transducer had to be minimized. To track these structures throughout their convective lifetime, which is known to be larger than their actual physical scale, the size of the array had to be large. The resulting array design was a compromise between cost and performance and was judged to be adequate for the scope of this investigation.

The array block was machined from a two-inch thick slab of polyurethane to the configuration shown in figure 2.4. The polyurethane block was designed to fit into an existing access port in the vertical wall of the tunnel test section. The array block surface was machined to tolerances of order 10^{-3} inches to provide a smooth surface, flush with the wall of the test section. The interface between the array block and the test section wall was nearly undetectable by touch. Boundary layer measurements made upstream and downstream of the interface showed no measurable disturbance to the flow field. The diameter of holes shown in figure 2.4 was drilled to fit the pressure transducers so that they could be installed without the use of adhesive.

2.3   Features of Turbulent Wall Flow

All experiments in this investigation were conducted with an equilibrium turbulent boundary layer at approximately 15 m/s. To verify that the boundary layer was equilibrium, velocity surveys were conducted over the surface of the transducer array. The results of both single-wire and cross-wire surveys are presented in this section. Based on the criteria for equilibrium flows established by Hussain [21], the boundary layer for the experiments was determined to be equilibrium. These criteria are:

1. A mean profile of proper shape with a shape factor of $H \approx 1.4$.

2. A mean profile satisfying the law of the wall including an adequate extent in the log-law region.
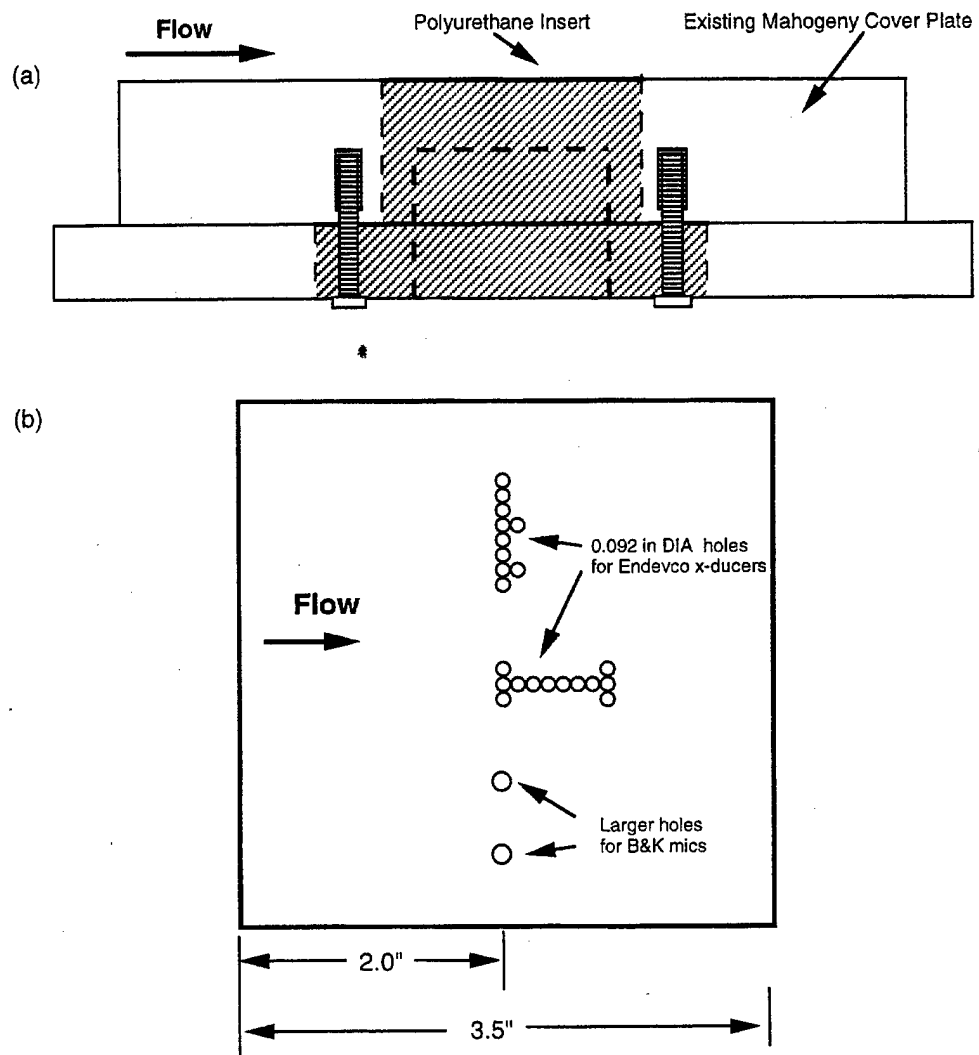
Figure 2.4: Configuration of the wall pressure array and mounting block

3. A wake strength that is appropriate for the Reynolds number of the flow.

4. A peak in the turbulence intensity profile ($u'/u_\tau=2.5$ at $y^+=15$).

5. A monotonic decrease in u' to the freestream value.

6. A broadband continuous u' spectrum that contains an inertial subrange.

The velocity data presented in this section will be shown to satisfy these criteria.

2.3.1   Mean Velocity Profile

The boundary layer on the array face, just upstream of the pressure transducers was surveyed with both a single-wire and a cross-wire anemometer. The boundary layer parameters, measured with the single-wire probe, are shown in table 2.2. The shear velocity, u_τ, was chosen as that which enabled the velocity profile to best fit the classical log-law relationship:

$$u^+=2.44\ln y^++4.9,$$

where $u^+=u/u_\tau$ and $y^+=yu_\tau/\nu$. The coefficients 2.44 and 4.9 are those used by Clauser [12]. The boundary layer thickness, δ, was defined as the distance from the wall where $u=0.99U_0$, where U_0 is the freestream velocity. The displacement thickness, δ^*, and the momentum thickness, θ, were obtained by integrating the mean velocity profile. The skin friction coefficient C_f was obtained from the definition of shear velocity $C_f=2(u_\tau/U_0)^2$, as well as calculated from the momentum and displacement thicknesses using the Ludwieg-Tillman relationship:

$$C_f=0.246\mathrm{Re}_\theta^{-.268} * 10^{-0.678H}$$

where $\mathrm{Re}_\theta=\theta U_0/\nu$, and $H=\delta^*/\theta$ is the conventional shape factor.

Table 2.2: Boundary layer parameters

Parameter	SI	English
Freestream Velocity, U_0	15.33 m/s	50.28 ft/s
Shear Velocity, u_τ	0.59 m/s	1.93 ft/s
u_τ/U_0	0.038	
Boundary Layer Thickness, δ	2.73 cm	1.075 in
Viscous TBL Thickness, δ^+	1026	
Displacement Thickness, δ^*	0.49 cm	0.195 in
Momentum Thickness, θ	0.34 cm	0.133 in
Reynolds No., Re_θ	3364	
Shape Factor, H	1.4606	
C_f calculated	0.00285	
C_f measured	0.00295	

Figure 2.5 shows the mean streamwise velocity profile normalized by boundary layer thickness and freestream velocity. Integration of the profile to compute δ^* and θ results in a shape factor of 1.46, satisfying criteria #1 above. The same data are shown in figure 2.6 normalized by viscous wall variables and plotted against $u^+=y^+$ and $U^+=4.44\ln y^+ + 4.9$ reference lines. The profile exhibits adequate log-law and wake regions satisfying criteria #2 and #3. The inner and outer regions of the boundary layer are also illustrated in figure 2.6, they are defined as:

1. Viscous sublayer $(0 < y^+ < 5)$

2. Buffer layer $(5 < y^+ < 30)$

3. Log-law region $(y^+ < 30$ and $y < 0.2\delta)$

4. Outer layer $(y > 0.2\delta)$

The viscous sublayer, the buffer region and the log-law region make up what is commonly referred to as the "inner" layer. The outer layer is comprised of the rest of the boundary layer, including the "wake region". The overlap region includes the log-law region.
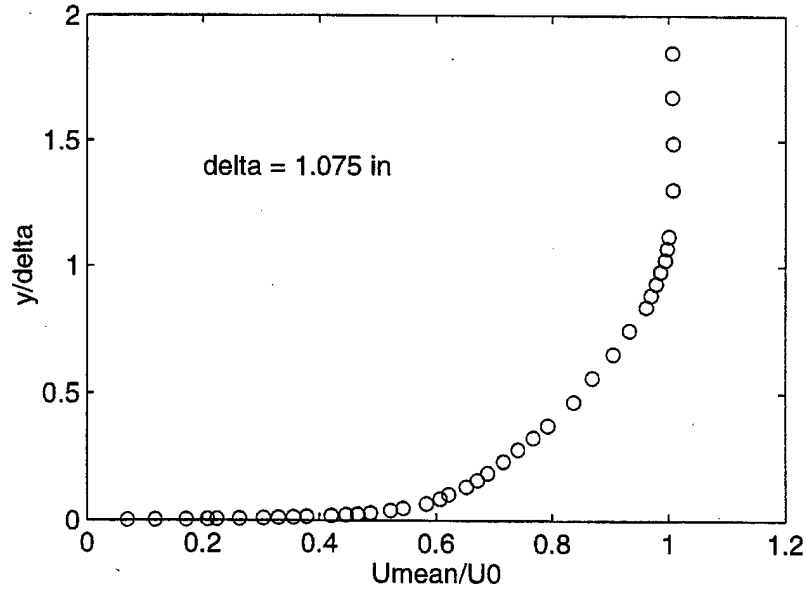
Figure 2.5: Mean streamwise velocity profile measured with boundary layer probe, $U_0 = 15.3$ m/s
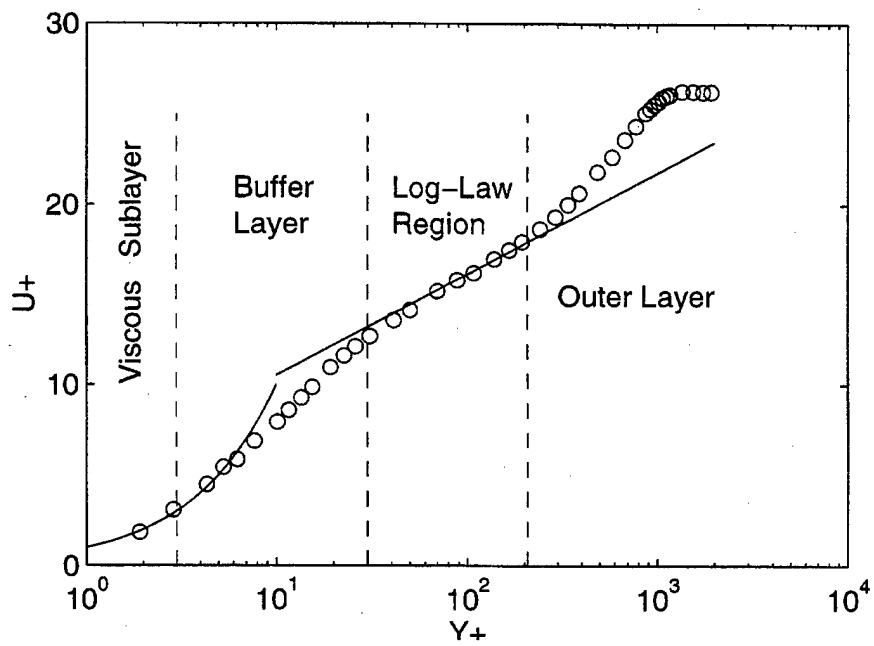
Figure 2.6: Mean velocity profile scaled on viscous variables, $U_0 = 15.3$ m/s

2.3.2   Turbulence Statistics

Statistical and spectral properties of the velocity field are presented in this section. Turbulence intensity is defined as u'_{rms}/U_0 where RMS denotes root mean squared, i.e., the square root of the second moment of velocity

$$u'_{rms} = \sqrt{\tfrac{1}{N}\sum u_i^2} \; ; \; \text{N= number of samples.}$$

Streamwise and wall-normal turbulence intensity profiles are shown in figure 2.7. The peak value of u'_{rms}/u_τ as well as the monotonic decrease to free stream levels satisfy criteria #4 and #5 for equilibrium flows. The wall-normal turbulence intensity exhibits the same monotonic decrease to free stream levels. Because the wall normal component (v) was acquired with a cross-wire probe as opposed to a single-wire boundary layer probe, measurements at wall distances less than $y^+=25$ $(y/\delta=0.017)$ were not possible. These data are consistent with the results of Farabee [16], Wilczynski [53], and Kammeyer [25] obtained in the same facility.

The Reynolds stress profiles for three independent cross-wire surveys are shown in figure 2.8 where mean Reynolds stress, $-\overline{uv}$, is normalized by free stream velocity and plotted against y/δ. The Reynolds stress scaled on local RMS velocities, shown in figure 2.9, is commonly referred to as the turbulence stress correlation coefficient. This coefficient is a measure of the level of coherent turbulence activity. Again, these data are consistent with previously cited investigators [16, 53, 25].

The power spectrum of the streamwise velocity were also obtained at various locations in the boundary layer survey. The auto spectrum can be obtained from the Fourier transform of the auto correlation, R_{uu}, where $R_{uu} = < u(y,t)u(y,t+\tau) >$ and $<>$ indicates the appropriate statistical average. The auto power spectrum $\Phi_u(\omega)$ can be obtained from:

$$\Phi_u(\omega) = \tfrac{1}{2\pi} \int_{-\infty}^{\infty} R_{uu}(\tau)e^{i\omega\tau}d\tau.$$

29
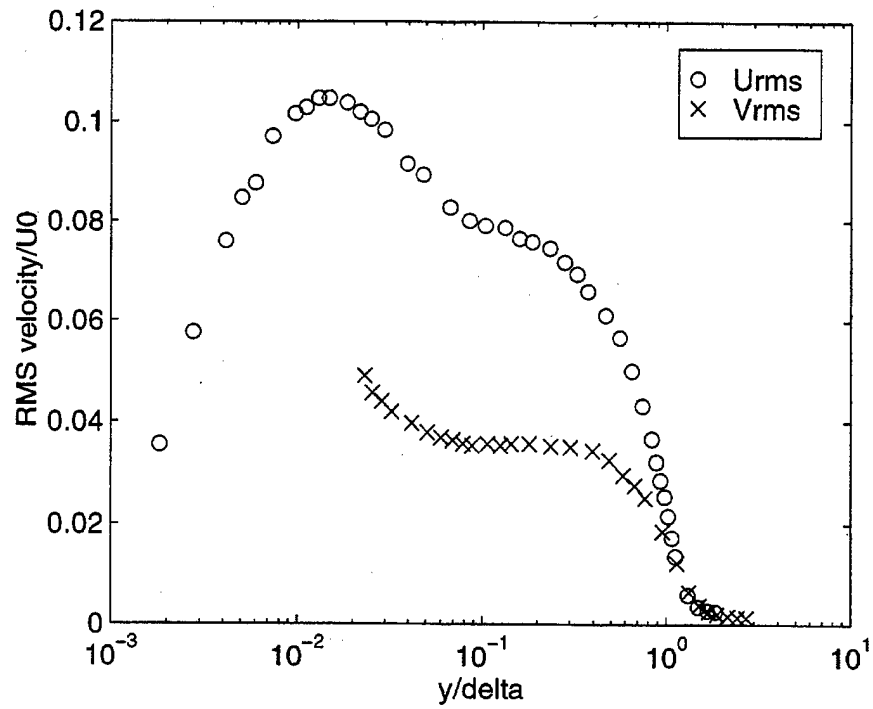
Figure 2.7: Normalized streamwise and wall-normal turbulence intensity profiles
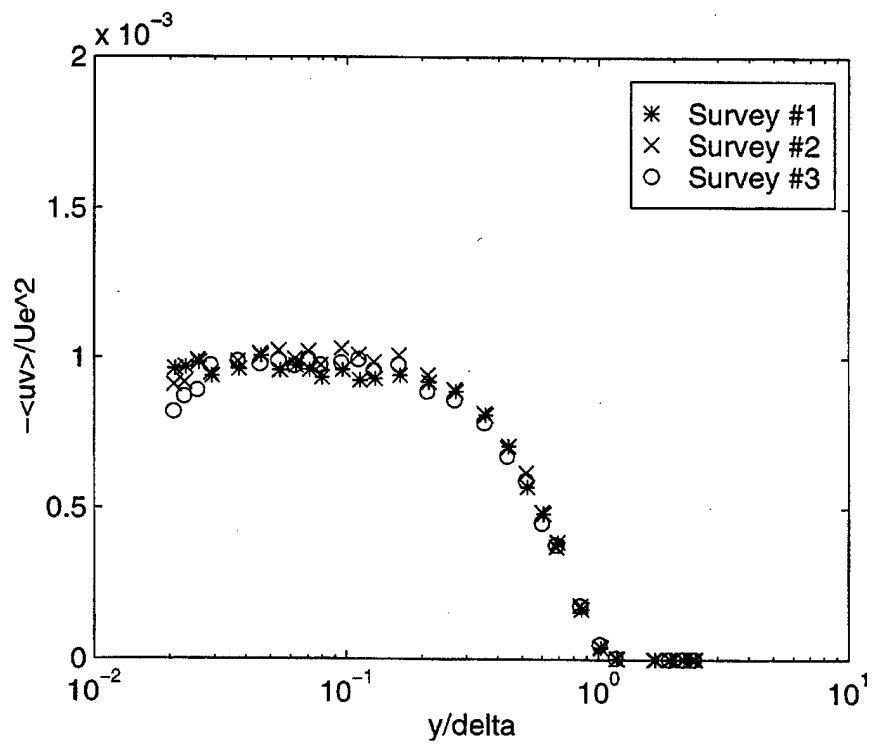
Figure 2.8: Reynolds stress profiles for three independent boundary layer surveys
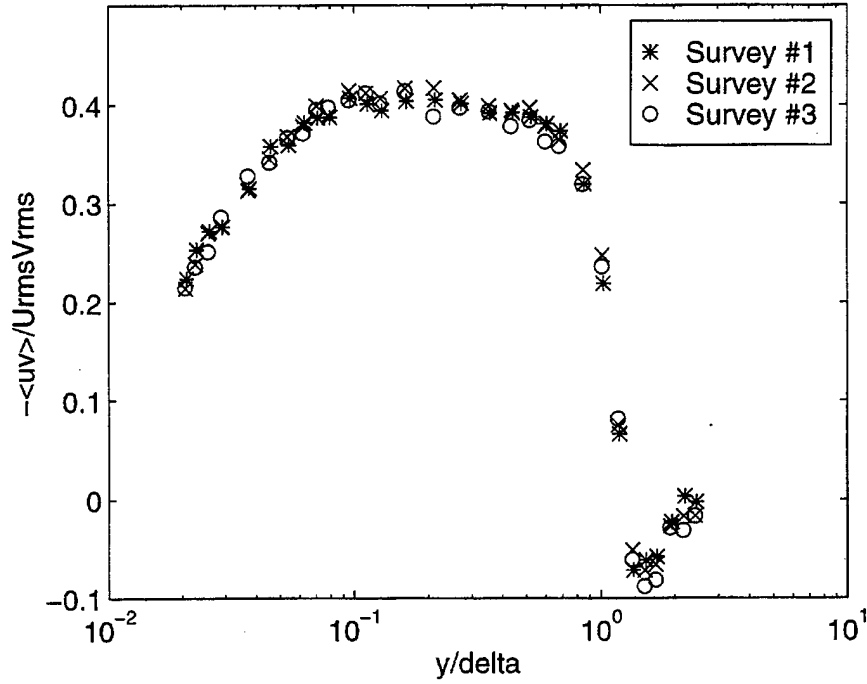
Figure 2.9: Turbulence stress correlation coefficient for three independent boundary layer surveys

The velocity spectra are presented in the form of the power spectral density in which the spectral levels at each frequency are normalized by the bandwidth at that frequency. For a detailed discussion of these functions, see Bendat & Piersol [3]. The velocity spectrum is a common method of defining the distribution of turbulent energy in the frequency domain, or as summarized in Tennekes & Lumley [48], it is indicative of how eddies of different sizes exchange energy with each other. The first moment of the spectral density, $\omega \Phi_u(\omega)$, is a popular method of presenting spectral data. Since equal areas under different sections of the first moment spectral density contribute equally to the mean square energy, peaks occurring in this spectrum indicate the presence of a dominant scale at which turbulent energy occurs.

Figure 2.10 shows the first moment spectral density at various locations across the boundary layer. These data were obtained using the FFT analyzer described in Section 2.1.2. Near the wall, especially at $y/\delta = .07$, two weak humps appear

31
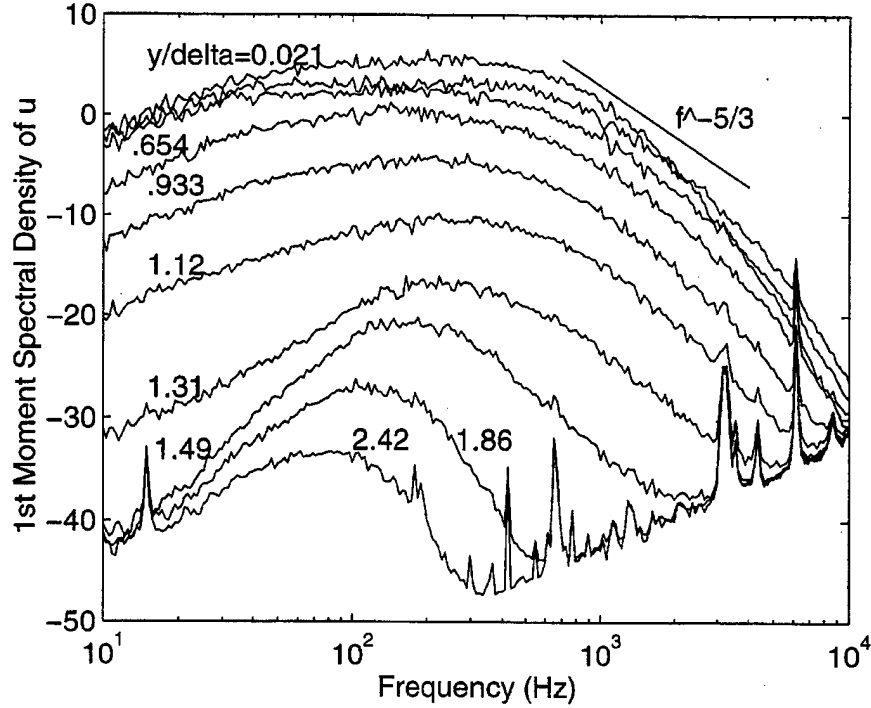
Figure 2.10: Streamwise velocity spectra at various wall distances

in the velocity spectrum. These humps occur at frequencies ($\omega\delta^*/U_0$) of approximately 0.1 and 0.8, indicating that two characteristic flow scales exist in this region. Farabee [16], and Bullock [10] observed a similar behavior closer to the wall and at slightly higher frequencies in flat plate boundary layers. Snarski & Lueptow [46] observed these humps as well for an axial flow. Farther away from the wall, the outer irrotational flow is observed and the velocity spectrum monotonically decays to the classical "low frequency irrotational bulge" as observed by Farabee and Casarella [17].

The inertial subrange is a range of wavenumbers (k) at which the turbulence energy spectrum scales on $k^{-5/3}$, commonly referred to as the Kolmogorov 5/3 law. The extent of this range is a function of turbulence Reynolds number [48]. A line indicating the slope that such a spectrum would have is shown in figure 2.10. The transformation between frequency and wavenumber is made using Taylor's hypoth-
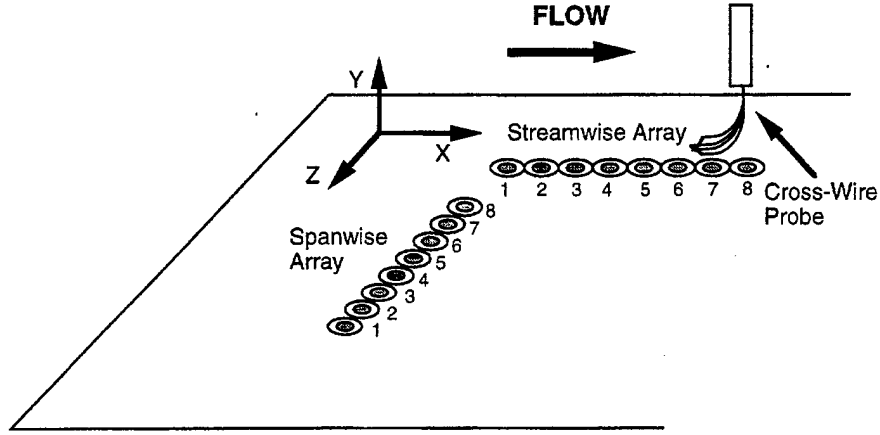
Figure 2.11: Sensor configuration during typical velocity and pressure measurements

esis, $k_1 = \omega/U_c$, which results in $\Phi(k_1, y) = U_c \Phi(\omega, y)$, where, k_1 is the streamwise wavenumber component and U_c is the convection velocity, assumed to be constant and equal to the local mean velocity, $U(y)$. At the Reynolds number of the flow tested, the inertial subrange is not obvious, however, a number of velocity spectra in the log law region of the boundary layer do show adequate $k^{-5/3}$ behavior.

2.4 Experiments Performed and Acquired Data

Two distinct sets of experiments were performed in this investigation. The first set involved the measurement of fluctuating wall pressure only, with the transducer array oriented in both the streamwise and spanwise directions. These measurements were, in part, exploratory; to determine if high amplitude wall pressure events could be tracked, and if so, to measure their spanwise and streamwise extent.

The second set of experiments involved the simultaneous measurement of pressure and velocity using the streamwise and spanwise transducer arrays. The velocity data were collected at 30 wall-normal locations. Figure 2.11 illustrates the orientation of the various sensors during one of the velocity surveys. To map the flow field in

Table 2.3: Acquired data matrix

Database	Array (#sensors)	Meas. Plane	Velocity Data	P-V Grid
1	Spanwise (8)	Z Axis	None	
2	Streamwise (8) ·	X Axis	None	
3	Spanwise (6)	Z-Y Plane	Z/d = 0,4	10 x 30
4	Streamwise (6)	X-Y Plane	X/d = 6, 12, 18	18 x 30

the X-Y plane, three different cross-wire surveys were conducted downstream of the streamwise transducer array. The first velocity survey was conducted at the downstream edge of the sixth transducer in the array. The other surveys were conducted 6 and 12 transducer diameters (d) downstream of the first position, thereby creating a uniform streamwise grid of measurement stations. In each survey, velocities (u and v) were measured at the same wall distances (y). The result was a rectangular grid (18 x 30) at which wall pressure and velocity signals could be simultaneously sampled and compared using correlation and conditional sampling techniques. A similar grid (10 x 30) was generated in the Y-Z plane using the spanwise transducer array.

Table 2.3 details the number and locations of the measurement stations. Since only 8 channels could be digitized at a time, the addition of the u and v signals in the second set of experiments limited the number of pressure transducers monitored to six. All measurements were made at a nominal free stream velocity of 15 m/s. In each of the experiments, the pressure and velocity signals were sampled simultaneously at a rate of 32,768 Hz for a period of 10 seconds. These digitized time records were stored for later processing. The signal processing techniques are discussed in Chapter 3. As discussed above, four distinct raw databases were acquired in the experimental phase of this investigation. The first two databases were analyzed using a variety of filtering and signal processing techniques, and are discussed in Chapter 4. The last two databases contain the major findings of the investigation.

34

These data are thoroughly analyzed, guided by the findings discussed in Chapter 4, and are discussed in Chapter 5.

Chapter 3

FILTERING AND PROCESSING OF EXPERIMENTAL DATA

The two forms of signal processing applied in this investigation were digital filtering and cross-correlation. The wall pressure and velocity data were digitally filtered to discriminate between large and small scale turbulent activity. The primary findings achieved in this investigation are a direct result of the filtering techniques used. Similarly, a majority of what was learned in this investigation about the physics of turbulent flows came from applying several correlation techniques to the filtered wall pressure and velocity measurements. It is important, therefore, to understand these post-processing techniques, how they will be used, and their limitations. The post-processing techniques employed in the current investigation will be discussed in this chapter. A comparative evaluation of the effects of these signal processing techniques are given at the end of this chapter.

The experimental data collected during the wall pressure and velocity surveys listed in table 2.3 have been permanently retained for future use. The data bases are considered to be high quality and should prove to be useful to other investigators who may wish to analyze it using other signal processing techniques.

3.1 Filtering of Experimental Data

In this section, the concept of filtering is discussed in detail. The filtering of turbulent signals is a cornerstone of the findings made in this investigation. Without the use of filtering, little information about the relationship between turbulent scales could be derived from time records of wall pressure or velocity. Filtering enables the researcher to focus on certain "scales of interest" within a turbulent signal and extract information which would otherwise be masked by noise. The rationale for filtering and the techniques used in this investigation are presented.

3.1.1 Rationale for Filtering

In most applications, the filtering of a signal is done to help discriminate a desired signal from background noise. To some extent, the same is true for this investigation. The noise in this case, however, includes more than electrical noise, acoustic interference, or structural vibration of the sensor. The wall pressure or velocity signatures of turbulent structures that are not within the frequency bands of interest (such as the inducec irrotational motions outside the boundary layer) are filtered out.

Many researchers have shown that low frequency, large scale structures tend to dominate the outer flow region of the boundary layer while high frequency small scale structures are generally limited to the near wall region [30, 50, 17]. To identify the wall pressure signature of the near wall turbulent structures will then require the discrimination between the large and small scales. Kammeyer [25] did this using a wavelet filtering scheme. Previous investigators used Fourier based filtering to separate large and small scale structures [30, 36].

The advantages of wavelet filtering versus Fourier based filtering to discriminate between turbulent scales will not be addressed in this report. It is recognized

Table 3.1: Frequency bands [Farabee and Casarella (1991)]

Region	Frequency Range	Actual Frequency
Low	$\omega\delta/u_\tau \leq 5$	f$\leq$17 Hz
Mid	$5\leq \omega\delta/u_\tau \leq 100$	17 Hz$\leq$f$\leq$344 Hz
Universal	$100\leq \omega\delta/u_\tau \leq 0.3R_\tau$	344 Hz$\leq$f$\leq$1075 Hz
High	$0.3R_\tau \leq \omega\delta/u_\tau$	1075 Hz$\leq$f

that frequency based filtering of turbulent signals may not be the optimum method. A "single" turbulent structure contains a range of scales and cannot therefore be isolated by focusing on a narrow frequency band. The hairpin vortex discussed earlier, for example, is known to consist of large scales (heads) as well as small scales (legs). It is further understood that turbulent structures of all scales exist across the boundary layer; they are not confined to only inner or outer locations. The dominant physical mechanisms of turbulence can, however, be studied using frequency based filtering techniques. By focusing on a band of frequencies in the wall pressure spectrum, for example, one is not isolating distinct turbulent structures, but is simply focusing on turbulent motions which have the appropriate spatial, temporal, and convective time scales. In general, these time scales do tend to dominate certain regions of the boundary layer.

In this investigation, frequency-based, band-pass filtering was chosen as the tool for differentiating between turbulent scales. As reviewed in Bull (JSV96), Farabee and Casarella [17] defined the frequency bands with which different turbulent regions of the boundary layer contribute to the respective regions of the wall pressure spectrum. These are shown in table 3.1. The third column in table 3.1 contains the equivalent frequencies for the boundary layer conditions studied in this investigation. The low frequency range is in the facility noise region and thus is not relevant to the investigation. Farabee and Casarella [17] showed that the mid frequency wall pressure fluctuations scaled on outer flow variables whereas high frequency pressure

fluctuations scaled on inner (viscous) variables. The universal or overlap frequencies scaled on mixed (inner and outer) variables.

Kammeyer's [25] wavelet filter when applied to velocity or wall pressure signals behaves similarly to a band pass filter with cutoff frequencies of approximately 1 kHz and 7 kHz. Kammeyer demonstrated that near wall turbulent activity could be discriminated from background turbulence by applying this filter. In this investigation, the cutoff frequencies chosen for band-pass filtering were based primarily on the results of Kammeyer and Farabee & Casarella, as well as on exploratory measurements made in this investigation.

The objective of the filtering was to discriminate between large scale and small scale "active" structures. Based on the behavior of velocity spectra outside the boundary layer (see figure 2.10) a filter was chosen to remove the scales associated with the outer "irrotational bulge".These motions are assumed to be passive since no evidence exists regarding these structures being associated with turbulent production. This band-pass filter had cutoff frequencies of 100 and 300 Hz, a subset of the "mid" frequency range defined earlier in table 3.1. A second filter representing the frequencies between the mid and the high ranges was chosen with cutoff frequencies of 300 and 1200 Hz ("universal" range). Finally, a high frequency band-pass filter was chosen which best duplicated the performance of Kammeyer's wavelet filter. This filter had cutoff frequencies of 1200 Hz and 5 kHz ("high" frequency range). Figure 3.1 shows the response of these filters to a typical wall pressure spectrum. For the remainder of this document, these three filters will be referred to as follows:

Filter No.	Frequency Band (Hz)	Spectral Region
1	100-300	"Mid"
2	300 - 1200	"Universal"
3	1200 - 5000	"High"

3.1.2 Digital Filtering Techniques

Published findings from several investigators on the statistical properties of wall pressure signals, which were once believed to have physical significance, have been recently brought into question due to concerns about bias attributed to the effect of analog filtering techniques. The negative skewness of fluctuating wall pressure seen by Karangelen [26], for example, has been attributed to phase distortion of the signal due to analog high pass filtering at 100 Hz. For this reason the filtering of the velocity and wall pressure signals was performed digitally using a method known to be distortion free. The digital filtering was accomplished using the MATLAB library of signal processing routines.

The wall pressure and velocity signals were digitized in "raw" voltage form, i.e.. unfiltered. Inherently, the velocity signals were relatively free of unwanted acoustic or electrical noise. The wall pressure signals however appeared to be contaminated with high frequency noise. Additionally, the wall pressure signal was contaminated with facility related acoustic noise (see figure 3.1). For these reasons, the first layer of filtering performed on the pressure and velocity signals was a digital band-pass filter with cutoff frequencies of 100 Hz and 5 kHz, (labeled as filter 0) eliminating the high frequency transducer related noise and the low frequency facility noise. The velocity and pressure time records subject to this filtering were then considered "clean" and representative of turbulence activity in the boundary layer. This "clean" signal will hereafter be referred to as "unfiltered" or "filter 0" data when being compared to data subject to filters 1, 2, or 3.

The high-pass and band-pass filters used a 5th-order Butterworth filter applied both forwards and backwards to eliminate phase lags. 500 sample points were removed from the beginning and end of each time record to eliminate end effects. The Butterworth filter subroutine was provided with the MATLAB software.

Another form of scale discrimination or filtering was applied to pressure and velocity time records in an attempt to detect turbulent events. This was the Variable Interval Time Average (VITA) [5] function applied to the variance of the turbulent signal. The result is a measure of the localized variance of a signal, and for a signal $p(t)$ is defined as

$$\nu_p(t, T_v) = \frac{1}{T_v} \int_{t-\frac{T_v}{2}}^{t+\frac{T_v}{2}} p^2(\tau)d\tau - \left\{ \frac{1}{T_v} \int_{t-\frac{T_v}{2}}^{t+\frac{T_v}{2}} p(\tau)d\tau \right\}^2,$$

where T_v is an adjustable integration time. The VITA function has been applied to the streamwise velocity signal $u(t)$ by numerous investigators as a method to detect burst/sweep events. In this investigation the VITA method is applied to wall pressure for the same purpose: to detect regions of increased localized activity. One advantage of the VITA method is the adjustable integration time. This parameter can be changed to fit the time scales of the events of interest. This flexibility allows the VITA method to be applied to velocity and pressure signals which have been band-pass filtered by tuning the integration time to the appropriate time scales.

3.2 Correlation of Experimental Data

One of the objectives of this investigation is to determine the spatial extent of the organized motions, more specifically, the causal relationship between large scale organized structures within the boundary layer, and small scale, near wall, turbulent-producing events. This will be examined by filtering the pressure and velocity signals with filters 1,2, and 3, and correlating them at various locations in the flow. Three correlation methods will be used in this investigation. They are listed below:

- Temporal Correlation

    - Correlation coefficient

41

− Normalized correlation

● Spectral Correlation (coherence function)

● Conditional sampling & ensemble averaging

These post processing techniques will be defined in this section.

3.2.1 Correlation and Cross Spectral Methods

Two signals $u(t)$ and $v(t)$ are considered perfectly correlated when their correlation coefficient has a value of 1.0. The correlation coefficient is defined by way of the cross-correlation function, $R_{uv}(\tau)$, where,

$$R_{uv}(\tau) = \lim_{T\to\infty} \frac{1}{T} \int_0^T u(t)v(t+\tau)dt.$$

The cross correlation coefficient is simply the cross-correlation function normalized by $u_{rms}v_{rms}$ such that its value when $u(t)$ and $v(t)$ are identical, i.e.., the auto-correlation coefficient, is unity when $\tau = 0$. The cross-correlation coefficient is a direct measure of the correlation between two signals.

If two signals being analyzed are positive-definite (always > 0), such as a squared signal or a VITA function, simply computing the cross-correlation coefficient of those signals would not be appropriate. The cross-correlation coefficient of any two positive-definite signals, including uncorrelated noise, will have a sawtooth shape with a peak at $\tau=0$. Therefore, when correlating VITA function time records, the correlation coefficient is expressed in dB relative to the base sawtooth shape [41]. The resulting function is referred to hereafter as the normalized correlation.

By taking the Fourier transform of the cross-correlation function, one obtains the cross-spectral density function:

$$\Phi_{uv}(\omega) = \frac{1}{2\pi} \int_{-\infty}^{\infty} R_{uv}(\tau)\, e^{i\omega\tau}d\tau.$$

The cross-spectral density function can be expressed as a normalized magnitude and phase. The normalized magnitude, $\Gamma_{uv}^2(\omega)$, commonly referred to as the coherence function, is given as

$$\Gamma_{uv}(\omega) = \sqrt{\frac{\Phi_{uv}^*(\omega)\Phi_{uv}(\omega)}{\Phi_u(\omega)\Phi_v(\omega)}},$$

where the * denotes the complex conjugate, and $\Phi_u(\omega)$ and $\Phi_v(\omega)$ are the auto-spectral densities of u and v defined in Chapter 2. The phase function is given as

$$\Theta(\omega) = \tan^{-1}\left[\frac{Im(\Phi_{uv}(\omega))}{Re(\Phi_{uv}(\omega))}\right],$$

where Re and Im denote the real and imaginary parts of the cross-spectrum.

Cross-correlation and coherence functions are used extensively in this investigation to establish a relationship between pressure and velocity signals. They are important tools for correlating large and small scale turbulent structures. While these functions can tell much about the relationship between flow variables, they do not directly identify individual turbulent structures, they simply correlate various regions of the flow field.

Another common method of demonstrating the relationship between flow variables is referred to as conditional sampling. This technique, used by many researchers to correlate turbulent structures with other flow variables such as shear stress or velocity gradients, is discussed in the next section.

3.2.2 Conditional Sampling and Ensemble Averaging

The objective of conditional sampling is to identify the relationship between a repeated event or salient feature in one signal and a repeated pattern or feature in another signal. In turbulence, one is often looking for a characteristic pattern in one flow variable, such as streamwise velocity, which appears to be correlated with the

occurrence of an event in another flow variable, such as wall pressure. The procedure for conditional sampling in this case would be to sample the velocity time record at times when criteria for the detection of events are met in the pressure signal. The individual velocity samples would then be synchronized and averaged.

Ensemble averaged event shapes depend on many factors including: the criteria on which the samples are synchronized, the threshold on which the events are defined, the number of events detected, and the uniqueness of the salient feature on which detection is based. Clearly, interpreting the results of this type of analysis is not straightforward. It is a technique which improves with experience and the investigator having extensive prior knowledge of the signals being analyzed. Yuan and Mokhtarzadeh-Dehghan [56] review many of the early conditional sampling methods used by the turbulence community.

The method employed in this investigation will be detection of peak wall pressure events and then sampling and averaging of streamwise and wall normal velocity time records. The samples are synchronized on the times at which the peak wall pressure events occur. The selection of the threshold value (k) applied to the wall pressure was based on experience gained during exploratory measurements made early in the investigation. The thresholds were based on the magnitude of the wall pressure signal normalized by its RMS value. Threshold values of $k = p/p_{RMS}$ of $\pm$ 1, 2, and 3 were tested previously by Wilczynski [53] for a different type of pressure transducer. Those tests were repeated in this investigation using the new transducers. The results of both tests are presented in appendix A as part of the comparative evaluation of the Endevco pressure transducers.

As shown by previous investigators [53, 25], high amplitude wall pressure events, particularly high frequency, short duration events, tend not to occur as single peaks but in clusters of peaks, both positive and negative. Kammeyer [25] went so far as to

develop an event detection criteria based on clusters or groupings of peaks. Table A.2 shows the statistics for single peak event detection obtained in this investigation. A threshold value of p/p_{RMS} of $\pm$ 2 was chosen as an adequate criterion for the detection of high amplitude wall pressure events. Application of this threshold value to the current wall pressure signals resulted in event statistics and average event shapes comparable to those obtained by Kammeyer using the cluster criteria. It was determined that, in general, the peak detection (k=2) and cluster detection of Kammeyer located the same number of events in the high frequency (filter 3) wall pressure time records.

By not allowing the events detected to have overlapping time windows, Kammeyer avoided the danger of multiple peak detections within a single cluster. This was an important feature since the shape of the ensemble averaged events is highly dependent on behavior of the signal prior to and following a peak. Nonetheless, the peak detection techniques employed in this investigation resulted in ensemble averaged event shapes similar to those obtained with cluster detection. The results for each of the filtered databases will be discussed in Chapters 4 and 5.

3.3 Comparative Evaluation of Signal Processing Techniques

3.3.1 Filtering Effects on the Signal

As discussed earlier, the wall pressure and velocity data were filtered at two stages. The signals were initially cleaned of facility acoustic and transducer electronic noise using filter 0. The spectral effect of this filter on a typical wall pressure signal is shown in figure 3.1 along with the auto spectra of the same signal subjected to filters 1, 2, and 3. The slope of the spectra near the cutoff frequencies illustrates the steepness of the 10-pole butterworth filtering scheme used. Nonetheless, there is an
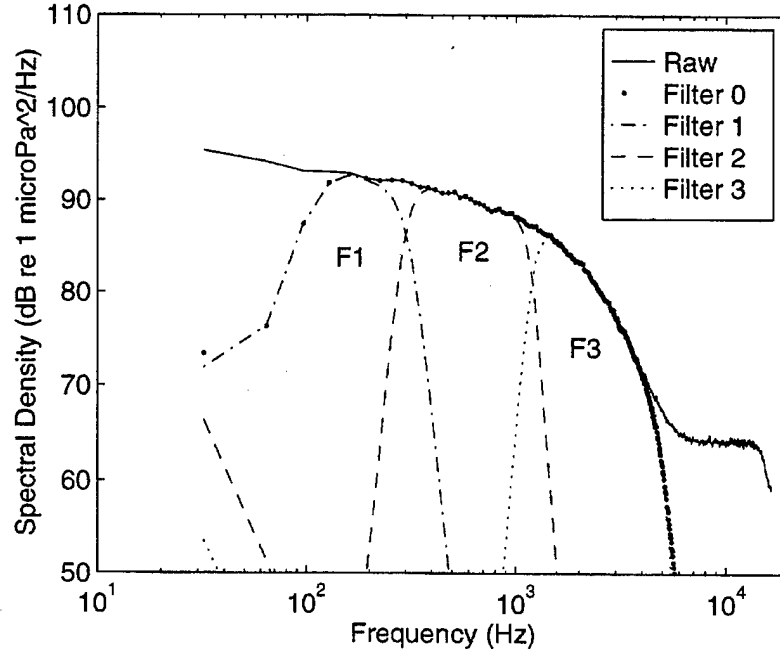
Figure 3.1: The spectral effects of band-pass filters on typical wall pressure signal ($U_0 = 15.3$ m/s)

unavoidable overlap between the spectra of neighboring filters.

A sample time record from a wall pressure signal subjected to filter 0 is shown in figure 3.2. All time records presented in this chapter are plotted against viscous time units ($t^+ = tu_\tau^2/\nu$). From figure 3.2 it is apparent that at these time scales, the essential features of the wall pressure signal are retained after filtering with filter 0. The high frequency choppiness and low frequency waviness of the signal that are removed by filter 0 are not associated with turbulent activity in the boundary layer. By removing the very low frequency content (below 100 Hz) of the wall pressure signal, and when observed in the time frame of figure 3.2, one appears to be removing a DC component from the signal. This can result in an increased number of zero axis crossings. From the standpoint of event detection, this observation is important since many event detection schemes rely on axis crossings to define the duration of an event.
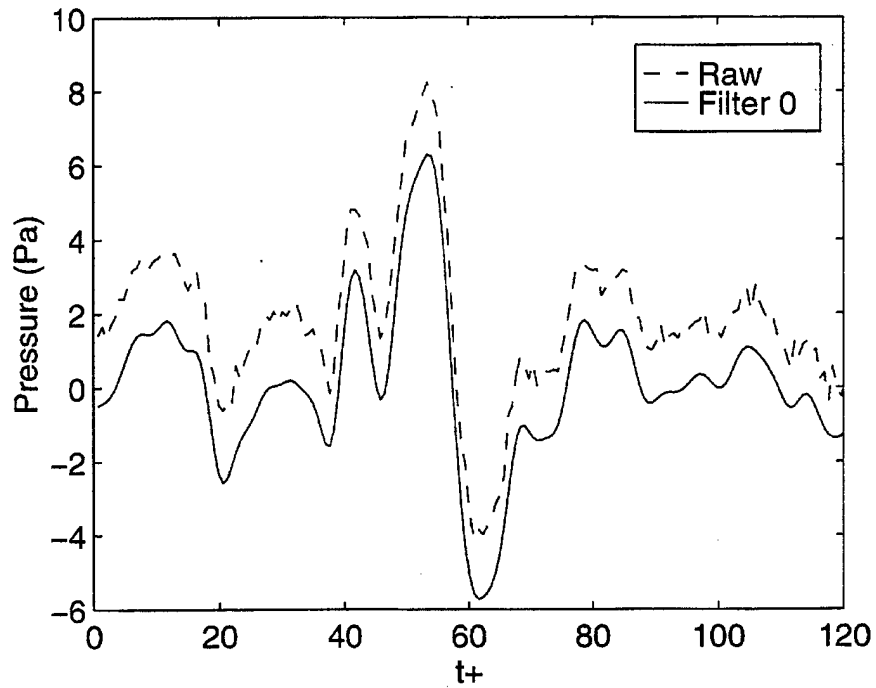
Figure 3.2: Sample raw versus band-pass filtered wall pressure time record

The same sample time record displayed in figure 3.2 is shown again in figure 3.3 subjected to filters 2 and 3. In this figure, the dynamics of the wall pressure signal begins to reveal itself. While filter 2 appears to maintain the large scale character of the signal, filter 3 appears to highlight the small scale events.

One feature of the unfiltered wall pressure spectrum in figure 3.1 is the flatness of the spectrum in the frequency ranges of filters 1 and 2. From this, one would expect that the statistical properties of a wall pressure signal subjected to filters 1 or 2 would be similar to those of random white noise subject to the same filtering. For this reason, and for the fact that the auto- correlation of white noise is only non-zero at $\tau=0$, the effects of band pass filtering on measured turbulent signals will be benchmarked by its comparative effects on white noise.

To illustrate the importance of the white noise comparison, sample time records
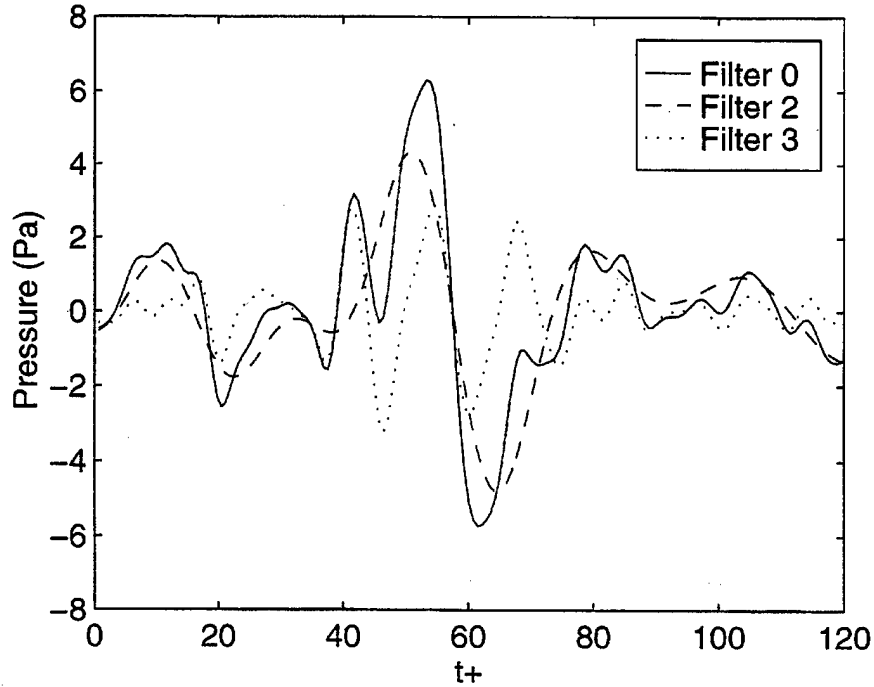
Figure 3.3: Sample wall pressure time record subjected to band-pass filters 0, 2, and 3

of wall pressure and white noise subject to various filters are shown in figures 3.4 and 3.5. Figure 3.4 shows a random white noise time record subjected to filter 0. Unlike the pressure signal shown in figure 3.2, the distinct frequency content of the original signal is dramatically altered by the filtering to produce an artificial signal having the correct time scales. This contrast is the first of many examples to be presented showing the distinction between a turbulent signal and random white noise.

Figure 3.5 compares the time records of white noise and wall pressure subjected to filter 3. While the white noise remains "noise-like", the high frequency pressure signal contains sustained periods of low amplitude activity interrupted by short duration, high amplitude events. Filter 3, designed to simulate Kammeyer's wavelet filter, appears to reveal some of the physics embedded in the intermittent wall pressure signatures of near wall burst/sweep events.

The comparisons made between noise and wall pressure signals subject to various
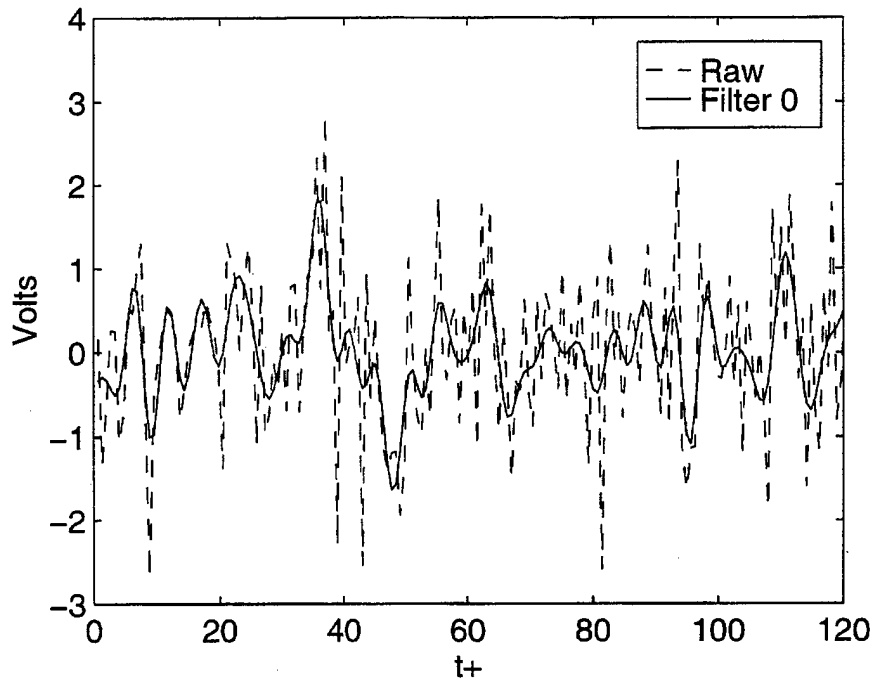
Figure 3.4: Sample raw versus band-pass filtered white noise time record
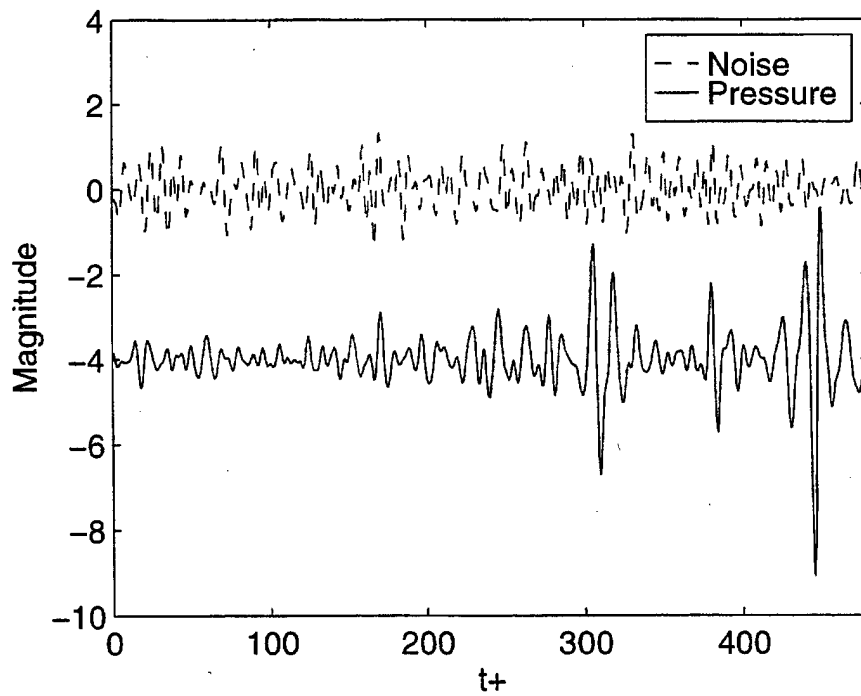
Figure 3.5: Sample white noise and wall pressure time records subjected to high frequency (filter 3) band-pass filtering

49

filters are important when one attempts to draw conclusions about turbulent activity based on wall pressure or velocity measurements. On the surface, unfiltered wall pressure as well as near wall velocity measurements appear "noise-like" in that their spectrum is generally flat and their time records are literally undecipherable. It is only when one begins to discriminate between the time scales incorporated in the signal and perform correlations on these filtered signals, that the embedded physics is revealed. However, the filtering must be done with caution.

3.3.2 Filtering Effects on Correlation

One of the most common methods used to describe the physical characteristics of a given flow field is to measure correlation functions. Whether it is wall pressure, velocity, shear stress, or another flow variable, the correlation of a signal with itself or with another flow variable can indicate the presence of organized, coherent motion. Kline [29] incorporated this terminology in his definition of organized structures. This statement will be shown in this section to be true only for unbiased, unfiltered experimental or numerical data. The bias introduced by filtering can artificially cause a signal to be correlated with itself.

Some insight on the dangers of filtering can be gained by examining the auto-correlation function for both the filtered turbulent signal and random white noise. Figure 3.6 shows the ensemble averaged auto-correlation coefficient (R_{pp}) of a typical wall pressure signal. When the signal is unfiltered (raw), R_{pp} decays rapidly from a value of 1.0 at $\tau=0$, but then flattens out and decays more slowly with τ. When the pressure signal is band pass filtered, R_{pp} reveals its components. The short time scales which give rise to the sharp peak at $\tau=0$ are captured by filters 2 and 3 in which the signal appears correlated with itself only for a short duration ($\tau^+ \leq \pm 50$). The filtering also results in more axis crossings in the correlation coefficient. As the
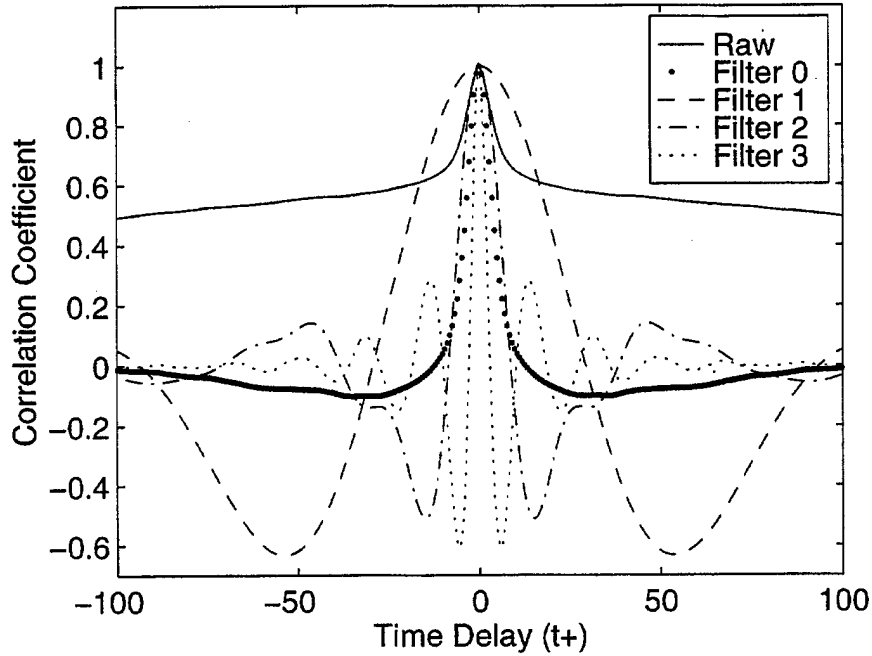
Figure 3.6: The effects of band-pass filtering on the auto-correlation function for wall pressure

cutoff frequencies of the bandpass filters are lowered, R_{pp} broadens while maintaining the same $\sin(x)/x$ shape of the higher frequency data. As the frequency bandwidth is expanded to include all relevant scales (filter 0), R_{pp} resembles a broad spike with minimal waviness before or after the peak. The presence of facility noise causes the raw pressure signal to appear correlated out to a very large τ.

When a random noise signal is filtered, the effect is similar (see figure 3.7). However for noise, the correlation coefficient (R_{nn}) of the raw signal is a narrow spike at $\tau=0$. As filtering is applied to the noise signal, a phenomenon known as filter "ringing" occurs and the correlation coefficient broadens and exhibits the same $\sin(x)/x$ like behavior seen in the pressure data. This behavior limits the usefulness of auto-correlation as a means of detecting coherent motions based on pressure or velocity signals that have been filtered in any way.
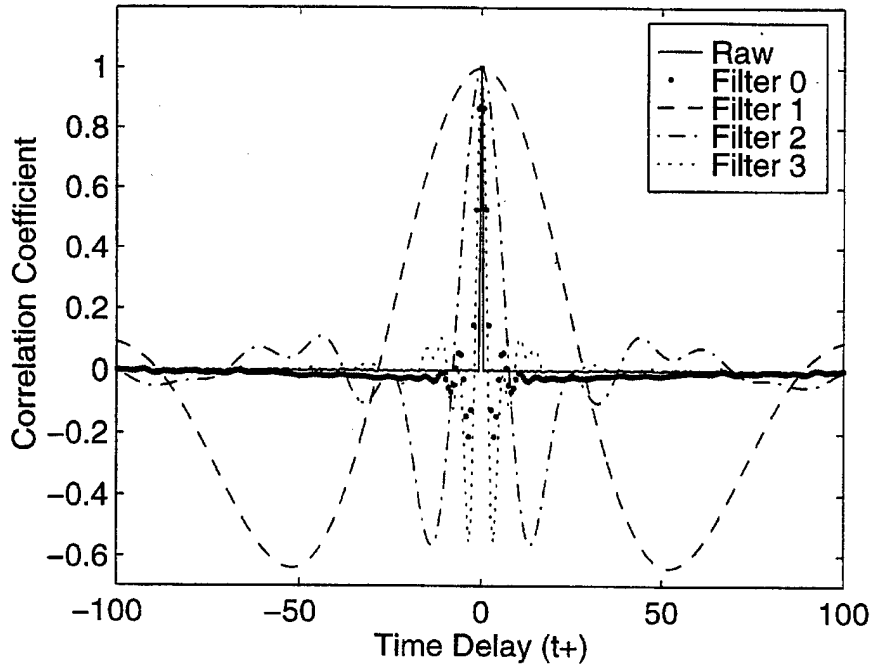
Figure 3.7: The effects of band-pass filtering on the auto-correlation function for white noise

Cross-correlation between two or more independently obtained signals turns out to be a more reliable tool for detecting coherent motions. Figure 3.8 shows the cross-correlation coefficient between two wall pressure signals from adjacent transducers in the streamwise array. Notwithstanding the magnitude at $\tau=0$ and the phase shift, the results are almost identical to the auto-correlations in figure 3.6. The peaks occurring at non-zero time delay are characteristic of a convecting pressure field.

While one could argue that the behavior of the auto-correlations in figure 3.6 is an artifact of the filtering, the cross-correlation is not so vulnerable. The cross-correlation between two independently derived noise signals is shown in figure 3.9. The temporal behavior of the cross-correlation is again dictated by the scales of the signal allowed by the filter, however, the magnitude of the correlation is essentially zero. Based on these observations, it was concluded that a significant cross-
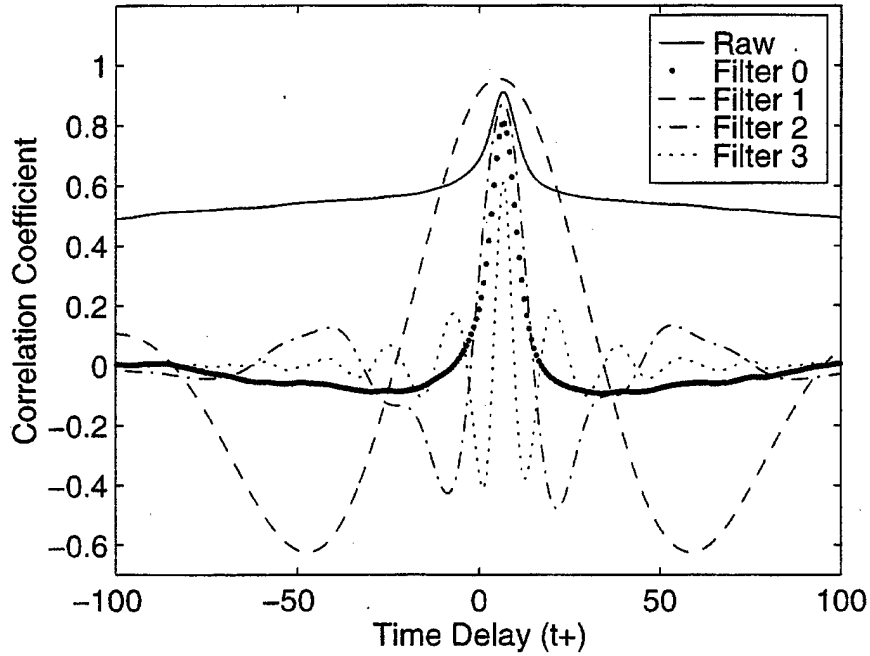
Figure 3.8: The effects of band-pass filtering on the cross-correlation function for wall pressure signals from two adjacent transducers in the streamwise array

correlation between turbulent signals (filtered or unfiltered) is a reliable indicator of coherent motions.

3.3.3 Filtering Effects on Conditional Sampling

The method of conditional sampling is also used extensively in this investigation to identify coherent motions in the boundary layer. Therefore, the same scrutiny has been applied to this method. Figure 3.10 shows the ensemble average of positive wall pressure peak events for a threshold of k=3. As with the auto-correlation functions, the shape of the events depends on the filtering of the original data. The average shape of the events in the low frequency filtered time records (filter 1) clearly reflect the time scales allowed by this filter. As the cutoff frequencies are increased, the average events shapes have a shorter duration and more associated peaks. The wavelet-like behavior of the filtered events is not evident in the raw or filter 0 event
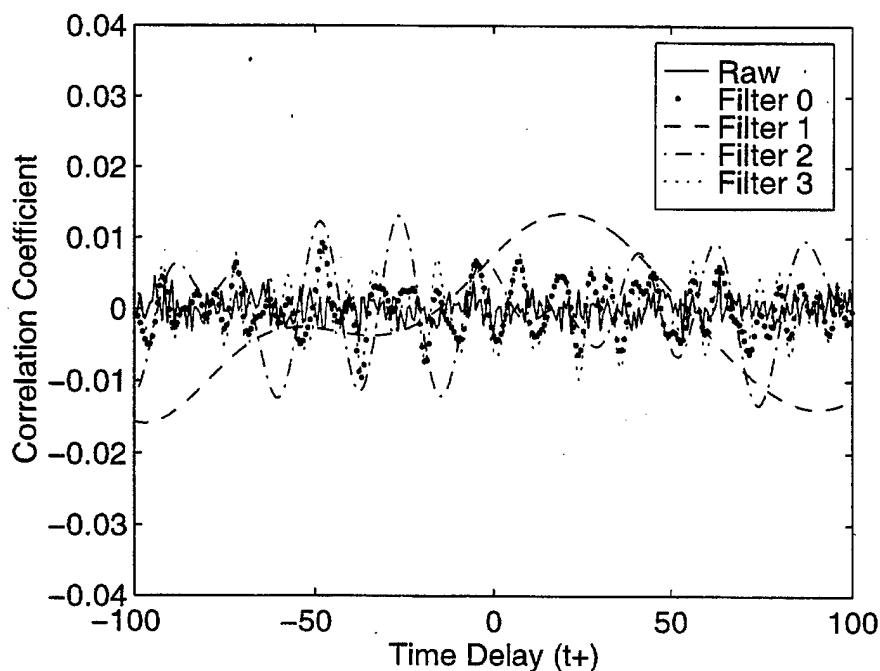
Figure 3.9: The effects of band-pass filtering on the cross-correlation function between two independently obtained white noise signals

shapes. The tails of the events seen when the data are filtered appear to be masked by the inclusion of events of all relevant scales. This phenomenon was seen by Karangelen [26] and is a manifestation of "phase jitter" in which the misalignment of events leads to a distorted ensemble average shape.

When the same filters are applied to white noise and the events are ensemble averaged, the results are quite similar and are shown in figure 3.11. They are, in fact, almost identical to the auto-correlation functions for white noise shown in figure 3.7. The average event shapes are clearly a function of the filtering, however, the event shapes of raw noise do not include any of the scales seen in the filtered noise events. This occurs for the same reason as it does in the auto-correlation function; white noise is not correlated with itself beyond $\tau=0$, so events in unfiltered noise are never more than one sample length in duration, i.e.., a narrow spike.
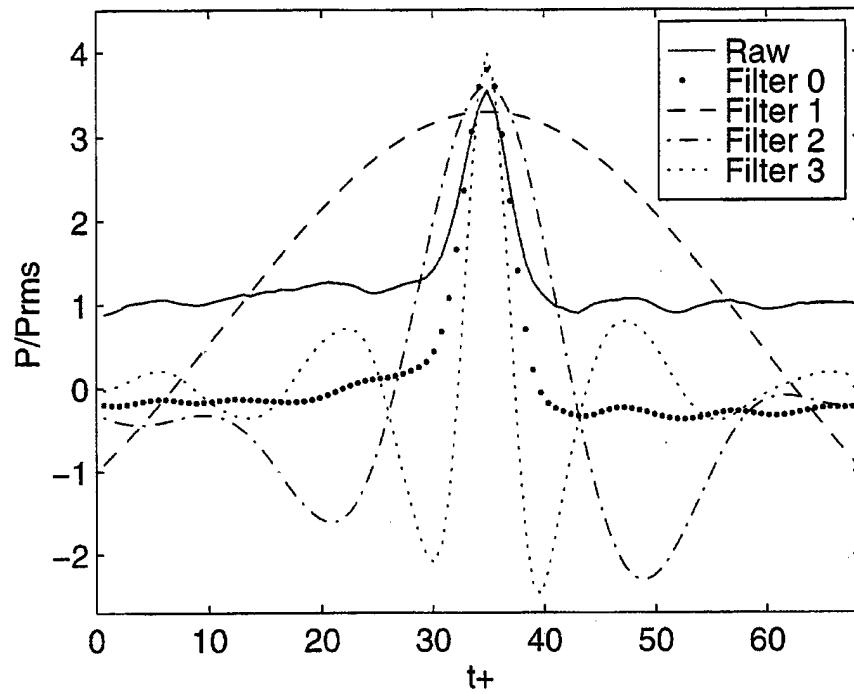
Figure 3.10: The effects of band-pass filtering on the ensemble averaged peak event shapes for wall pressure
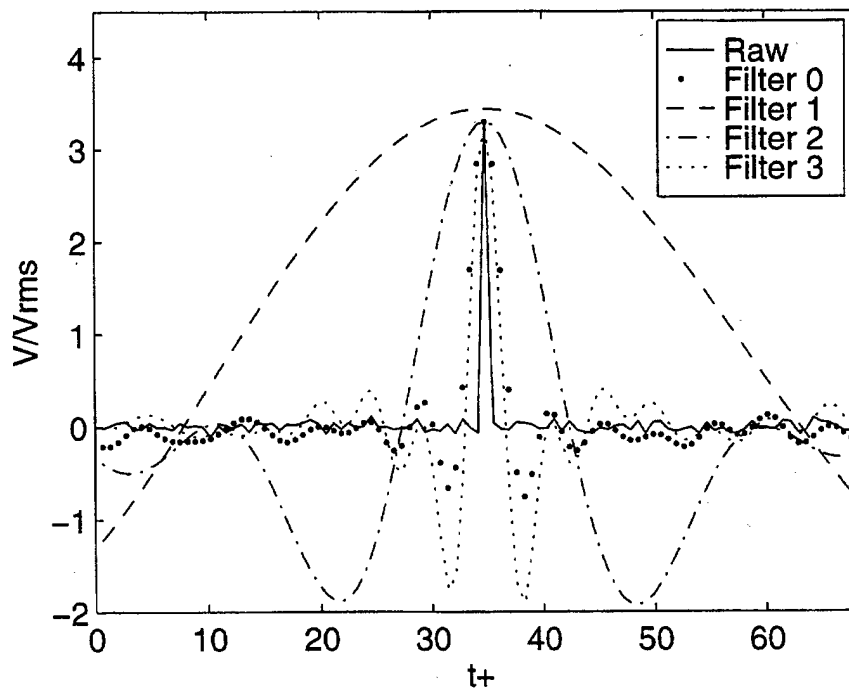
Figure 3.11: The effects of band-pass filtering on the ensemble averaged peak event shapes for white noise
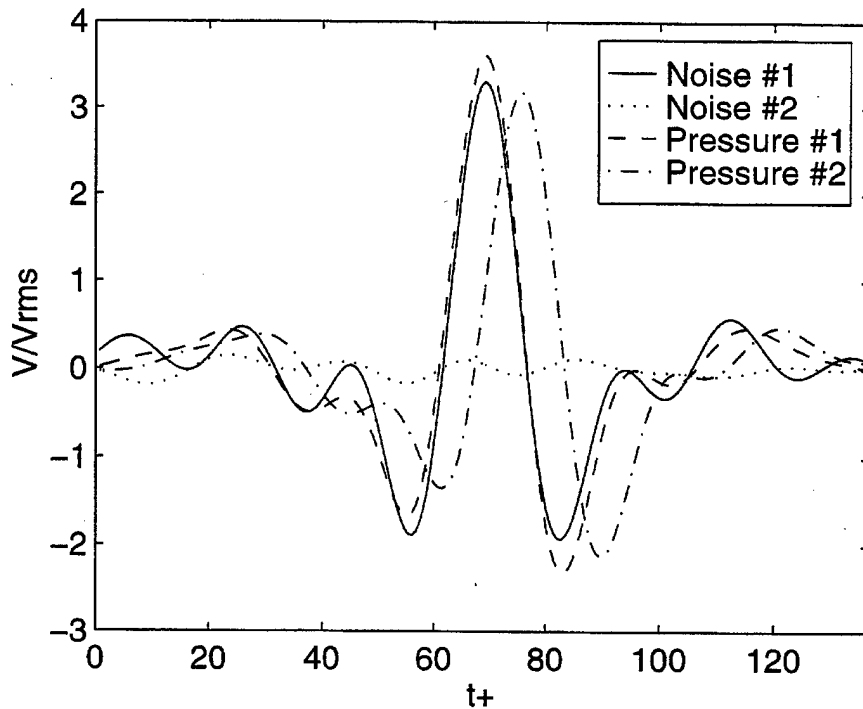
Figure 3.12: Conditionally averaged peak event shapes for filtered noise versus filtered wall pressure

The interpretation of average event shapes must therefore be done with great care. One must be certain, as with auto-correlation, that the influence of filtering as well as other issues discussed in Section 1.2.2 are accounted for.

Conditional sampling of one signal based on events detected in another independently derived signal is a robust method of correlating two signals. It allows one to avoid many of the dangers of interpreting auto-correlation or single-channel conditional averaging. In this case, if two signals are uncorrelated, they remain uncorrelated despite any filtering applied to them. Figure 3.12 illustrates this point. In this figure, the wall pressure signals (subject to filter 2) from two adjacent transducers in the streamwise array are conditionally sampled and ensemble averaged based on peak events (k=+3) occurring in the upstream transducer signal. The average event shapes are nearly identical for both transducers but are out of phase due to

convection of the pressure sources in the flow. Similar data from two independently derived white noise sources are also shown. Conditional sampling reveals no correlation between the two filtered noise signals. Clearly, the physics revealed in the two pressure signals is not an artifact of the filtering.

3.3.4 Filtering Effects on Wall Pressure Event Statistics

The effect of bandpass filtering on wall pressure peak event detection is illustrated in table 3.2 which shows the number of events detected as well as characteristics of the events for each filter used in this investigation. Also shown in table 3.2 is the resultant RMS level of the filtered time record. Clearly, a large amount of energy is removed from the signal simply by removing facility and electrical noise with filter 0. Furthermore, despite the bandwith of filter 1 ($\Delta f = 200$ Hz) being much less than the bandwidth of filter 3 ($\Delta f = 3800$ Hz), the RMS level of the resulting time records are comparable. This is an important observation since it has been assumed that by removing the scales associated with filter 1, one is removing the influence of the induced irrotational flow.

The effect of filtering on the total number of events detected is not surprising. As the frequency band of the filters is increased (filter 1 to filter 3), the number of events detected rises dramatically while the average time between events (ΔT) as well as their average duration falls proportionately. This effect was seen by Kammeyer [25] using a "high frequency" wavelet filter. The low number of events detected in the raw pressure signal is a result of normalizing by such a large RMS value.

The fraction of the time record occupied by the large amplitude events (% time) and their percent influence on the filtered RMS level of the signal reveal an important characteristic of the wall pressure signal. As the frequency of the filters increases, there are more events detected and their contribution to the RMS energy in the

Table 3.2: Filter effects on wall pressure event statistics (k=3)

Filter	RMS (Pa)	# of Events	% Time	% RMS	$\triangle T$	Duration
Raw	2.298	175	13.33	36.48	3678	249.75
0	1.240	722	5.25	24.42	906	23.72
1	0.529	70	1.76	9.70	9214	82.29
2	0.859	389	2.81	18.00	1680	23.62
3	0.621	1584	3.58	32.17	411	7.38

Table 3.3: Filter effects on white noise event statistics (k=3)

Filter	RMS (V)	# of Events	% Time	% RMS	$\triangle T$	Duration
Raw	1.000	878	0.56	3.49	745	2.08
0	0.524	565	1.33	6.31	1160	7.68
1	0.098	53	1.34	7.33	12330	82.50
2	0.226	175	1.14	6.23	3614	21.23
3	0.460	612	0.84	5.45	1065	4.48

filtered signal rises proportionately. However, when considering their contribution to the total energy in the unfiltered signal, the contribution of the high frequency events is disproportionately larger than that of the events detected in the low frequency signals. This occurs because of the temporal characteristics of the high frequency events, that is, large amplitude and short time scales result in energy imparted on the wall in a short period of time.

The equivalent event statistics for a filtered white noise signal are shown in table 3.3. The white noise time record analyzed was the same length as the wall pressure signal from table 3.2 and was filtered using the same sampling frequency (f_s=32768 Hz). The most obvious difference from the wall pressure event statistics is the far fewer number of events detected. And while more events are detected in the higher frequency signals, unlike wall pressure, their contribution to the % time and % RMS do not increase.

In general, these effects illustrate the physical features of wall pressure discussed in detail by Karangelen [26] and Wilczynski [53]. Despite the sharp rolloff of the

wall pressure spectrum in the frequency range of filter 3, a pressure signal filtered in this range contains an abundance of intermittent, large amplitude events. These events contribute disproportionately to the total wall pressure field and can not be neglected.

Chapter 4

RESULTS ON SPACE-TIME CHARACTERISTICS OF WALL PRESSURE EVENTS

As previously stated, there are three fundamental objectives of this investigation. They are, in short: to discriminate active from passive turbulent structures, to track both the near wall and large scale active structures, and to obtain the wall pressure signatures of these composite structures. The data to be presented in this chapter are from the first set of experiments: measurements of fluctuating wall pressures with an array of transducers in both the streamwise and spanwise directions. Two distinct databases were acquired from these tests. Each of these databases were then filtered using filters 0,1,2 and 3. This chapter will contain a discussion of post processing analyses of these filtered databases in order to address the basic objectives.

In Section 4.1, experimental results which illustrate the spatial extent and life cycle of wall pressure events are presented for each of the filtered databases. Correlations between large scale and small scale turbulent signatures are examined using the concurrent filtered time records from the array in Section 4.2. Attempts to track the growth and decay of wall pressure signatures of both large and small scale structures with data from the streamwise transducer array are given in Section 4.3.

Finally, a summary of these findings will be presented in Section 4.4.

4.1 Spatial Extent of Wall Pressure Signatures

Using the correlation techniques described in Chapter 3, temporal records from the streamwise and spanwise transducer arrays were analyzed for information about the space-time characteristics of the wall events. These methods include spectral analysis, cross-correlation measurements, and conditional sampling. Using the results of these analyses, an attempt will be made to demonstrate the spatial extent of the wall pressure signatures of organized structures. These findings will be presented first for the streamwise transducer array and then for the spanwise array.

4.1.1 Streamwise and Convective Features

Cross-Spectral Techniques

The wall pressure field beneath a turbulent boundary layer has historically been studied with spectral analyses [8, 9, 16, 55]. Measurement of the cross-spectrum of the wall pressure field provides information about the spatial and convective properties of the pressure producing turbulent structures. In this investigation, the cross-spectrum is expressed in terms of its normalized magnitude (coherence) and phase (convection velocity). The phase is expressed in terms of the convection velocity which was shown by Blake [7] to be related by $U_c(\omega, \Delta x) = \omega \Delta x / \Theta(\omega, \Delta x)$, where Δx is the streamwise separation between the transducers, and the cross-spectrum Θ is the phase angle in radians.

Farabee [16] conducted a thorough investigation of the spanwise and streamwise cross-spectral properties of the wall pressure field for an equilibrium and disturbed turbulent boundary layer. In general, the cross-spectral measurements from the streamwise and spanwise arrays in this investigation are consistent with Farabee's

61
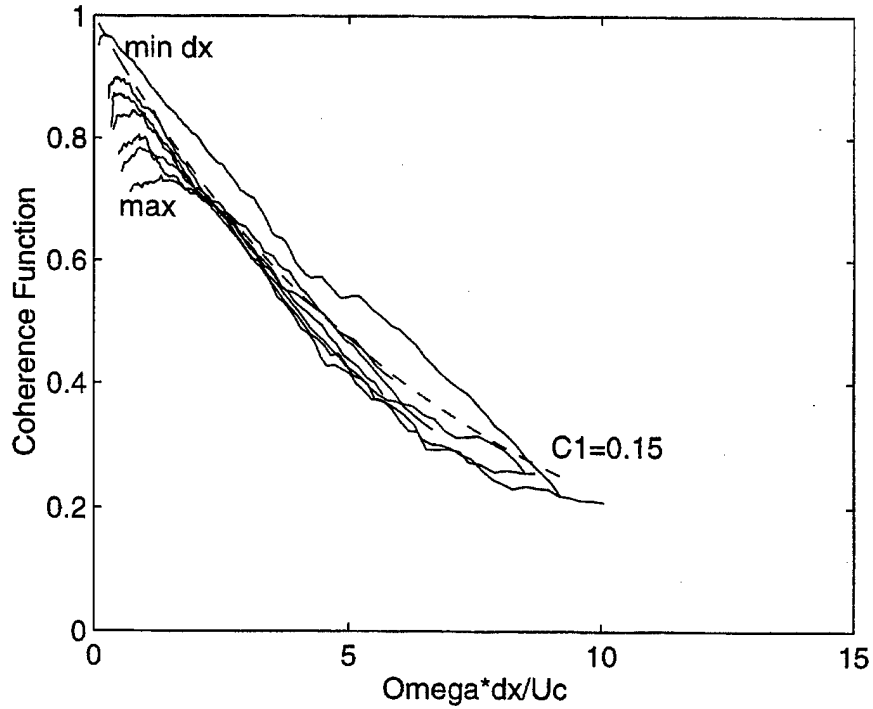
Figure 4.1: The coherence function between transducer pairs in the streamwise array

equilibrium results. Figure 4.1 shows the coherence functions measured between the upstream-most transducer with the remaining transducers in the streamwise array. The minimum spacing, labeled "min" in the figure, was 1/10-inch; the maximum spacing measured was 7/10-inch. The coherence function is plotted against the phase of the cross-spectrum, $\omega \Delta x / U_c$.

The first trend observed in figure 4.1 is the collapse of the high frequency portion of each curve onto a universal curve for all transducer spacings. This Strouhal number similarity scaling behavior is classical and was seen by Bull [9] and Farabee [16]. Also shown in figure 4.1 is a line indicating an exponential decay function proposed by Bull [9] in which he assumed that the coherence function, Γ, behaved according to :

$$\Gamma(\omega, \Delta x) = e^{-C_1 |\omega \Delta x / U_c(\omega, \Delta x)|},$$
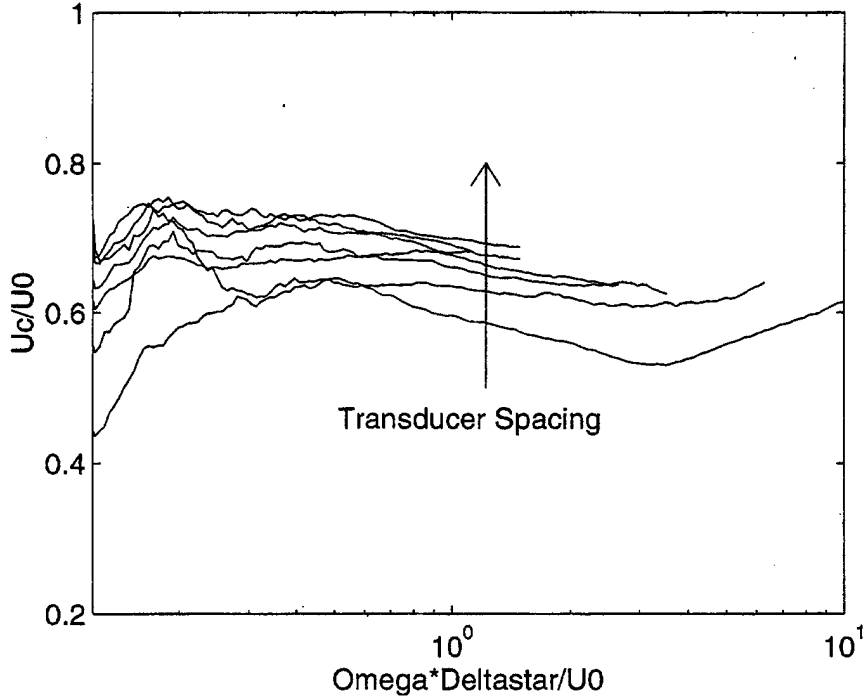
Figure 4.2: The measured convection velocity between transducer pairs in the streamwise array versus $\omega\delta^*/U_0$

in the region of similarity scaling. The current data was best fit using a coefficient, C_1, of 0.15 which is within the range of reported decay rates.

The lack of similarity scaling in the low frequency portions of the curves is consistent with the results of previous investigators [8, 9, 16, 37] and is a physical requirement of the wall pressure field. As discussed in Farabee [16], for the coherence function to asymptotically approach unity at low frequency would require that large scale pressure source terms in the boundary layer convect over large distances without being distorted by gradients in the mean flow. This obviously does not occur.

The phase of the wall pressure cross-spectrum is shown in figure 4.2 in the form of convection velocity plotted against Strouhal number, $\omega\delta^*/U_0$. These results are also in qualitative agreement with those of previous investigators [16, 6]. The convection

velocity for all transducer separations increases initially with frequency, peaks at a Strouhal number of $\omega\delta^*/U_0 \approx 0.2$, and levels off to an asymptotic value. The magnitude of the convection velocity measured in this way appears to increase (at all frequencies) with transducer spacing. This behavior illustrates the dispersive character of the wall pressure field; fluctuations of the same length scale convect at different speeds.

This method of measuring convection velocity is but one of several methods explored in this investigation. Cross-correlation and conditional sampling measurements will be shown to yield comparable results. Although cross-correlation is mathematically related to the cross-spectrum through the Fourier transform, it has one advantage that will be exploited throughout this investigation. By analyzing and presenting wall pressure measurements in the time domain, rather than in the frequency domain, one can compare the effects of signal processing (filtering) on the correlation between spatially separated signals.

Correlation Techniques

The correlation coefficient, $R_{pp}(\tau)$, was computed between the upstream-most transducer (p1) and each of the remaining transducers in the streamwise array (p1 to p8). This computation was made over a segmented time span, ΔT, and then repeated for successive time spans until the end of the time record was reached. The individual correlation functions were then ensemble averaged. Typical results of this computation are shown in figure 4.3. The average correlation coefficients were computed using pressure time records that were subjected to filters 0,1,2 and 3.

Figure 4.3a shows $R_{pp}(\tau)$ for wall pressure time records subjected to filter 0, which is the baseline data, free from background and electrical noise. There are several distinctive features of these data that are worth discussing. The first is the

exponential decay with streamwise distance of the magnitude of the maximum correlation. This behavior is consistent with the exponential decay of the coherence function (figure 4.1) which was computed from unfiltered wall pressure signals. As the separation distance between the transducers is increased, the maximum correlation value decays and the width of the correlation function broadens. This is also consistent with the spectral results which showed the influence of the large scale, low frequency pressure fluctuations increases with transducer separation. The scales of the turbulent structures which remain well correlated across the length of the array define the shape of the correlation function between first and last transducers. These scales are larger than those which only remain correlated across the two upstream-most transducers.

The purpose of filter 1 was to isolate the scales which are associated with turbulent structures in the outer-irrotational flow. The cross-correlation function computed for the same transducer pairs as figure 4.3a for time records subjected to filter 1 are shown in figure 4.3b. The shape of $R_{pp}(\tau)$ changes dramatically when only a narrow band of frequencies (scales) is considered. Along with the slower decay rate of the maximum values, the overall shape of the correlation is quite different. Rather than the pulse-like shape of the broad band (filter 0) correlation function, $R_{pp}(\tau)$ for the low frequency (filter 1) appears more wave-like, with more of a tendency to overshoot or oscillate. By removing the high frequency components of the wall pressure signal, a physically relevant correlation function of the pressure sources due to the irrotational flow is exposed.

The same general trend is observed as the filter cutoff frequencies are increased (filters 2 and 3). As shown in figures 4.3c and 4.3d, as the frequency bands increase, so does the number of discernible peaks in the cross-correlation functions. Hijikata, Suzuki, and Iwana [19] observed similar trends between frequency components in

65
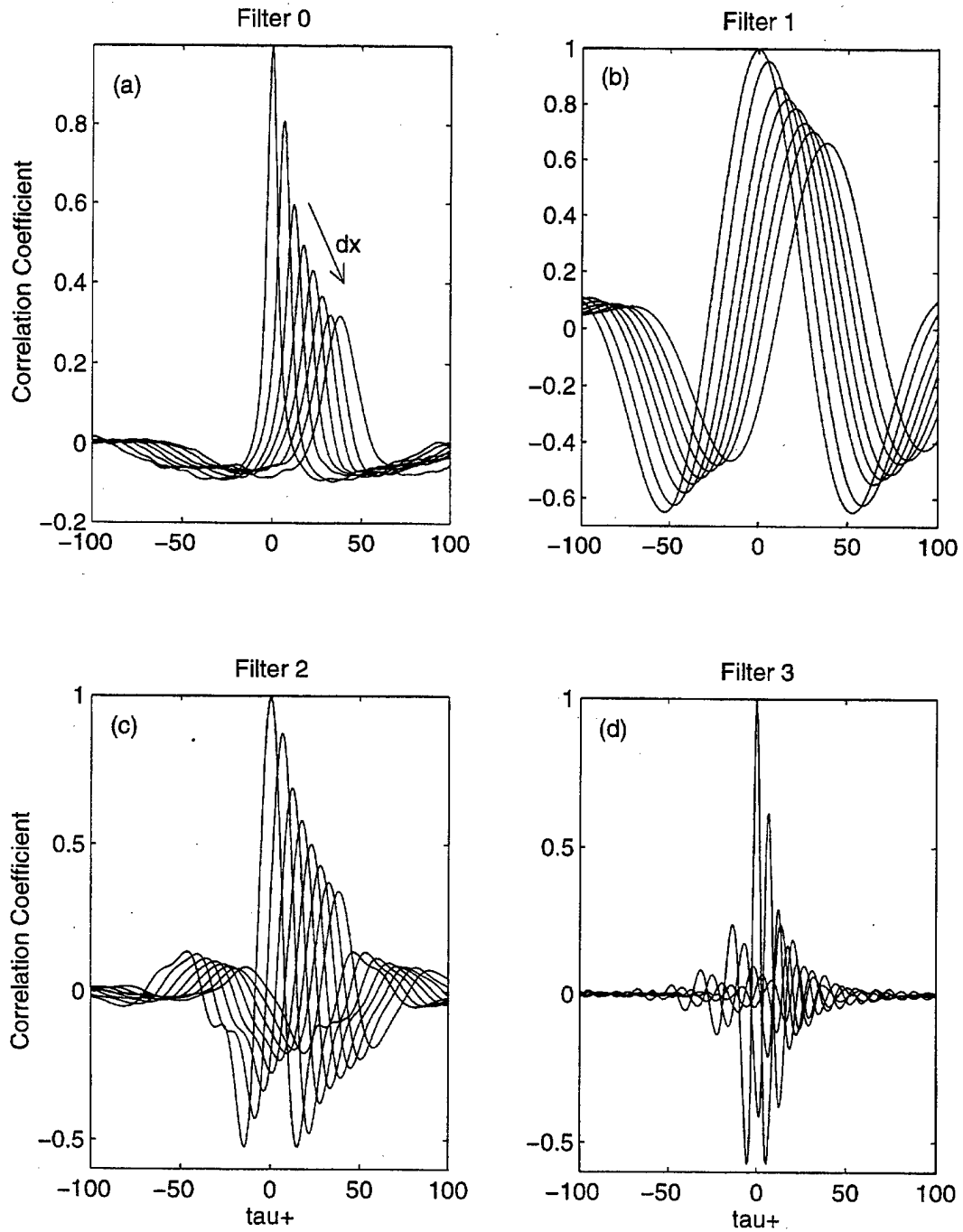
Figure 4.3: The ensemble averaged correlation function between transducer pairs in the streamwise array (a) unfiltered, (b) filter 1, (c) filter 2, (d) filter 3

pressure-velocity cross-correlation functions. The correlation data of Naguib and Wark [36] between band pass filtered shear stress and streamwise velocity measurements show the same tendency to oscillate more as the frequency of the filters is increased.

The spatial decay rates of the maximum cross-correlation for each of the filters tested are replotted versus streamwise distance in figure 4.4a. It appears from these curves that the decay rate of $R_{pp}(\tau)_{max}$ of the wall pressure signals is highly dependent on the filtering applied. From these data it would appear that high frequency (filter 3) wall pressure activity is only correlated to one half the boundary layer thickness ($\delta/2$) in the streamwise direction.

The convection velocity of the wall pressure field may also be computed from the time delay between peaks in the correlation functions ($\Delta\tau$) and the separation distance (Δx) between the transducers, $U_c(\Delta x) = \Delta x/\Delta\tau$. Results of this computation, using the upstream-most transducer as the reference, are shown in figure 4.4b. Two important trends are observed in these data. First, as the transducer separation increases, the convection velocity rises slightly. This agress with the spectral results presented earlier. More important however, is the variation of U_c with the choice of filtering. U_c computed from broadband data (filter 0) as well as that from filters 2 and 3 appears to collapse on the same line, varying from $U_c/U_0 \approx 0.6$ to 0.7 across the array. The scales associated with filter 1, those in the outer-irrotational flow, convect at consistently higher velocities across the array.

If one assumes that filters 1,2, and 3 successfully discriminate between turbulent scales, then the results depicted in figure 4.4 provide insight into the relationship between these scales. It appears that the scales associated with filters 2 and 3 convect at approximately the same speed and this speed corresponds to that measured by cross-correlation functions of the broad-band (filter 0) data.
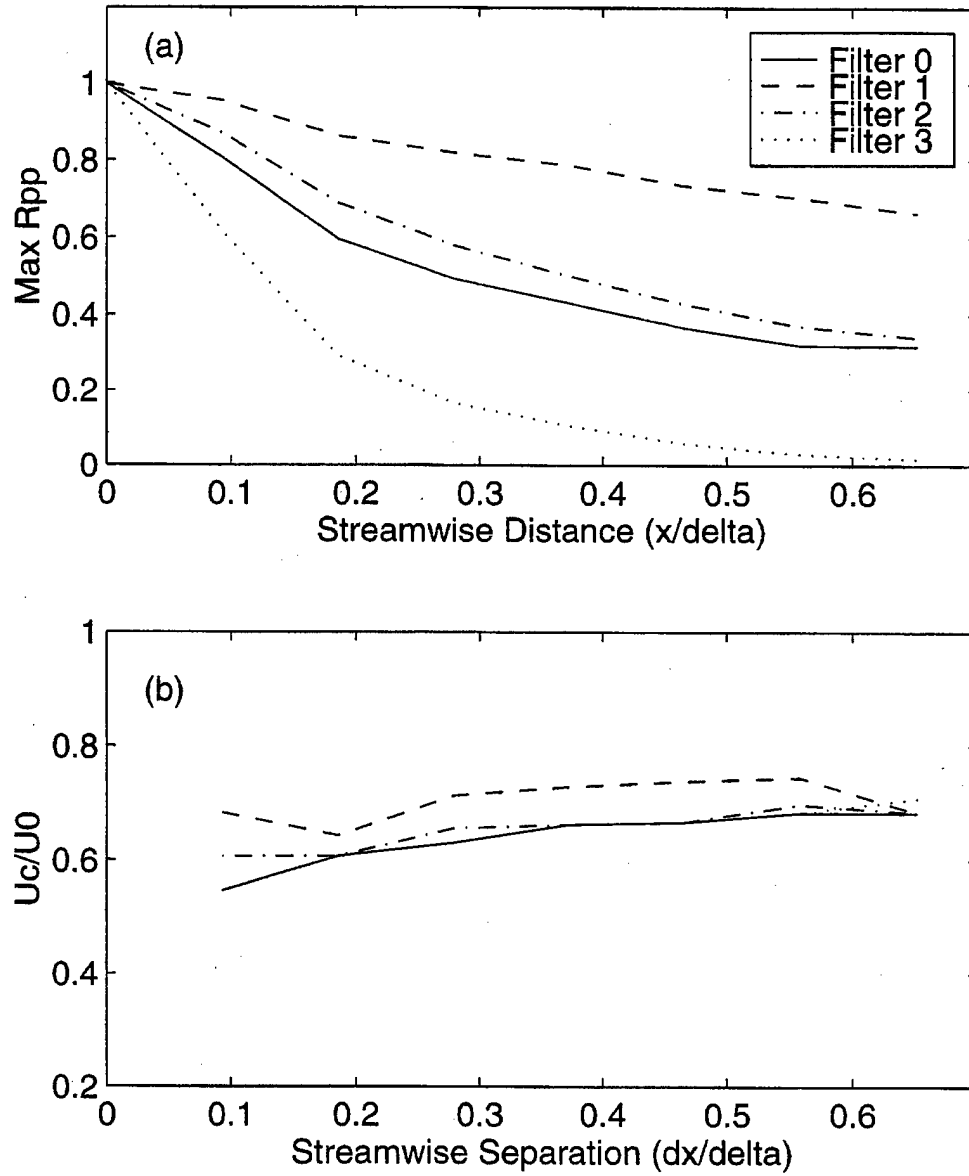
Figure 4.4: Convective features of cross-correlation function for streamwise array (a) mean decay of peak correlation coefficients, (b) convection velocity based on mean time between peaks

Some comments are in order regarding the near-wall structures associated with the high frequency wall pressure data (filter 3). As shown in figure 4.4a, the magnitude of the cross-correlation of the high frequency wall pressure signal decays rapidly with transducer separation. These pressure signatures are generally attributed to burst events in the near wall region. This would suggest that the spatial influence of the ejection/sweep processes are limited to 3 or 4 transducer spacings in the streamwise direction. As will be shown in subsequent analyses of the data, this is not the case. The spatial influence of these near wall structures is much larger. A shortcoming of the standard cross-correlation function is that it fails to illustrate the true influence of these scales because the pressure signature of these structures changes quickly from one transducer to the next. A more appropriate method of measuring the spatial influence of these burst events is to correlate the wall pressure signals based on a measure of the localized energy contained in clusters of these short time events.

VITA Techniques

The VITA method is an attempt to measure localized temporal activity. Figure 4.5 shows the normalized correlation between the VITA functions at two streamwise transducers computed exclusively from filter 2 and filter 3 wall pressure signals. Integration times of $T_w^+ \approx 52$ and $T_w^+ \approx 12$ were used in the VITA calculation for the respective filters. These values were based on the median time scales in the bandwidth of the filters. The $T_w^+ \approx 12$ value was also consistent with Kammeyer's [25] VITA calculation of wavelet filtered data. The results for filter 2-filter 2 and filter 3-filter 3 correlations show consistently strong correlations over the spatial extent of the streamwise array for both the pressure signatures of the large scale intermittent structures (filter 2) and the near-wall burst events (filter 3). This method of detection

and correlation sheds new light on wall pressure signatures of large and small scale turbulent motions.

By comparing figure 4.3d and figure 4.5b an important feature of high frequency wall pressure signals is revealed. *That is, the appearance or shape of individual near-wall burst events are distorted as they convect downstream, deteriorating the cross-correlation of the temporal records between transducers. However, the cluster of turbulent activity associated with the event, identified by the VITA calculation of the signal's variance, remains well correlated as it convects the length of the transducer array. And as shown in figure 4.4b, this cluster of burst activity appears, qualitatively, to convect with the same speed as the larger "central" structures associated with filter 2.*

Conditional Sampling Techniques

The cross-spectral, cross-correlation, and VITA techniques presented so far do not specifically address individual wall pressure events, but rather, are used describe the wall pressure field in a statistical framework. Conditional sampling and ensemble averaging of wall pressure peak events is another approach that can yield similar information on the spatial and convective properties of the wall pressure field. However, with this approach, the intermittent, high amplitude wall pressure fluctuations can be extracted from the total signal and examined for their own spatial and convective features.

Conditional sampling results from the streamwise array are shown in figure 4.6. These figures require some explanation. Wall pressure signals from each transducer were conditionally sampled based on detection of peak events (k=+3) occurring at the upstream-most transducer (p1). The signals from each of the transducers were then ensemble averaged over a fixed time window centered at the peak detection
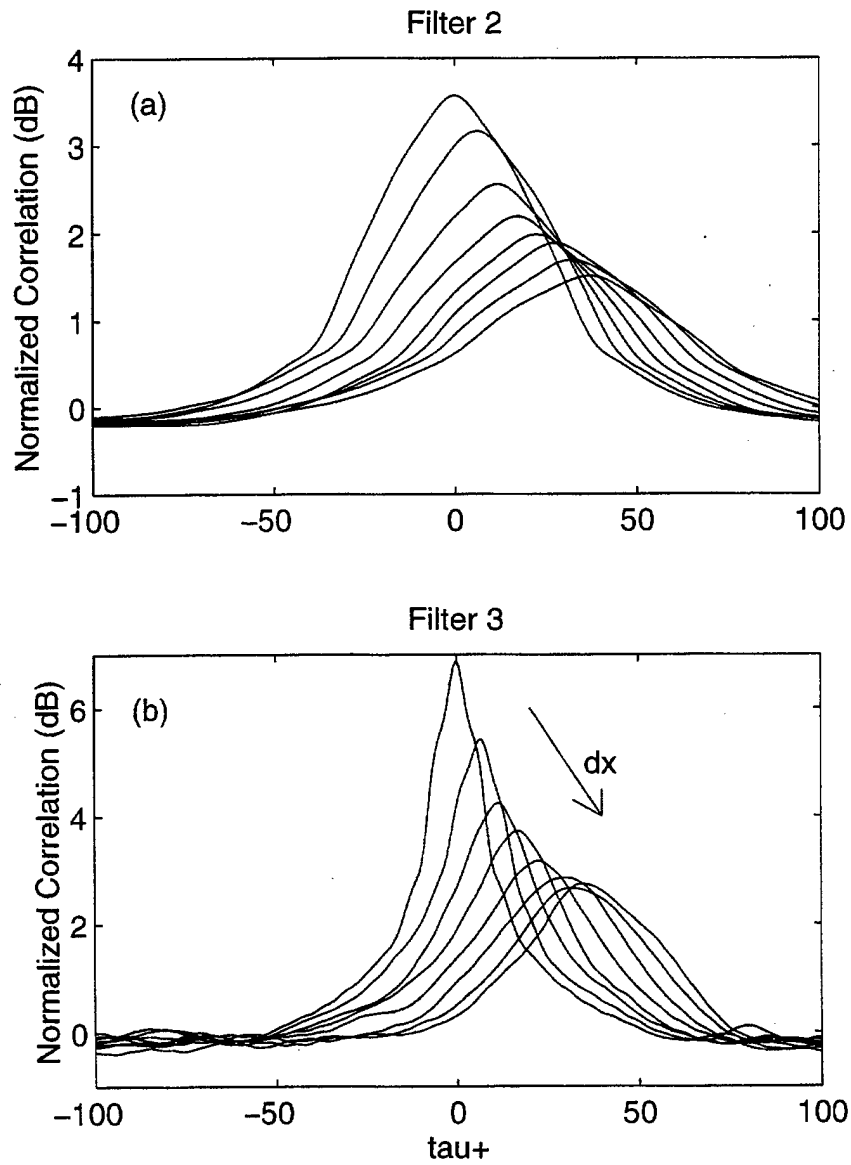
Figure 4.5: Normalized correlation based on the localized variance (VITA) functions of filtered wall pressure signals from the streamwise array, (a) filter 2, (b) filter 3

time. This computation was performed on time records that were subjected to filters 0,1,2, and 3. The conditionally averaged event shapes at each of the eight transducers in the array are shown in separate plots for each of the filtered time records.

Figure 4.6a shows the event shapes for the noise-free (filter 0) wall pressure data. The results are similar to those of Schewe [45] who used a four element array and a peak threshold of 3.2. The average shape of the events is similar to the shape of the corresponding correlation functions in figure 4.3a. The signal shapes are pulse-like peaks with little tendency to overshoot before or after the peak. As the distance between the transducers increases, the average event shape broadens and decays exponentially in magnitude.

There are several possible reasons for the decay and broadening of the event shapes with streamwise distance. Schewe [45] cites the decay of the individual events and the different convection velocities of the individual events as the reasons for the broadening behavior. There is more likely a complex combination of peak event decay, varying convection speeds, and the influence of large and small turbulent scales affecting the downstream shape of the wall pressure events. As with the correlation functions of filter 0 wall pressure, there is no discrimination between scales. The events detected at the reference transducer include large scale and small scale events which collectively exceed the given threshold. As the distance between the transducers increases, the shape of the correlation function as well as the average event shape becomes dictated by the scale of the events which remain correlated over that distance, i.e., the larger scale turbulent structures.

When certain scales are discriminated prior to event detection and conditional averaging, the event shapes do not change significantly with downstream distance. Figure 4.6b shows this effect for the filter 1 event shapes. Again, like the correlation

72
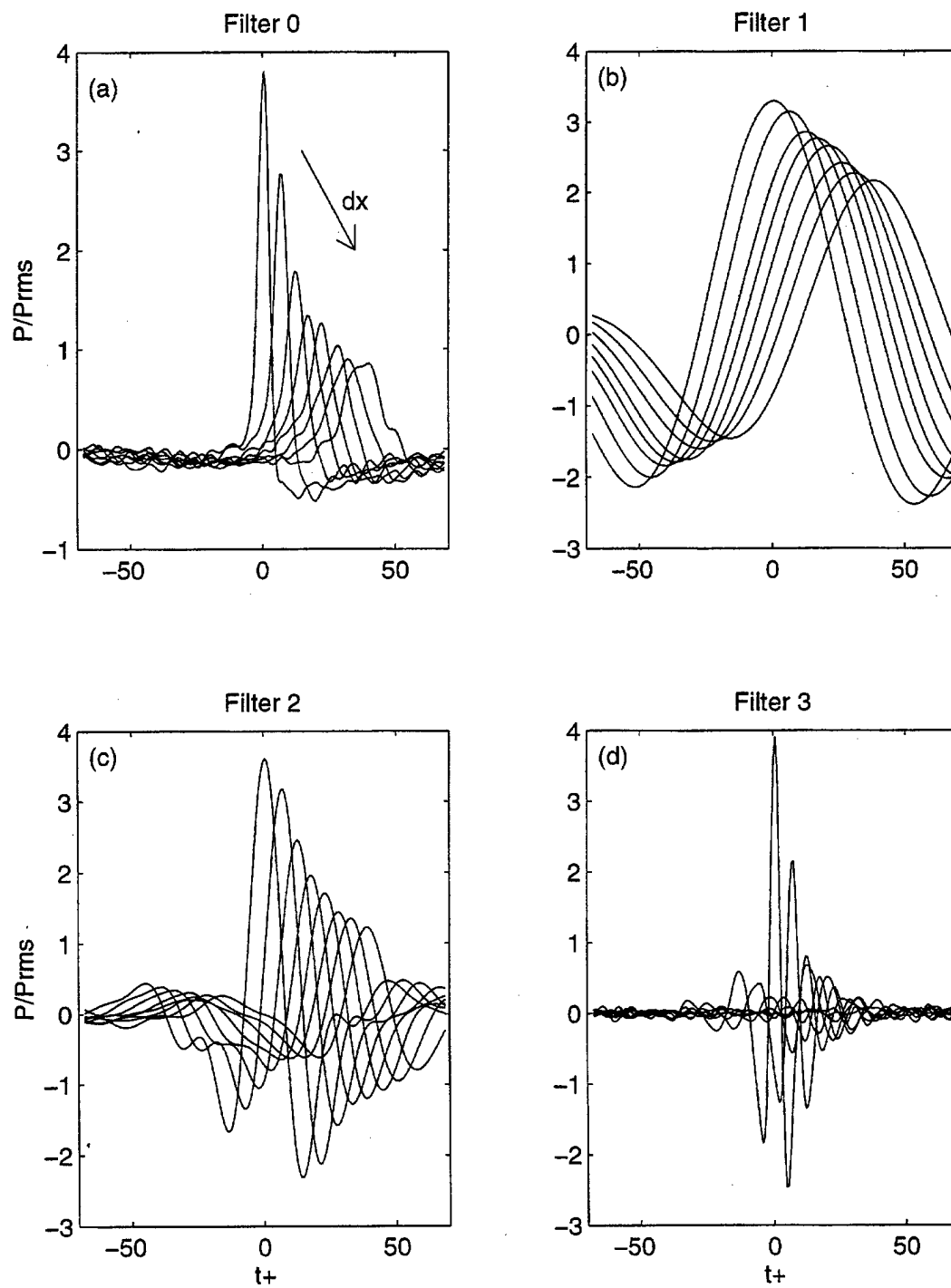
Figure 4.6: Downstream wall pressure signals conditionally averaged on peak wall pressure events (k=+3) at the first transducer in the streamwise array (a) unfiltered, (b) filter 1, (c) filter 2, (d) filter 3

function, the decay rate of the event magnitude is slower. But unlike the filter 0 data, the width of the event shapes remains essentially unchanged across the array. In addition, the tails of the event shapes, before and after the peak are revealed by removing the high frequency fluctuations from the signal. The same is true for the event shapes of the filter 2 and filter 3 data shown in figures 4.6c and 4.6d, respectively. Similar to the correlation functions, the exponential decay rate of the peaks increases with the cutoff frequencies of the filters.

Another technique for determining the mean convection velocity, U_c, is by measuring the time delay between peaks in the conditionally averaged event shapes. The results for each of the four filters is shown in figure 4.7. U_c/U_0 varies between approximately 0.55 and 0.7 over the range of separations examined. These data compare favorably with the results of Schewe [45] ($U_c/U_0 = 0.53$) who tracked the centroid of the event shapes, as well as with the results of Thomas and Bull [50] ($U_c/U_0 = 0.67$) who defined U_c by the displacement of the zero axis crossing in downstream event shapes. These results are also consistent with the convection velocity results of Kammeyer [25]. The nominal increase in U_c with transducer separation seen in the correlation results is also observed in these data. The collapse of the filter 2 and filter 3 curves on the filter 0 curve is not as apparent as with correlation results, however, the events sampled in the filter 1 time records appear to convect consistently faster than the events detected in the other signals.

The convection velocity results presented so far (spectral, cross-correlation, and conditional sampling) have consistently shown that wall pressure events associated with the scales defined by filters 2 and 3 have convection velocities U_c/U_0 between 0.55 and 0.7. This places the center of these pressure sources at ($50 < y^+ < 250$), the log-law region of the boundary layer.

74
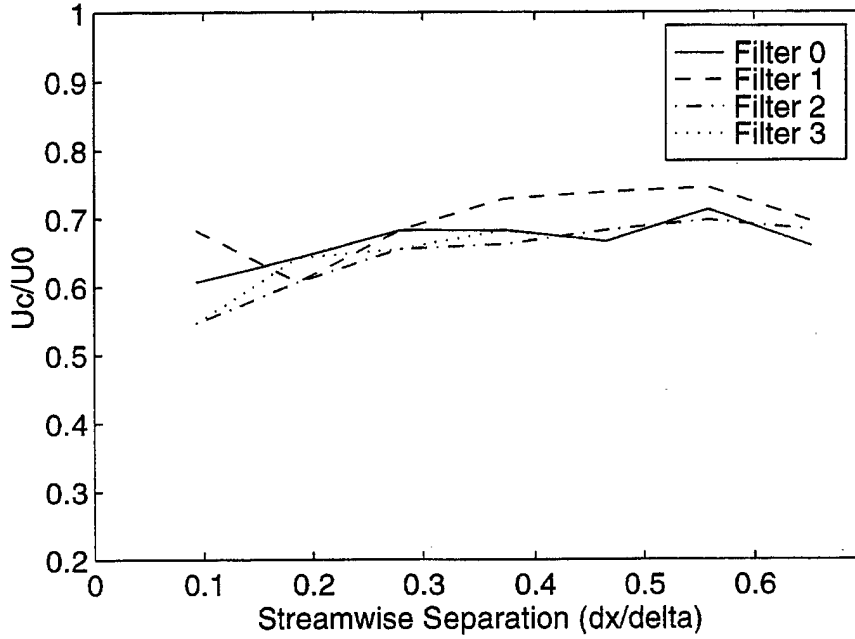
Figure 4.7: Measured convection velocity based on time between peaks in the stream-
wise conditionally averaged wall pressure events

4.1.2 Spanwise Features

Some techniques used for the data obtained with streamwise wall pressure mea-
surements were also applied to measurements from the spanwise array. Again, the
spatial extent of the wall pressure field will be examined by cross-spectral, cross-
correlation, and conditional sampling/ensemble averaging techniques applied to the
data acquired from the spanwise array. These findings will be briefly summarized.

The **spanwise coherence functions** between transducers pairs in the array are
plotted against Strouhal number in figure 4.8. The Strouhal number in this case is
of the form $St = \omega \Delta z / U_c$, where the convection velocity is taken from the stream-
wise phase measurements with the equivalent transducer spacing. The spanwise
coherence curves are consistent with the results of previous investigators [16, 9].
The exponential decay curve, with constant $C_2=0.9$, suggested by Farabee [16] is
also shown. The high frequency portions of the coherence curves collapse on this
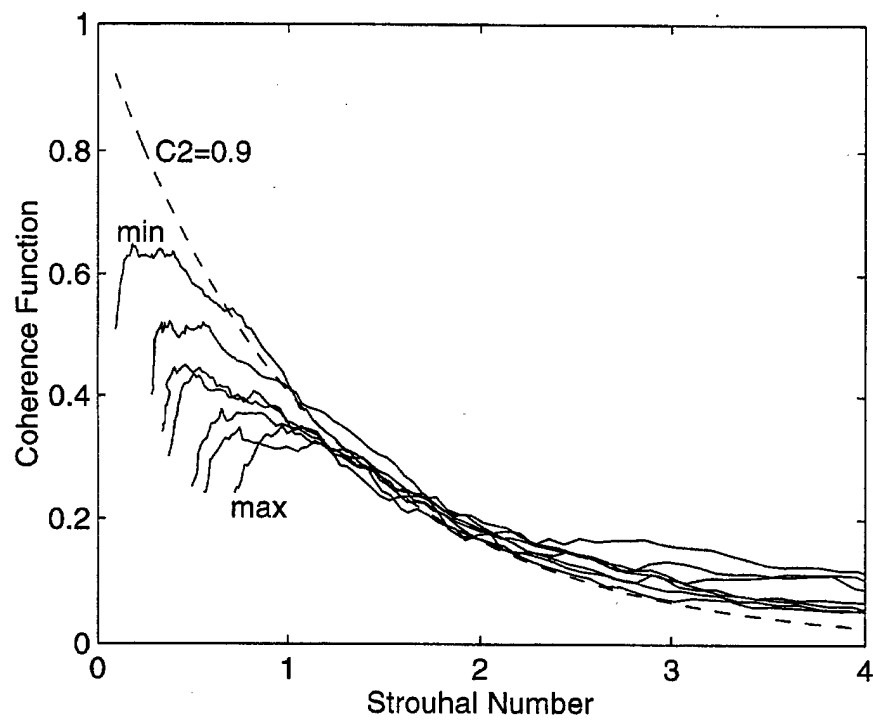
Figure 4.8: Coherence function between transducer pairs in the spanwise array, Strouhal No. $=\omega\delta^*/U_0$

universal decay curve. As with the streamwise coherence, the curves deviate from the similarity scaling at low frequency. Finally, the wall pressure field is coherent over a shorter spanwise distance than streamwise distance as indicated by the larger exponential decay constant, C_2.

The average **cross-correlation function** was computed between the first, reference transducer and the remaining transducers in the array. The results of this computation for pressure signals subjected to all four filters are shown in figure 4.9. Many of the features observed in the streamwise correlation functions are present in the spanwise data, including the exponential decay of the peak magnitude with transducer separation. The broadening of the correlation functions with transducer separation is also seen in the filter 0 data. As with the streamwise correlation, the quantity and magnitude of positive and negative peaks in the tails of the main peak increases with the cutoff frequencies of the filter.

Other than the obvious lack of convection, the most significant difference between the streamwise and spanwise cross-correlation functions is the larger decay rate of the peak magnitudes with spanwise separation. Figure 4.10 compares the decay rates for the four filters tested. The wall pressure signal subjected to high frequency filtering (filter 3) is essentially un-correlated beyond a spanwise separation of one transducer diameter ($\Delta z/\delta \approx 0.1$). The wall pressure field in the frequency band of filter 1 appears to be well correlated across the entire array. And as with the streamwise correlations, the decay rate of the unfiltered (filter 0) wall pressure and that subject to filter 2 appear to coincide.

In contrast to the standard temporal correlations shown in figure 4.9d, the normalized correlation function based on the variance of the high frequency (filter 3) wall pressure signals expands the spanwise extent of near wall burst events. As shown in figure 4.11, the **VITA technique** reveals the larger spanwise influence of
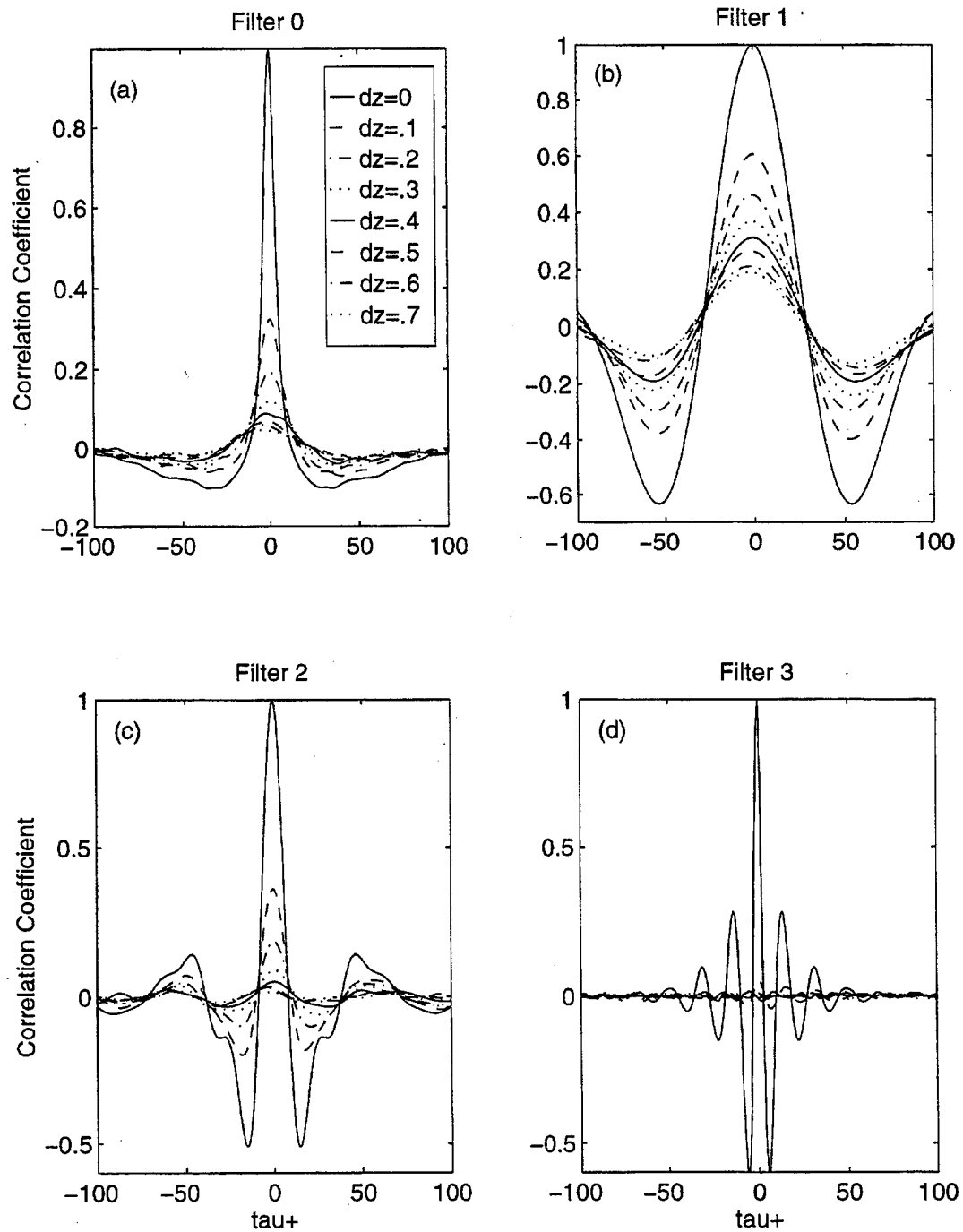
Figure 4.9: The ensemble averaged correlation function between transducer pairs in the spanwise array (a) unfiltered, (b) filter 1, (c) filter 2, (d) filter 3
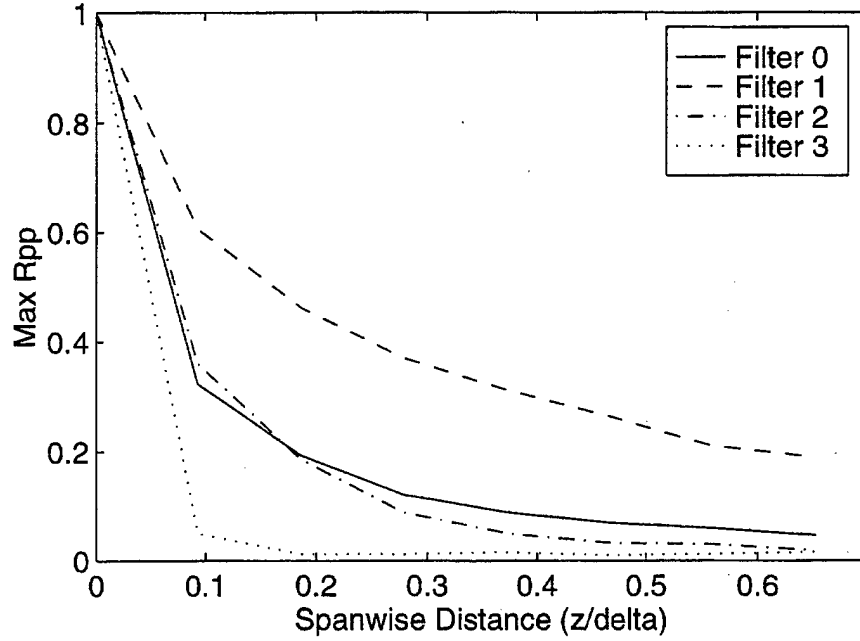
Figure 4.10: Mean decay rate of peak cross-correlation coefficients for spanwise array

high frequency wall pressure activity to be as much as three transducer diameters $(\Delta z/\delta \approx 0.3)$.

The results of **conditional sampling** with the spanwise array are similar to those of the streamwise array. Absent the convective effects, the conditionally averaged event shapes resemble the shapes of the correlation functions in figure 4.9. However, rather than view the event shapes in the time domain, it is possible to project the event shapes onto the X-Z plane using Taylor's hypothesis. By assuming a frozen, convecting pressure field, the conversion from time to space is accomplished via the average measured convection velocity $(U_c/U_0 = 0.67)$:

$$X^+ = U_c^+ * t^+.$$

The wall pressure signals for each transducer in the spanwise array (p1 to p8) were conditionally sampled and ensemble averaged on the detection of peak events (k=+3) at p4, a transducer at the center of the array. Time was converted to
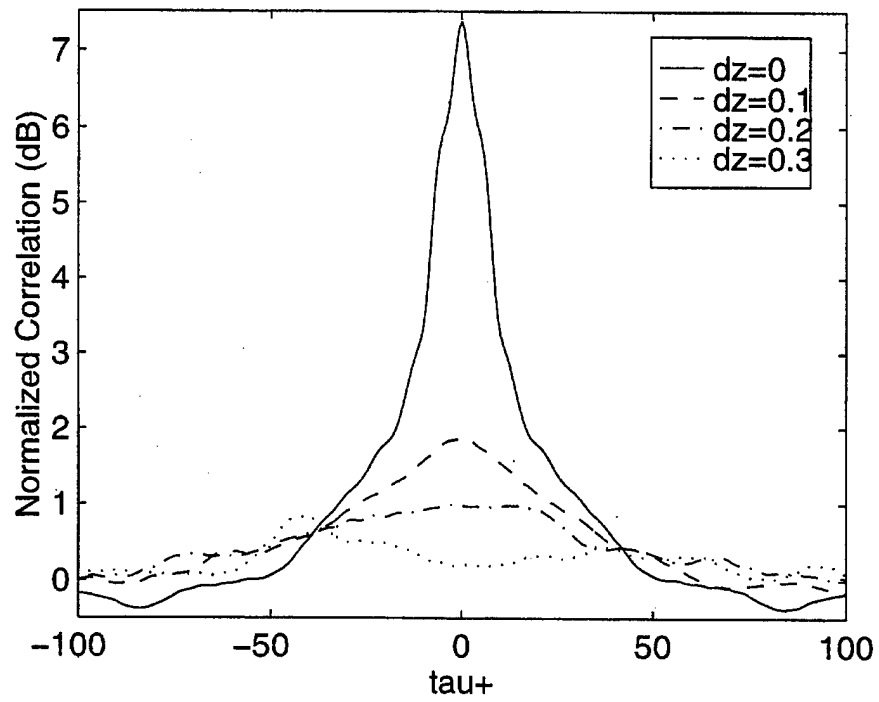
Figure 4.11: Normalized correlation based on the localized variance (VITA) functions of filter 3 wall pressure signals from the spanwise array

space using the average convection velocities, computed for each filter from the streamwise cross-correlation functions. Contour plots from the resulting ensemble averaged event shapes (P/P_{rms}) are shown in figure 4.12. The data from filters 0, 2 and 3 are plotted on the same scale. The streamwise (x^+) scale of the filter 1 curve has been expanded to accommodate the large streamwise extent of the wall pressure events detected in that signal.

Figure 4.12a shows the average spatial extent of high amplitude wall pressure events from the unfiltered (filter 0) signals. When viewed this way, the wall pressure contours do not appear elongated in the streamwise direction like those of Kim [27] for a simulated channel flow. They do, however, exhibit the same nominal spatial extent.

When the wall pressure signal is broken down into its large and small scale components (filters 1, 2, and 3), an interesting picture emerges. Viewing figures 4.12b, c, and d collectively, one sees the complexity of the turbulent wall pressure field. Clearly, the wall pressure signal is composed of many large and small scale events. The wall pressure signatures of these events varies greatly with the filtering performed on the original signal. The wall pressure events associated with scales characteristic of the irrotational flow (filter 1) have a much larger spatial extent than the streamwise or spanwise dimensions of the array. However, the events detected in the filter 3 data are nearly too small to resolve with the transducers used.

4.2   Correlation of Large Scale and Small Scale Structures

In the previous section, the possibility that large scale (filter 2) and small scale (filter 3) wall pressure signatures are correlated was suggested by showing that the events convect at approximately the same speed. Several of the turbulence produc-
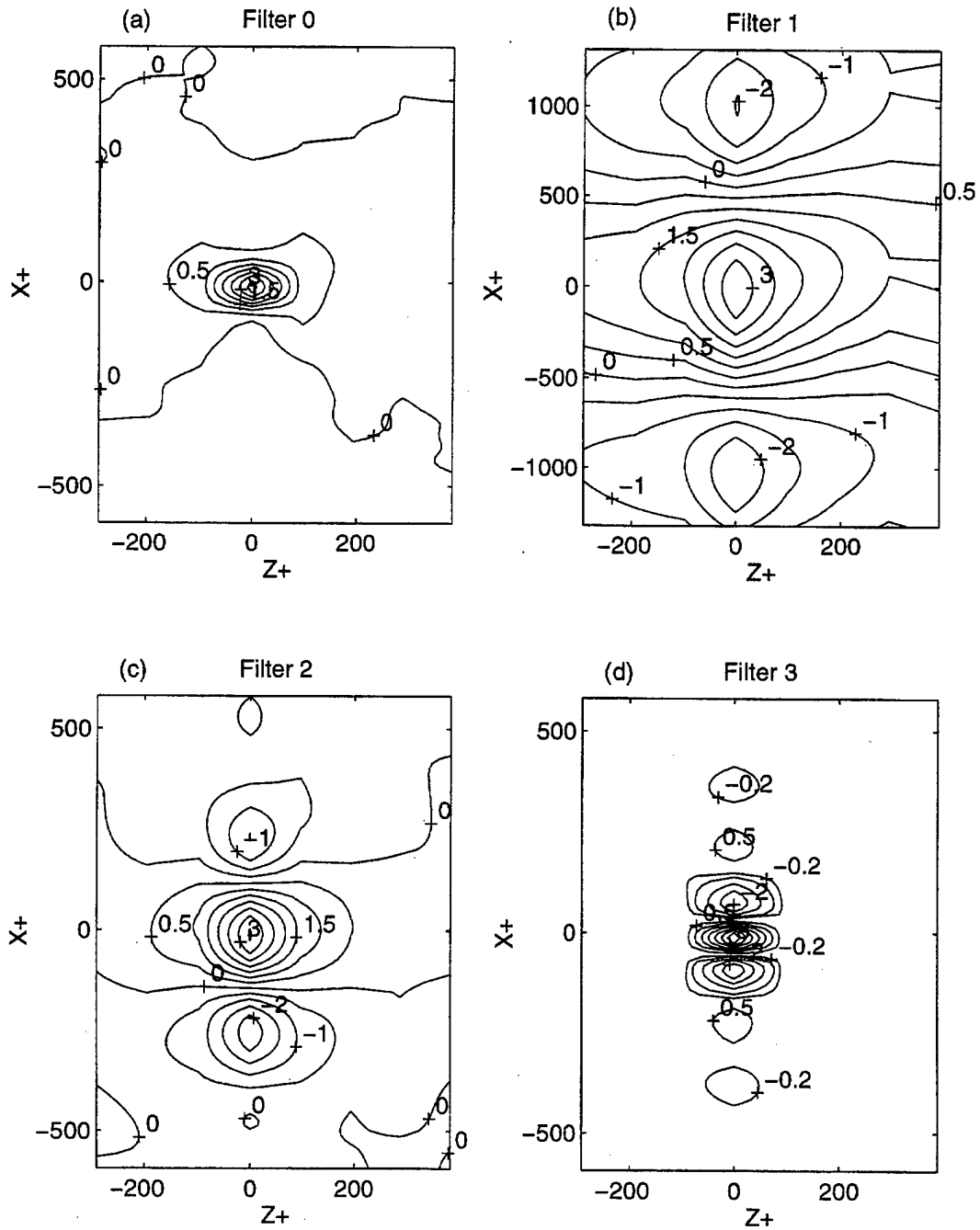
Figure 4.12: Contours of spanwise wall pressure signals conditionally averaged on peak wall pressure Events at P4 (the center of the spanwise array), $X^+ = U_c^+ * t^+$, k=+3, (a) unfiltered, (b) filter 1, (c) filter 2, (d) filter 3

tion models discussed in Chapter 1 are based on this type of correlation in which there is a causal relationship between large and small scale turbulent activity. Thomas and Bull [50], for example, correlated the passage of a large scale, inclined shear layer with small scale, near wall, turbulent production activity.

As described in Chapter 3, the cutoff frequencies of the filters applied to the wall pressure time records were chosen based on the reported turbulent scales. The relationship between the scales in the wall pressure field will be examined in this section using the cross-correlation and conditional sampling analysis tools already demonstrated. These tools will be applied to the wall pressure signals subjected to filters 2 and 3 for both streamwise and spanwise array measurements. In addition, selected time records from the streamwise array are presented to illustrate the relationship between large and small scale events.

4.2.1   Streamwise Analysis

Streamwise correlation measurements presented in the previous section, figure 4.3d and figure 4.5, illustrated an important characteristic of high frequency wall pressure events. They showed that small scale events occur in clusters of large amplitude positive and negative peaks, and that while the pattern of peaks in the cluster changes significantly as it convects, the cluster itself remains generally intact. This was shown by contrasting the standard temporal correlation function of the wall pressure field and the normalized correlation of the wall pressure VITA functions.

Figure 4.13 shows the normalized correlation of the low and high frequency wall pressure VITA functions, that is, filter 2-filter 3 correlations between the transducers. The integration window, T_w^+, was tuned to the time scales isolated by filters 2 and 3, $T_w^+ \approx 52$ and $T_w^+ \approx 12$ respectively.. There appears to be a clear correlation between activity in the filter 2 signal of the upstream-most transducer, and high frequency
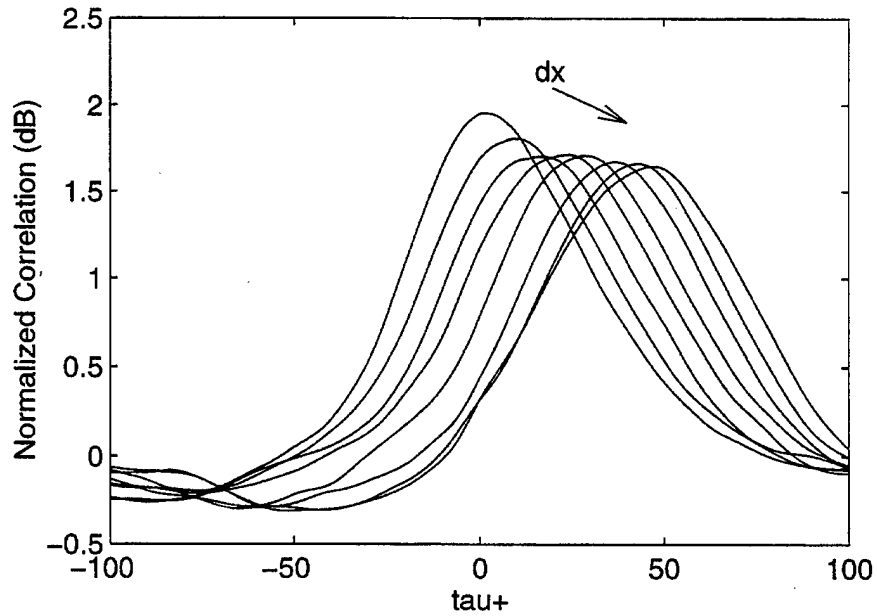
Figure 4.13: Normalized correlation based on the localized variance (VITA) functions of filter 2 wall pressure at P1 and downstream (P1-P8) filter 3 wall pressure

(filter 3) activity at the other downstream transducers in the array. The magnitude of the correlation appears also to decay very gradually with transducer separation. *This qualitative observation of the strong VITA correlations between the filtered signals suggests that the filter 2 and filter 3 wall pressure activity appear to be components of composite footprint of a single, organized turbulent motion.* This behavior is best illustrated by examining the time records of the entire wall pressure array.

A sample window of simultaneous wall pressure time records from the streamwise array is shown in figure 4.14. In this figure, the dotted lines represent filter 2 data while the solid line represents filter 3 data. Each signal is displaced vertically for clarity. In this sample there are obvious regions or clusters of high frequency activity (filter 3) which appear to convect at approximately the same speed as the peaks in the lower frequency signal (filter 2). The time records in this figure are typical of the entire time record collected and were chosen because they effectively

illustrate the correlation results above. At each of the downstream transducers, the turbulent clusters seen in the high frequency signal appear to be slightly preceded by high amplitude positive peaks in the low frequency signal. Thomas and Bull [50] observed the same behavior in high and low pass filtered wall pressure signals. By correlating the high and low frequency components of a single wall pressure signal, they observed that large-amplitude, high frequency pressure fluctuations occur when the low frequency component is falling from a large positive value to a large negative value. This behavior is evident in the time record of figure 4.14.

The strong correlations measured in the filter 2 wall pressure field (figures 4.3c and 4.6c) are illustrated in figure 4.14. The low frequency event shapes appear almost frozen as they convect across the entire span of the array. Schewe [45] made the same observation of unfiltered events in the wall pressure from a four element array. In contrast, the peaks within the high frequency clusters do not retain their shape as the cluster convects.

The VITA function based on signal variance has been shown to be an effective filter for detecting high frequency turbulent wall pressure activity. It has also been successfully applied to the lower frequency (filter 2) wall pressure signal. The low frequency peaks observed in figure 4.14 tend also to occur in small clusters, however, these clusters contain fewer peaks than the high frequency clusters; nominally less than three (positive or negative).

The low and high frequency VITA functions for each transducer in the streamwise array are shown in figure 4.15. The time sample shown is the same as that in figure 4.14. The high frequency events seen in the time records are successfully captured by the VITA function. The low frequency events in the time record also register a bulge in the VITA function. The dominant high frequency event seen in the time record illustrates the temporal relationship between low and high frequency wall pressure
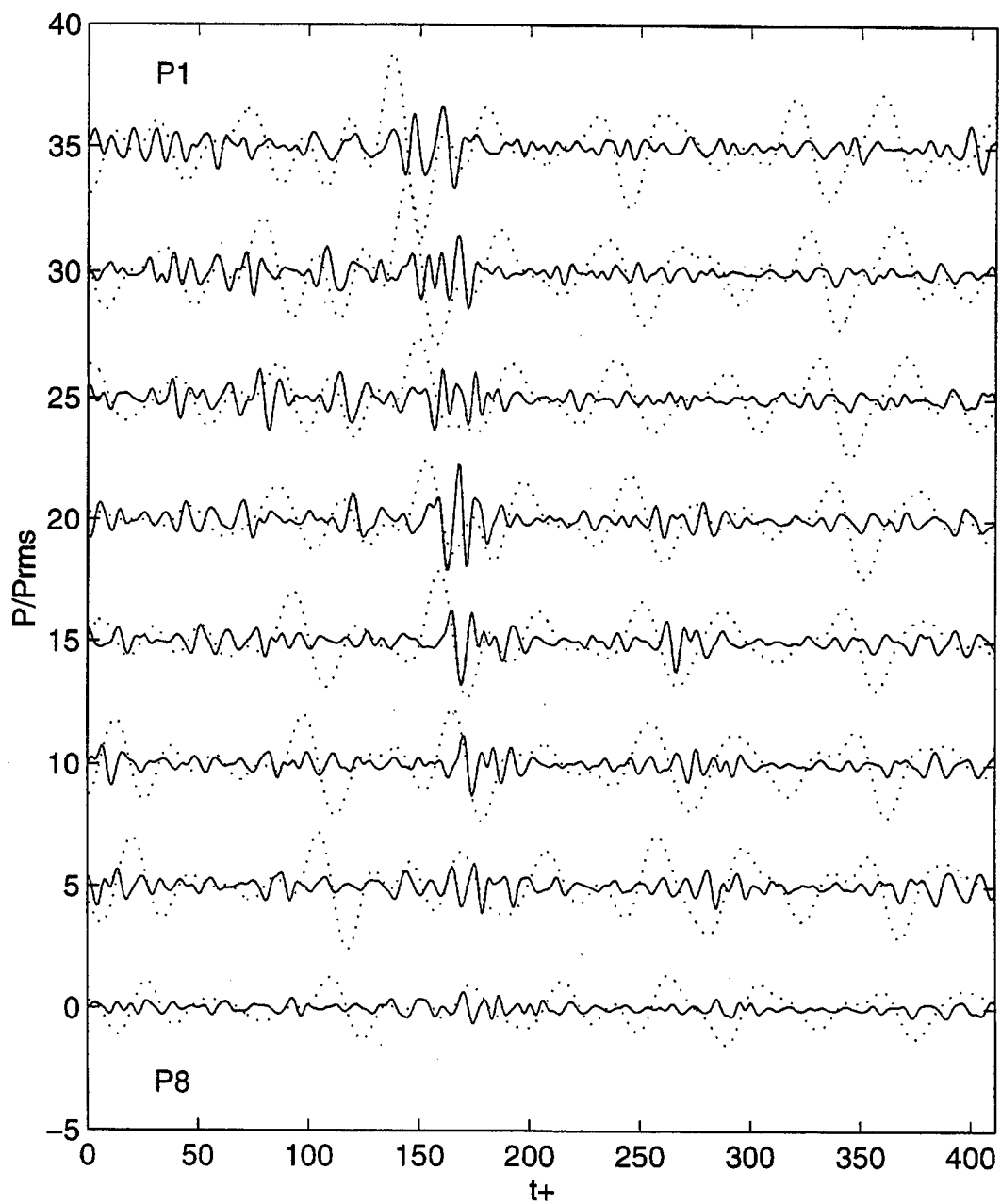
Figure 4.14: Sample filtered Wall pressure time records from the streamwise array (P1 to P8): ..., filter 2; —, filter 3.

activity observed by Thomas and Bull [50]. The high and low frequency VITA functions indicate a time lag between peak low frequency and peak high frequency wall pressure activity. The high frequency VITA functions appear to peak slightly later than the low frequency function. If one assumes that the low and high frequency activity are associated with a single turbulent structure, this result suggests that the large scale component of the structure passes over the transducers ahead of the small scale component. The signature of the large scale head and small scale legs of an inclined hairpin vortex, for example, would satisfy this description.

Although the sample time records in figure 4.14 are typical of the entire time record collected, the observation of a single event is not sufficient to draw general conclusions. Therefore, conditional sampling methods were also applied to the filter 2 and filter 3 wall pressure time records. Figure 4.16 shows the ensemble averaged data from the high frequency (filter 3) wall pressure time records of the first four transducers in the streamwise array based on the detection of low frequency (filter 2) high amplitude (k=+3) peak events in the upstream-most transducer. These data confirm the correlation results in figure 4.13 as well as the temporal information observed in the time records and the VITA functions. There is a clear correlation between low frequency peak events and high frequency wall pressure activity across the array. On average, the peak high frequency activity occurs slightly after the low frequency peak has passed, shown by the offset of the dx=0 curve peak from $t^+=0$.

4.2.2 Spanwise Analysis

By correlating low and high frequency filtered wall pressure signals from the stream-wise array, a relationship between large and small scales in the wall pressure field has been demonstrated. The extent of this correlation was measured by examining the variance (VITA) of the high as well as low frequency wall pressure signals. To
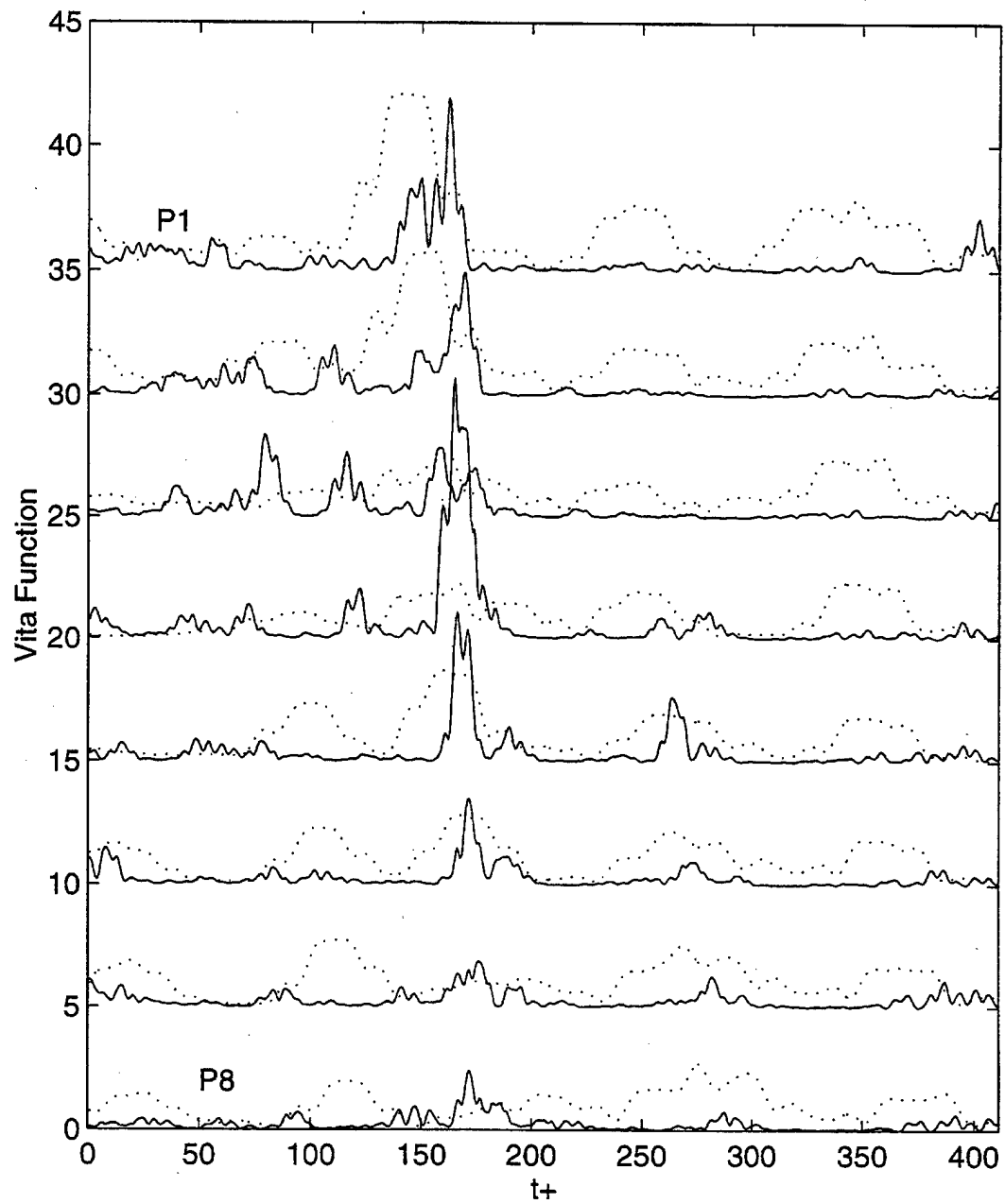
Figure 4.15: Sample VITA functions of the wall pressure time records shown in figure 4.14: ..., filter 2; —, filter 3.
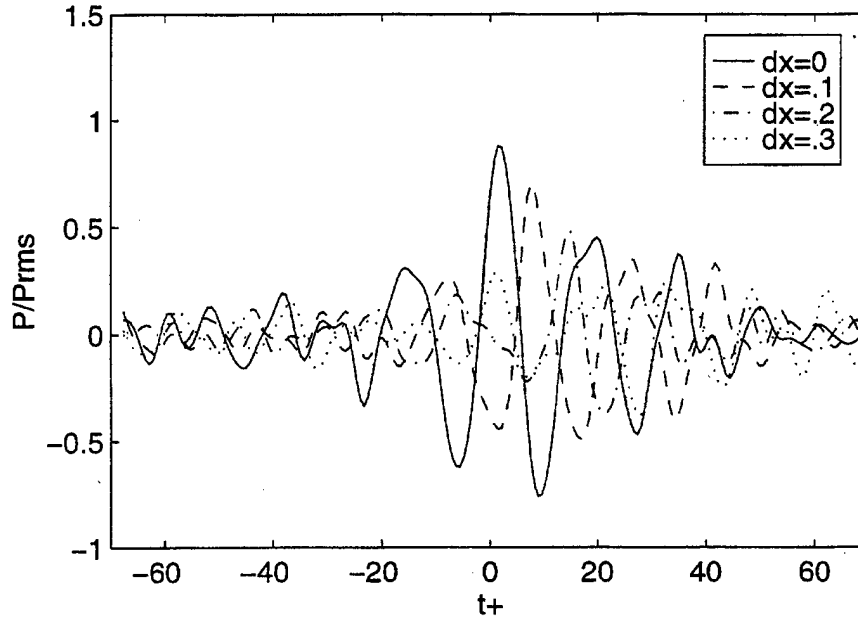
Figure 4.16: Downstream filter 3 wall pressure signals conditionally averaged on peak events in upstream, filter 2 wall pressure signal, (k=+3)

describe the spanwise extent of this correlation, the normalized correlation of the VITA functions of the spanwise low and high frequency wall pressure signals was computed. The results of this analysis are shown in figure 4.17. While the magnitude of the normalized auto-correlation ($\Delta z = 0$) function between the low and high frequency signals is more than 5 dB lower than the correlation of the high frequency signal with itself (see figure 4.11), the spanwise extent of the correlations are nominally the same (2 to 3 transducer diameters).

The correlation data in figure 4.17 appear to be skewed to positive time. This result is consistent with the temporal relationship between the filter 2 and filter 3 wall pressure activity seen in the time records and the VITA functions. The positive skewness indicates that the high frequency (filter 3) activity, to which the filter 2 events are correlated, occurs on average a finite time after the filter 2 activity has occurred, i.e., filter 2 activity precedes filter 3 activity.

Conditional sampling experiments were performed between the low and high
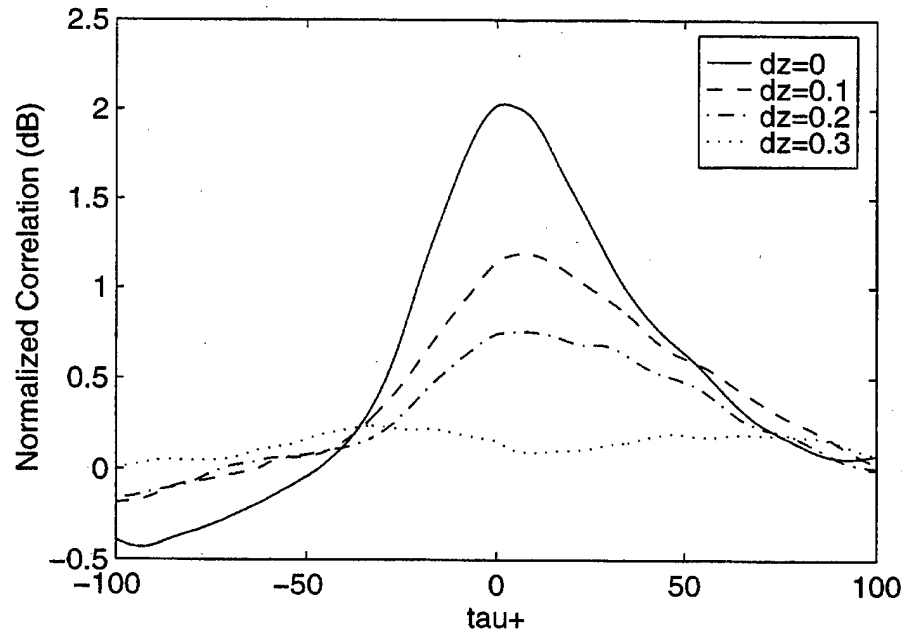
Figure 4.17: Normalized correlation based on the localized variance (VITA) functions of filter 2 wall pressure signals and neighboring filter 3 wall pressure signals from the spanwise array

frequency spanwise array signals. The high frequency signals (filter 3) from all the transducers in the array were conditionally sampled based on large amplitude peak events detected in the low frequency (filter2) signal at P1. The ensemble averaged event shapes from these computations did not show a strong enough correlation between low and high frequency signals to warrant their presentation. The failure of the conditional sampling technique to show a spanwise correlation between low and high frequency wall pressure events is believed to be due to phase jitter. The large streamwise variation from transducer to transducer in the shape of the peaks within the high frequency event clusters shown in figure 4.14 is even more pronounced in the spanwise direction. This variation contaminates the shape of the conditionally averaged time records, and will, in effect, mask any physical correlation between transducer signals.

4.3 Results of Tracking Wall Pressure Signatures

One of the objectives of this investigation is to determine the life cycle of the wall pressure signatures of large and small scale turbulent structures. Ultimately, the signature of these structures could be incorporated as a detector function for an active or adaptive turbulence control system. In the previous section, the correlation between large and small scale structures was demonstrated using only an array of wall pressure transducers. The flow field associated with these large and small scale wall pressure events will be presented in Chapter 5. In this section, an exploratory attempt at tracking these large scale structures exclusively with the streamwise array of wall pressure transducers is presented. A brief description of the evolution of the event tracking algorithm and its logic is then followed by some typical results from the low frequency peak event tracking experiments.

4.3.1 Development of the Event Tracking Algorithm

As discussed earlier, large amplitude wall pressure events in the high frequency (filter 3) time records typically occur as clusters of positive and negative peak events. The pattern of peaks in the cluster was also observed to change significantly as the event convected across the array. For this reason, tracking high frequency wall pressure events using a simple peak tracking algorithm proved to be unfeasible. A more robust cluster tracking scheme would be necessary. Instead, the focus of this part of the investigation was directed to the low frequency (filter 2) wall pressure signals which were shown to correlate with the high frequency wall pressure events.

The large amplitude wall pressure events in the filter 2 time record were shown earlier to usually contain less than three peaks, at least one of which was always a positive peak. An algorithm, described below, was developed to track these events with the array using a peak detection scheme. The development of this algorithm

91

proved also to be a formidable challenge. The logic of the algorithm was continuously improved as more experience was gained with the nature of the events to be tracked. The final product was able to successfully track low frequency events across the length of the array.

One objective of the event tracking experiments was to measure the decay rate of the high amplitude wall pressure events contained in the filter 2 data records. After careful examination of the "clean" as well as the filtered time records from the streamwise array, the term "decay rate" began to loose its original meaning. The following qualitative observations were made:

- Most peak event magnitudes grow and decay as they convect the streamwise extent of the array.

- Typically, when the magnitude of one peak decayed, the magnitude of another peak in the cluster (positive or negative) grew.

- Many peak event magnitudes decay to zero before reaching the last transducer in the array.

- Similarly, many events originated ($P/P_{rms} > k$) within the span of the array.

It should be noted that the same features were also observed and were more pronounced for the high frequency (filter 3) clusters. In the filter 3 event clusters, a peak could come and go in the span of two transducers.

The peak detection and tracking algorithm used in this investigation was written to accommodate the observations listed above. The algorithm will be briefly described. Initial peak detection was triggered at the second and seventh transducers in the array. For each peak detected that exceeded a given threshold pressure (k) a

search was executed upstream and downstream of the reference or "trigger" transducer, P2 or P7. If a peak was detected in the signal of the next transducer within a given time window (positive for P2 detections and negative for P7 detections), its magnitude and location in the time record were registered and the search continued in the next transducer's signal. The length of the time window in which the search for the next peak was conducted was chosen based on the time it would take a peak event to convect the transducer spacing if traveling at one-half the nominal convection velocity measured from the cross-correlation and conditional sampling experiments. Any peaks found beyond this window were assumed to be unrelated to the reference event.

Once all the events at transducers 2 and 7 were detected and their corresponding peaks in the neighboring transducer signals were located, the magnitude and locations of the events were compiled. To determine the "growth" and "decay" rates of the wall pressure peak events, only those peak events which were detected at three or more transducers were saved. Furthermore, only those peak trains whose maximum magnitudes occurred at transducers 2 and 7 were retained. By applying these requirements, the computed mean "growth" and "decay" rates are then based only on peak events which are indeed decaying from or growing to their maximum magnitudes within the span of the array.

4.3.2 Sample Results of Low Frequency Peak Tracking

The resulting peak event magnitude traces for reference transducer 2 (decaying events) and transducer 7 (growing events) are shown in figure 4.18a and b, respectively. The magnitudes are normalized by the magnitude of the peak occurring at the reference transducer. The most noteworthy feature of these curves is the large scatter in the magnitudes of the growing and decaying peak events. A large contrib-

utor to the apparent scatter is the individual peak events which, although have their maximum magnitudes at P2 or P7, decay as well as grow within the span of the array. Another feature which appears to generate considerable scatter is the detection of peaks downstream of P2 or upstream of P7 whose magnitude is actually negative. By defining a positive peak as simply a point n where P_{n-1} and P_{n+1} are less then P_n, it is possible to find positive peaks with negative magnitude. Tightening the requirements for growing or decaying peak events by eliminating such events results in a significant reduction in the number of tracked events and yet was determined to have only a marginal impact on the mean growth or decay rates.

The mean decay and growth rates of tracked low frequency peak events are shown in figure 4.19a and b, respectively. Separate mean growth and decay rates were computed for events which were trackable from 3 to 8 transducers. In figure 4.19a it is not surprising that the average decay rate of the peaks varies inversely with the distance over which the peaks could be tracked. In general, the decay rates depicted in figure 4.19a appear to be exponential. This effect is even more pronounced in the average growth rates shown in figure 4.19b. The average growth rates of the peak events appear to be slightly steeper than the average decay rate and follow a nominally exponential shape.

The fourth and final measure of convection velocity used in this investigation is the time between peaks detected by the peak tracking algorithm. The data shown in figure 4.20a and b are the actual time between the peaks detected and traced in figure 4.18a and b. The average time between peaks for the decaying and growing events is approximately 0.26 msec. This translates to $U_c/U_0 \approx 0.64$, which is consistent with the spectral, correlation, and conditional averaging results presented in section 4.1.

The distribution of peak detection times in figure 4.20 illustrates the point discussed earlier about the effect of convection velocities of individual events on the
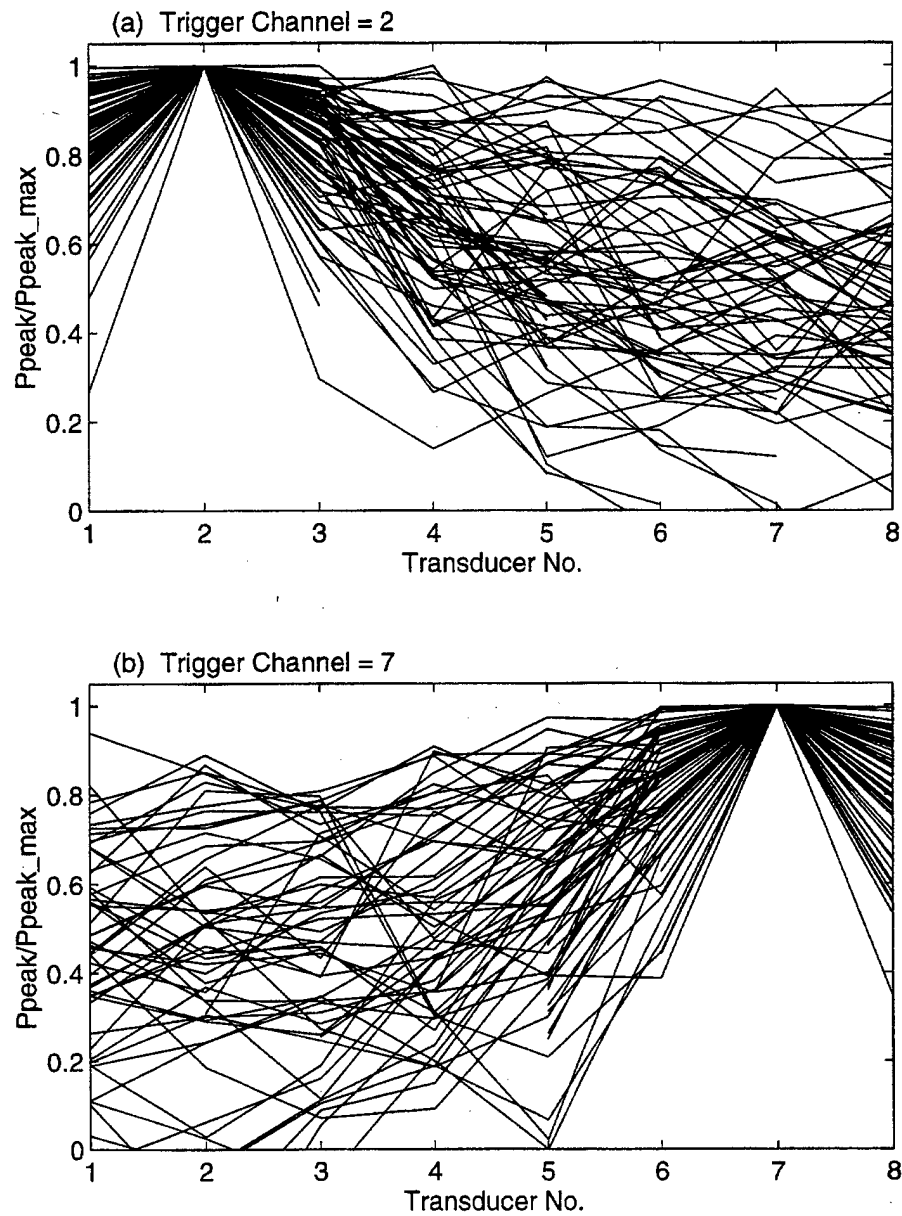
Figure 4.18: Relative magnitude of filter 2 positive peak events tracked using the streamwise array (a) maximum peak value occurs at P2, (b) maximum peak value occurs at P7
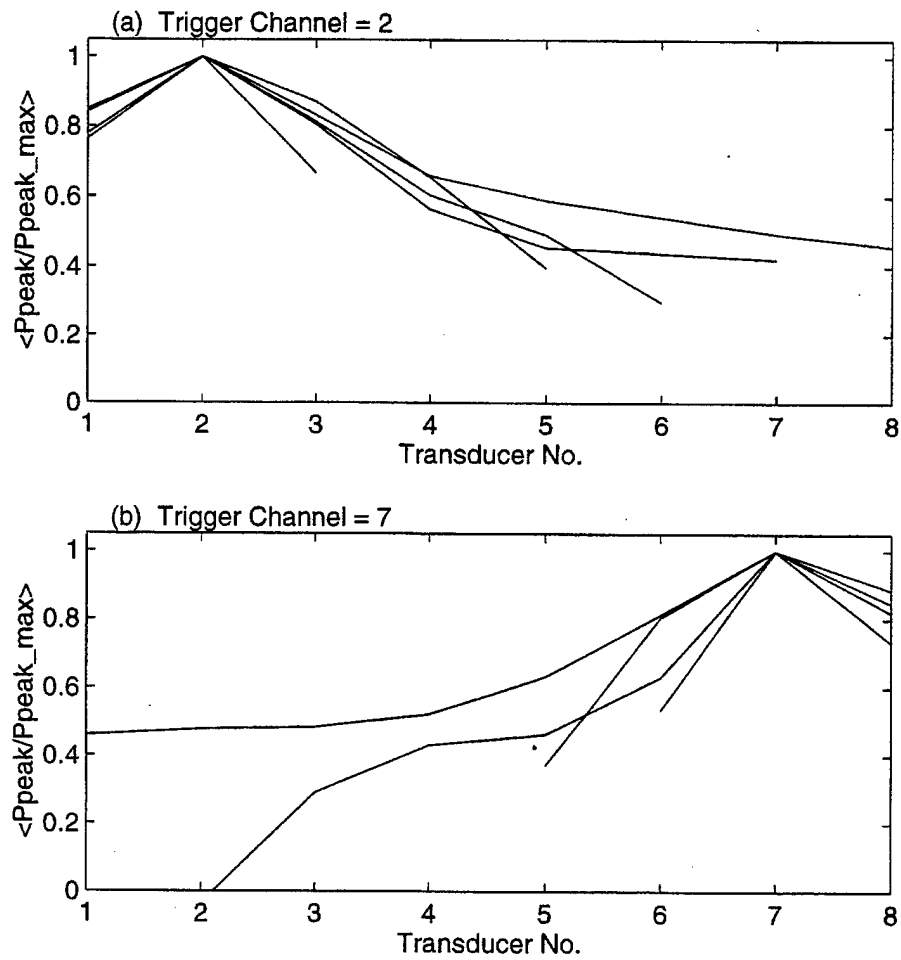
Figure 4.19: Mean growth and decay rates of filter 2 peak event magnitudes tracked with the streamwise array (a) maximum peak value occurs at P2, (b) maximum peak value occurs at P7
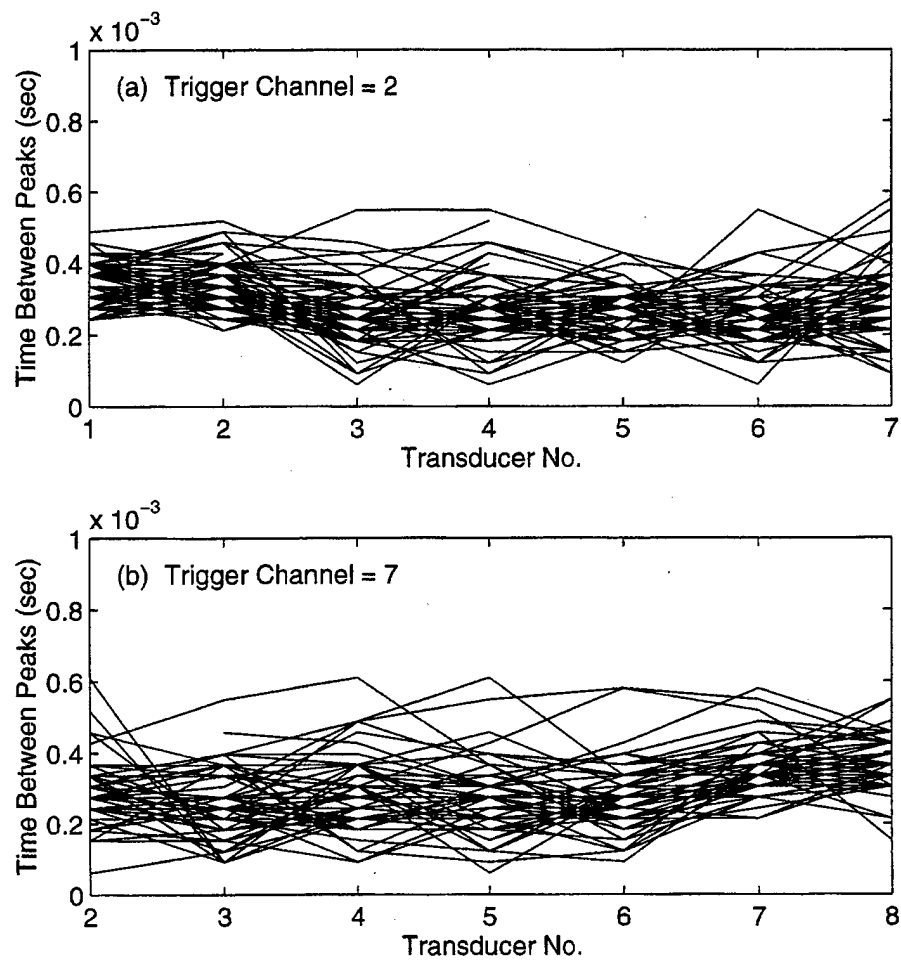
Figure 4.20: Convection velocity (time between peaks) obtained from individually tracked filter 2 peak events: (a) maximum peak value occurs at P2, (b) maximum peak value occurs at P7

magnitude of conditional averaging results. It is for precisely this reason that the decay rates of wall pressure events were not measured from conditional sampling results. The phase jitter introduced into the ensemble averaged event shapes by peaks which convect at different speeds is significant, as shown convincingly by figure 4.20. This observation also confirms the spectral findings on the range of wall locations (y^+) at which the pressure source terms are centered.

4.4 Summary of Findings

The space-time characteristics of the wall pressure field have been measured with the streamwise and spanwise transducer arrays using various signal processing tools. By filtering the wall pressure in selected frequency bands (filters 1, 2, and 3), structural features of the wall pressure field have been revealed. The spatial extent and convective features of the wall pressure field as measured by cross-spectral, cross-correlation, and condition sampling methods were demonstrated to be highly dependent on the filtering of the wall pressure signals and hence potentially subjective. In addition, by comparing signals subject to different filters, a correlation between large scale (filter 2) and small scale (filter 3) wall pressure activity was shown. Finally, a wall pressure peak event tracking algorithm was demonstrated which utilized the signals from the streamwise transducer array. A general summary of the important findings from each of these efforts will now be discussed.

The spatial extent of the wall pressure field was determined from cross-spectral and cross-correlation measurements from both the streamwise and spanwise arrays. The spectral and correlation results were consistent in that the streamwise extent was significantly larger than the spanwise extent. In addition, the magnitude of these correlations decayed exponential with transducer spacing. Not surprisingly, the wall pressure field when filtered to retain only irrotational motions (filter 1) had a much

larger spatial extent than either the high frequency or unfiltered wall pressure field. Furthermore, by correlating wall pressure signals based on the cluster groupings of events (VITA functions), the spatial extent of both the large scale (filter 2) and small scale (filter 3) wall pressure field expanded significantly.

Results from conditional sampling experiments were consistent with both the cross-spectral and cross-correlation findings. By conditional sampling and ensemble averaging large amplitude peak wall pressure events, another measure of the spatial extent of wall pressure events was obtained. The temporal and spatial characteristics of the ensemble averaged event shapes showed the same dependency as the correlation functions on the band pass filter used.

By measuring the convection velocity of the filtered wall pressure field, some important features were observed. It was shown that the pressure sources associated filter 2 and filter 3 scales convected at nominally the same speed as that measured in the 'clean', filter 0 wall pressure. In contrast, the pressure field associated with the very low frequency (filter 1), irrotational motions convects at a consistently higher speed. This was the first confirmation that the filters chosen discriminated between turbulent scales as well as regions of the boundary layer. The common convection velocity of the filter 2 and filter 3 scales was also the first indication that these scales may be components of a composite turbulent structure.

The issue of a correlation between large and small scales was addressed directly in the subsequent section where normalized correlation and conditional sampling techniques were applied to wall pressure signals subjected to filters 2 and 3. Streamwise and spanwise normalized correlation analyses between a single, low frequency (filter 2) wall pressure signal and high frequency (filter 3) signals from the other transducers in the array showed a strong correlation between the scales. Similarly, conditional sampling results from the same data set showed that, on average, high

frequency wall pressure activity across the streamwise array was associated with the passage of low frequency activity. Visual analysis of filtered time records from the streamwise array confirmed this behavior. The ability of the VITA technique to capture both the filter 2 and filter 3 wall pressure activity was also demonstrated.

Collectively, the findings revealed a consistent phase relationship between large and small scale wall pressure activity. This phase relationship supported the idea that, in many cases, small and large scale wall pressure activity were components of the wall pressure signature of a single, large scale, turbulent structure. The pattern of the large scale activity was observed to be different from that of the small scale activity or events. The small scale activities were characterized by intermittent, convecting clusters of peaks which evolved over the spatial extent of the array. The large scale activity, which accompanied the small scale events, resembled a frozen, convecting wave train, which maintained its shape as it traversed the length of the streamwise array. These large scale wave trains were less intermittent than the high frequency events and usually contained 2 or more peaks and axis crossings. This feature made them well suited to VITA detection.

A wall pressure event tracking algorithm was developed to track the individual peaks in the large scale wave trains (events). Spatial and convective features obtained from these analyses were consistent with the findings of the correlation and conditional sampling analyses. In addition, the tracking analysis revealed more subtle features of the large scale wall pressure activity. One such feature was the large variation in convection velocity between individually tracked events. This observation confirmed the spectral findings on the range of wall locations (y^+) at which the pressure source terms are centered. More importantly, this finding illustrated the need for caution when interpreting conditional sampling results where multiple events, such as those tracked with the streamwise array, have been ensemble

averaged.

The results presented in this chapter lay the groundwork for the flow field measurements to be presented in Chapter 5 in which many of the same cross-correlation and conditional sampling schemes are applied to simultaneously obtained velocity and wall pressure data. The next logical step would be to examine the flow field data in an attempt to identify the small and large scale active structures, as well as to determine if the relationship exists between distinct active flow structures across the boundary layer. This will be the focus of the next chapter.

Chapter 5

RESULTS ON IDENTIFICATION OF ORGANIZED FLOW STRUCTURES

This chapter will focus on the simultaneous measurements of the flow field and wall pressure in which both are subjected to the filtering schemes previously discussed. The frequency bands of the four filtering schemes used throughout this investigation are re-stated in table 5.1. The goal is to capture or identify the distinct flow structures whose wall pressure signatures were measured with the array. These flow structures will be defined using the same analysis tools previously employed which include cross-spectral, cross-correlation, and conditional sampling, but applied now to both velocity and pressure data.

The streamwise and spanwise spatial extent of the pressure-producing structures will be defined by measuring both the coherence and cross-correlation between wall

Table 5.1: Band-pass filters employed in this investigation

Label	Bandwidth (Hz)	Flow Structures
Filter 0	$100 \leq f \leq 5000$	Composite Flow
Filter 1	$100 \leq f \leq 300$	Outer / Irrotational
Filter 2	$300 \leq f \leq 1200$	Large Scale Active
Filter 3	$1200 \leq f \leq 5000$	Small Scale Active

pressure and streamwise (u), as well as wall normal (v) components of velocity at locations across the boundary layer. The temporal cross-correlation functions between pressure and velocity will also provide unique insight into the temporal and convective behavior of the pressure producing structures. These findings will be presented in Section 5.1.

This chapter also presents the results of conditional sampling experiments in which u and v are sampled based on the occurence of large amplitude wall pressure events measured by the streamwise array. From these results, a composite picture of the average pressure producing flow structures can be inferred. In addition, by conditionally sampling high frequency velocity signals on low frequency wall pressure events, the correlation between large and small scale structures is illustrated in the ensemble averaged flow field. Section 5.2 will present these investigations. Finally, a summary of the overall results from the flow field measurements are presented in section 5.3.

5.1 Spectral and Temporal Wall Pressure -Velocity Correlation

Although the cross-spectrum and cross-correlation functions are Fourier transform pairs, it is useful to examine both functions when studying turbulent structures. The cross-spectrum contains both the coherence and phase relationship and is a measure of the mean linear correlation between two signals as a function of frequency. It is important to note that the normalized cross-spectrum (the coherence function) provides a measure of the linear dependence between two signals and the cross-correlation provides a measure of the correlation between the two. While similar, the measures of dependency and correlation are subtly different in that coherence is not influenced by the phase relationship between the two signals. The correlation,

on the other hand, is a function of phase difference. For example, two completely dependent signals, such as $sin(\omega t)$ and $sin(\omega t + \pi/2)$ have zero correlation. The phase information is useful when analyzing pressure-velocity correlations because it gives the relationship between wall pressure and the direction of the velocity field. For these reasons, the coherence functions and the cross-correlation functions will be examined collectively. Results of correlations between the velocity field and the streamwise wall pressure array will be presented first, followed by results from the spanwise array.

5.1.1 Streamwise Analysis

As described in Section 2.4, flow field measurements were performed downstream of the streamwise transducer array. These measurements consisted of three boundary layer surveys in which u and v were measured at 30 (y^+) locations across the boundary layer. The surveys were conducted at evenly spaced x locations ($\Delta x = d_{transducer}$) resulting in an 18x30 grid of pressure-velocity correlation measurement stations. The experimental configuration is illustrated in figure 5.1. The data to be presented will effectively represent the cross-spectral and cross-correlation measurements between a fixed wall pressure transducer at location $(x^+, y^+)=(0,0)$ and hot-wires located at each station in the streamwise grid. Therefore, the flow field depicted by the correlation contours will represent flow patterns downstream of the transducer array.

Cross-Spectral Analysis

At each pressure-velocity measurement station in the 18x30 streamwise grid, the cross-spectral density functions, $\Phi_{pu}(\omega)$ and $\Phi_{pv}(\omega)$, were computed between wall pressure and velocity. These functions were computed from unfiltered, simultaneously obtained pressure and velocity time records. The cross-spectrum/coherence computations were performed with MATLAB using spectral density and coherence
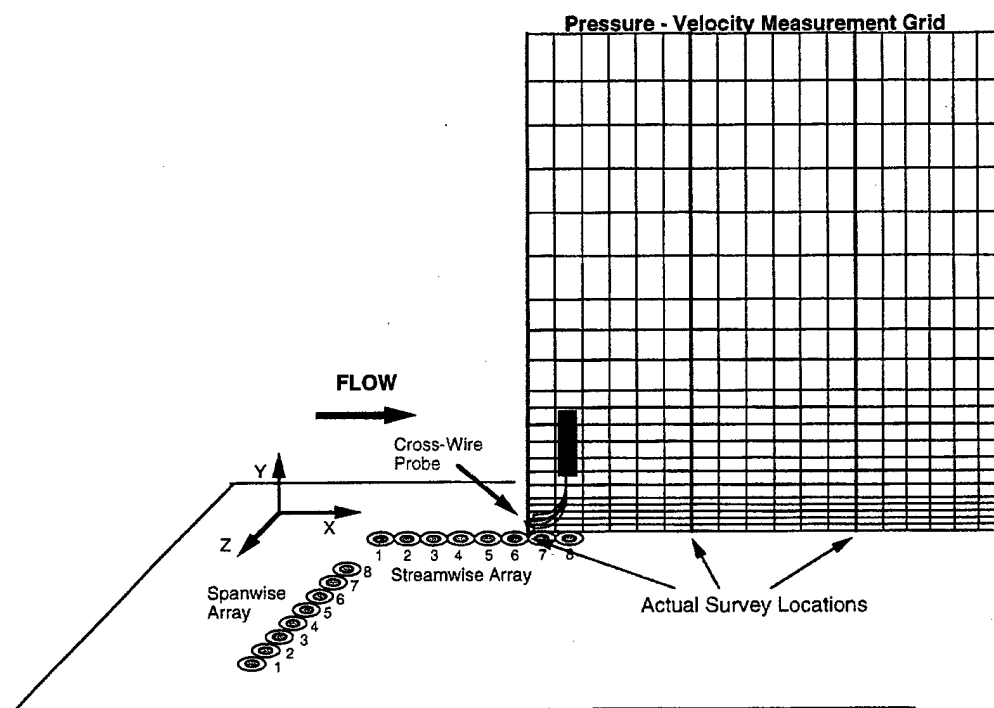
Figure 5.1: Experimental configuration for streamwise flow field measurements

subroutines from the Signal Processing Toolbox (1024 point, Hanning window) [32]. To illustrate the behavior of the pressure-velocity coherence levels as a function of location in the flow field, contours of the mean coherence levels, averaged within the frequency bands of filters 1, 2, and 3, were generated. By viewing the pressure-velocity coherence in this manner, a spatial map of the mean pressure producing structures can be obtained for the scales associated with each filter.

Contours of pressure-velocity coherence, Γ_{pu} and Γ_{pv} in the streamwise measurement grid for filters 1, 2, and 3 are shown in figures 5.2 - 5.4, respectively. Contours of the mean coherence level for the **filter 1 band** are given in figures 5.2a and 5.2b for u and v, respectively. Two distinct regions of strong coherence between wall pressure and streamwise velocity are evident in figure 5.2a. One region is located in the near wall region of the boundary layer and another is observed outside the wall layer ($y^+ > 1026$). The near wall coherence region starts from its maximum at ($x^+=0,y^+=0$) and forms an inclined ridge that decreases with wall distance but with consistently strong levels near the wall ($y^+ \leq 100$). This indicates that low frequency pressure fluctuations at $x^+=0$ are associated with strong near wall streamwise velocity fluctuations. Γ_{pu} breaks down between $600\leq y^+ \leq 1200$ which is essentially the upper half of the turbulent boundary layer, a region noted for its turbulent/non-turbulent intermittency. Another coherence region rests outside the boundary layer at $y+ \geq 1000$. Here, the low free stream turbulence levels lead to strong low frequency pu coherence resulting from the large scale induced irrotational motions.

The pu coherence contours for this low frequency range are consistent with those of Snarski and Leuptow [46] who contoured Γ_{pu} at $\omega\delta^*/U_0 = 0.23$, which is in the frequency range of filter 1. Snarski and Leuptow, who lacked wall normal velocity (v) data, attributed the near wall and outer-irrotational levels to a single, very

Figure 5.2: Filter 1 pressure-velocity coherence contours in the streamwise measurement grid

large scale, rotating structure. Closer examination of the data in figure 5.2 suggests otherwise. The breakdown of Γ_{pu} between $600 \le y^+ \le 1200$ was observed by other investigators [46, 53]. And while the intermittency of the velocity signals in this region may degrade the mean coherence levels, the consistent streamwise extent of this coherence "gap" suggests the existence of two distinct structures rather than a large single rotating structure. The near wall and irrotational structures appear to have little statistical correlation other than similar wall pressure signatures. Other data to be presented in this chapter on the coherence as well as correlation contours will support this argument.

The low frequency coherence contours between pressure and wall normal velocity, Γ_{pv}, shown in figure 5.2b also display two regions of strong coherence located within and outside the boundary layer. However, in contrast to the u component, which peak near the wall the v component peak within the boundary layer occurs at $y^+ \approx$ 700. The peak Γ_{pv} outside the boundary layer occurs at nominally the same location as the Γ_{pu} peak. The larger overall levels in the pv coherence contours are probably indicative of the stronger direct correlation between wall pressure and wall normal velocity fluctuations. Overall, these data illustrate the spatial extent of the observed irrotational structures to be in excess of three boundary layer thicknesses in the vertical direction and significantly more in the streamwise direction.

Mean coherence contours for the **filter 2 band** are shown in figure 5.3. The pu coherence data in figure 5.3a are similar in shape to the filter 1 contour within the boundary layer, however, the spatial extent of the structures is much smaller. There appears to be little coherence between wall pressure and structures of this scale in the outer irrotational flow as observed in the filter 1 band. This is true for both pu and pv coherence. The dominance of the pv coherence in the internal layer is more obvious in these data than in the filter 1 contours. The flattening of the contours in
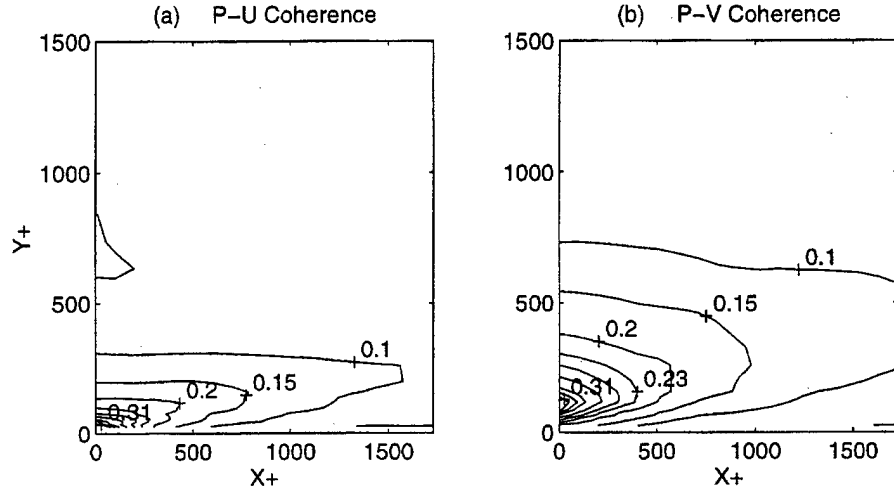
Figure 5.3: Filter 2 pressure-velocity coherence contours in the streamwise measurement grid

the y-direction indicates that the coherent motions are inclined and convecting with the mean flow.

The location of the inner layer peaks in the filter 2 coherence contours are consistent with the filter 1 contours for the structures observed within the boundary layer. The pu coherence peaks at the "origin" ($x^+=0,y^+=y_{min}$) while the pv coherence peaks at $y^+ \approx 125$. Wall pressure fluctuations at $x^+=0$ are associated with both near wall fluctuations in u and fluctuations in v at a finite y distance. Near wall ejections measured by numerous investigators exhibit this type of u behavior. In fact, recent investigations [52] use streamwise shear stress as a detection criteria for capturing small scale, turbulent production events.

Small scale (filter 3) activities were shown in Chapter 4 to have a significantly smaller spatial extent than the large scale filter 2 or filter 1 activities. The pu and pv coherence contours for the **filter 3 band** displayed in figure 5.4a and 5.4b are consistent with those findings. Although the resolution of the measurement grid is nearly too large to resolve these scales, the same general patterns within the boundary layer shown in the filter 1 and filter 2 coherence contours are reproduced in
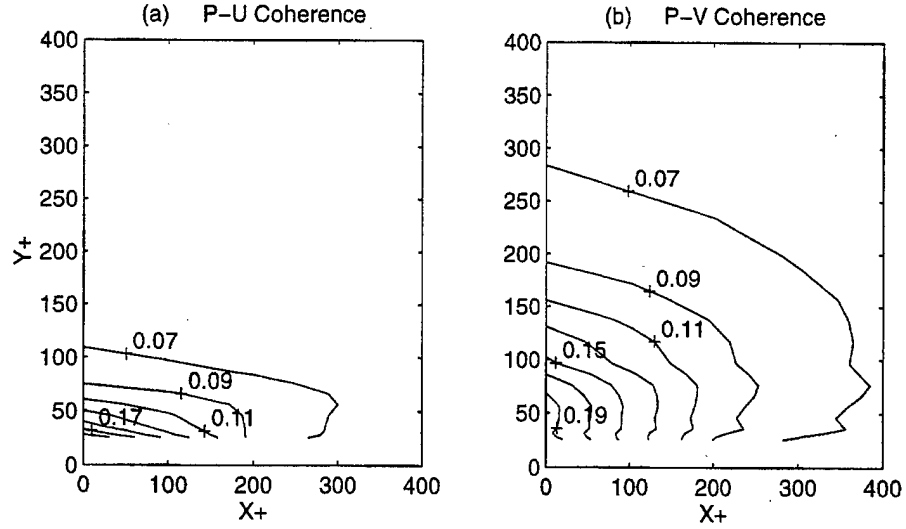
Figure 5.4: Filter 3 pressure-velocity coherence contours in the streamwise measurement grid

the high frequency data. The dominance of pv as well as the convection/inclination effects are clearly demonstrated, although, the flatness of the contours, and hence the mean inclination angle of the structures is less than that of the larger scales. In addition, the orientation of the pu and pv contour peaks are consistent with the larger scales showing a correlation between wall pressure fluctuations and near wall streamwise velocity fluctuations. The peak in Γ_{pv} appears to be approximately $y^+ \approx 50$.

Cross-Correlation Results

The cross-correlation function between wall pressure and velocity has been used by many investigators to study the turbulent sources of wall pressure fluctuations [24, 30, 39, 46, 55]. This function complements the cross-spectral analysis since it incorporates the coherence and phase information at all frequencies when applied to unfiltered time records. The ensemble averaged cross-correlation functions between wall pressure and velocity, $R_{pu}(\tau)$ and $R_{pv}(\tau)$, were computed at each pressure-velocity station in the streamwise measurement grid. X-Y contours of the value of
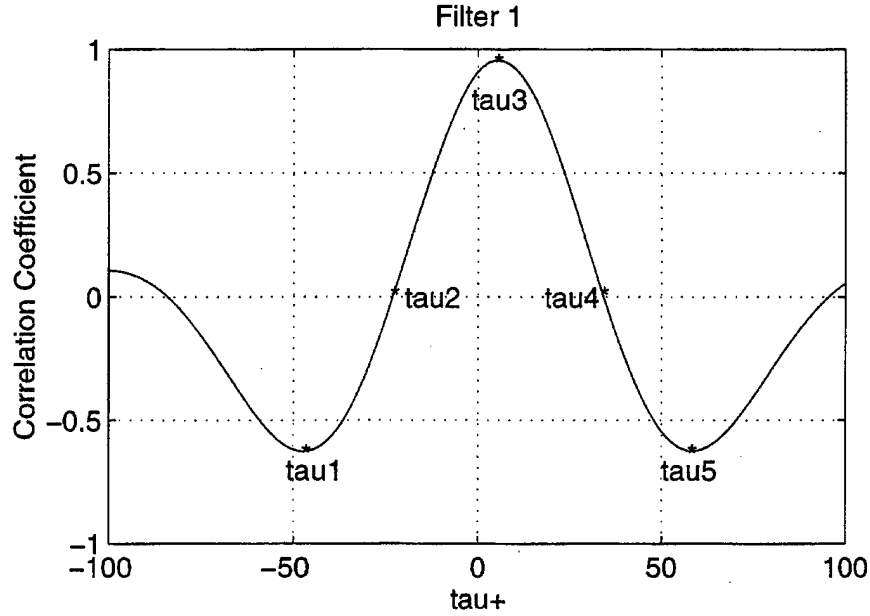
Figure 5.5: Sample time delays at which correlation contours are computed

these functions at five separate time delays were assembled into consecutive plots to illustrate the time history of these functions throughout the flow field. Since the contours are constructed at single time delays, they represent a "snapshot" of the average eddy structure throughout the boundary layer that contributes to the fluctuating wall pressure [46].

The time delays at which the correlation contours were computed were based on the location of the peaks and axis crossings in the wall pressure cross-correlation functions (see Chapter 4). Therefore, the values of these time delays are different for each filter. Figure 5.5 illustrates how the points $(\tau_1$ to $\tau_5)$ were chosen from the cross-correlation function, $R_{pp}(\tau)$, for an adjacent streamwise transducer pair. The reference point of maximum correlation was shifted to $\tau = 0$ and the other times were equidistant from the center. This method of flow visualization was recently applied to a step flow by Hijikata, et al,[19] who successfully illustrated the separation and reattachment of the boundary layer.

The contours of $R_{pu}(\tau)$ and $R_{pv}(\tau)$ evaluated at τ_1 through τ_5 are shown in figures 5.6 through 5.9 for the time records using filters 0,1,2 and 3 respectively. The solid line denotes positive correlation while the dashed line denotes negative correlation. By comparing the results from these filtered time records, a wealth of information about the time averaged pressure producing structures is obtained.

The correlation contours of R_{pu} and R_{pv} for the **filter 0 (unfiltered) time records** are shown in figure 5.6. The R_{pu} results at $\tau=0$ are consistent with the results of Snarski and Leuptow [46] for measurements on a cylindrical boundary layer. The appearance of these data has been slightly enhanced using a running average, smoothing algorithm. As with the low frequency (filter 1) coherence contours, the unfiltered correlation functions show both the large irrotational structures and the inclined 'δ -scale' structures within the boundary layer. These two scales appear to dominate the unfiltered correlation results.

The behavior of R_{pu} and R_{pv} in the intermittent region of the boundary layer is also consistent with the coherence functions, i.e., R_{pu} goes to zero while R_{pv} remains strong. This behavior also seen by Kobashi & Ichijo [30], is believed to be indicative of the strong relationship between fluctuating v and wall pressure. Drawing a line from (0,0) through the center of the $R_{pu}(\tau = 0)$ contours it can be shown that the irrotational structures are inclined at approximately 45-degrees while the δ-scale structures in the boundary layer are inclined at approximately 20-degrees from the wall. 20-degree inclination angles have been observed by Snarski & Leuptow [46] as well as others [29, 50] and have been attributed to near-wall shear layers and large scale "backs" (see section 1.2.1). The 45-degree inclination of the irrotational motions has also been observed by investigators using other analysis techniques.

Understanding the phase information in the correlation contours is critical to interpreting these figures. In figure 5.6a, for example, regions of negative R_{pu} indicate
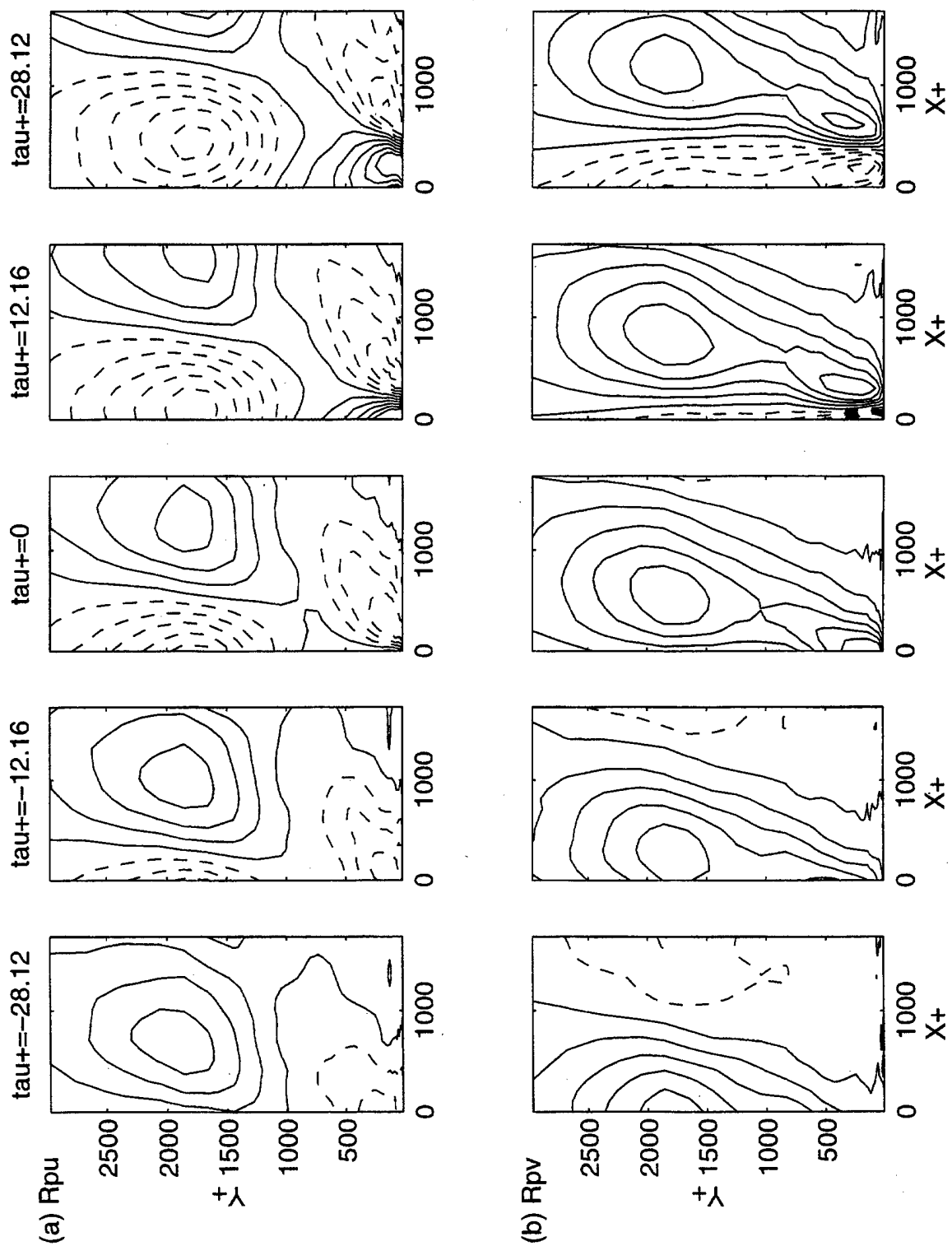
Figure 5.6: Streamwise filter 0 pressure-velocity correlation contours at selected time delays

a correlation between positive pressure at $x^+ = 0$ and negative streamwise velocity and vice versa for negative pressures. By examining both R_{pu} and R_{pv} at $\tau = 0$, one may infer a δ-scale structure comprised of a large negative u and positive v, i.e., a Q2 or ejection type event to be associated with positive wall pressure. And in the downstream wake of this structure ($\tau^+ = 28.12$), one sees a δ-scale sweep or Q4 type event. It can also be seen in figure 5.6 that R_{pu} and R_{pv} for the δ-scale motion are nominally 180-degrees out of phase, which is consistent with Reynolds stress activity. R_{pu} and R_{pv} for the irrotational motions are nominally 90-degrees out of phase, characteristic of two-dimensional flow over a wavy wall, a model for irrotational flow verified by Panton [39] who observed the same pressure velocity phase relationships. These phase relationships suggest that while the δ-scale motions and the irrotational motions may coexist in the same flow field, their statistical correlation is weak and they are most likely seen together in the correlation contours because of their common wall pressure signatures. This finding supports the original conjecture derived from the coherence contours.

When the pressure and velocity signals are decomposed into large and small scales using filters 1, 2, and 3, the resulting correlation functions contain features not visible in the unfiltered (filter 0) data. Figure 5.7 shows the R_{pu} and R_{pv} contours for **filter 1 time records**. The most noteworthy feature of these curves is the similarity to the unfiltered data in figure 5.6. For example, the pressure-velocity phase relationship of the irrotational and δ-scale motions observed in figure 5.6 for the unfiltered data are reproduced in figure 5.7 for the filter 1 data, as are the inclination angles of the two structures. This suggests that the turbulent scales isolated by filter 1 dominate the unfiltered pressure-velocity correlation results and may mask the near wall, small scale production activity. Therefore, previous investigators who have studied turbulent boundary layer structures and wall pressure sources using

pressure-velocity correlation techniques may in fact only be seeing the very large scale irrotational motions (in unbounded flows) and the δ-scale motions within the boundary layer.

By removing the irrotational motions from the turbulent signals, the near-wall structures are more clearly revealed. Figure 5.8 shows R_{pu} and R_{pv} contours for the **filter 2 time records**. These contours reveal convecting coherent motions that have vertical scales of approximately 0.8δ (defined by the R_{pv} extent) and a streamwise extent larger than the length of the measurement grid. Also, consistent with the filter 2 coherence contours, there is little correlation between motions of this scale in the irrotational flow and wall pressure. In addition, the vertical extent of the pv correlations are more than twice that of the pu correlations.

The streamwise inclination of the correlation contours seen in the near wall region for the unfiltered as well as filter 1 data is also evident in the smaller scale filter 2 structures. However, some important distinctions should be noted. The filter 2 structures, shown by the $\tau=0$ negative contour, are less inclined than the filter 1 scales. Furthermore, the inclination of the filter 2 scale structures appears to increase slightly as they convect. This trend is observed in both the R_{pu} and R_{pv} contours. The 180-degree phase relationship between R_{pu} and R_{pv} is again indicative of Reynolds stress activity. The alignment of the positive and negative pu and pv contours indicates the same lift-up or ejection motions associated with positive pressure at $x^+=0$. In general, these data show that the mean pressure producing turbulent structures of this scale are nominally 0.5δ to 0.8δ in vertical extent, contain at least two vortical components (4 contours) and become more inclined as they convect. They tend also to remain well correlated as they convect the length of the measurement grid ($\sim 1.5\delta$).

Finally, the correlation contours for **filter 3 time records** are shown in figure
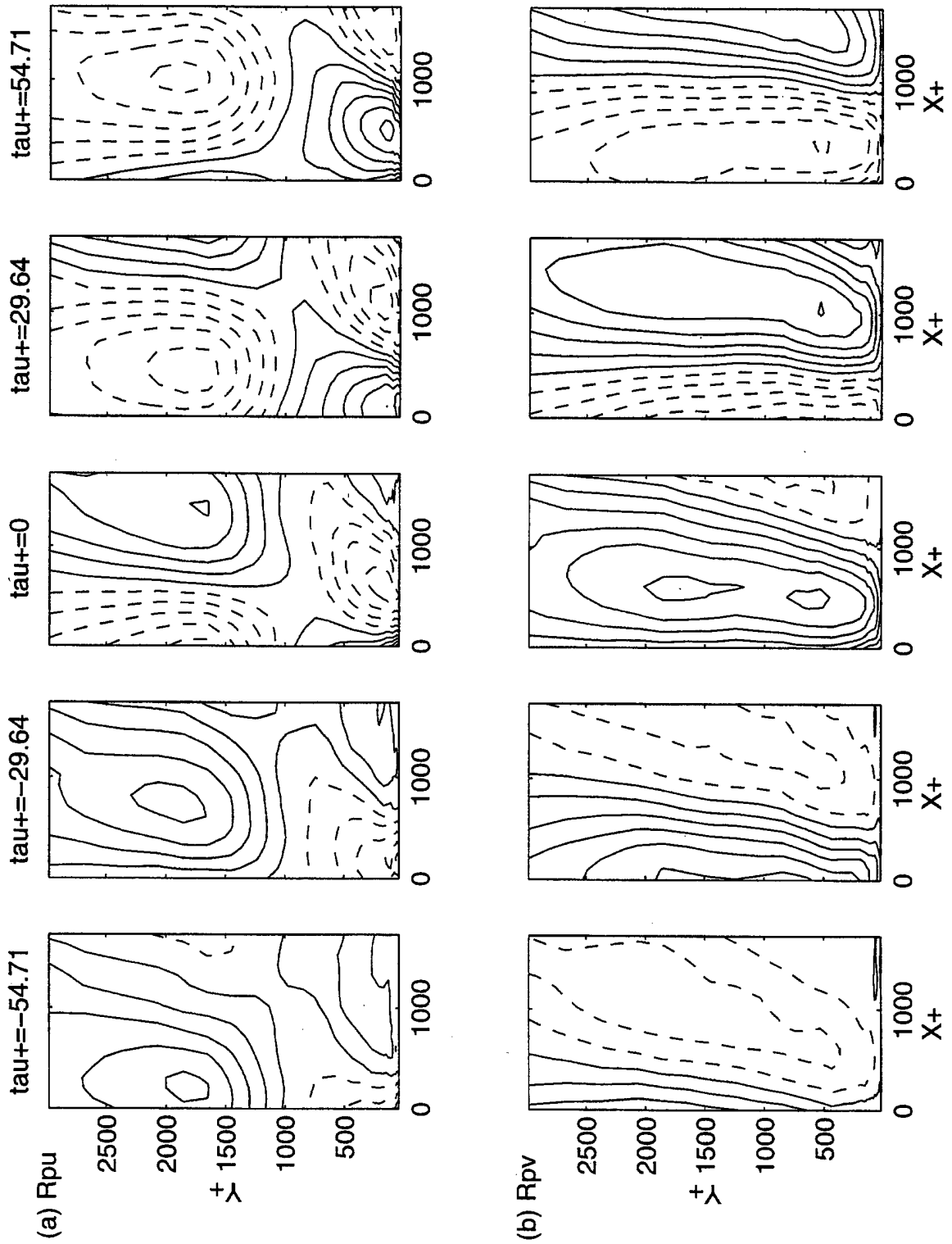
Figure 5.7: Streamwise filter 1 pressure-velocity correlation contours at selected time delays
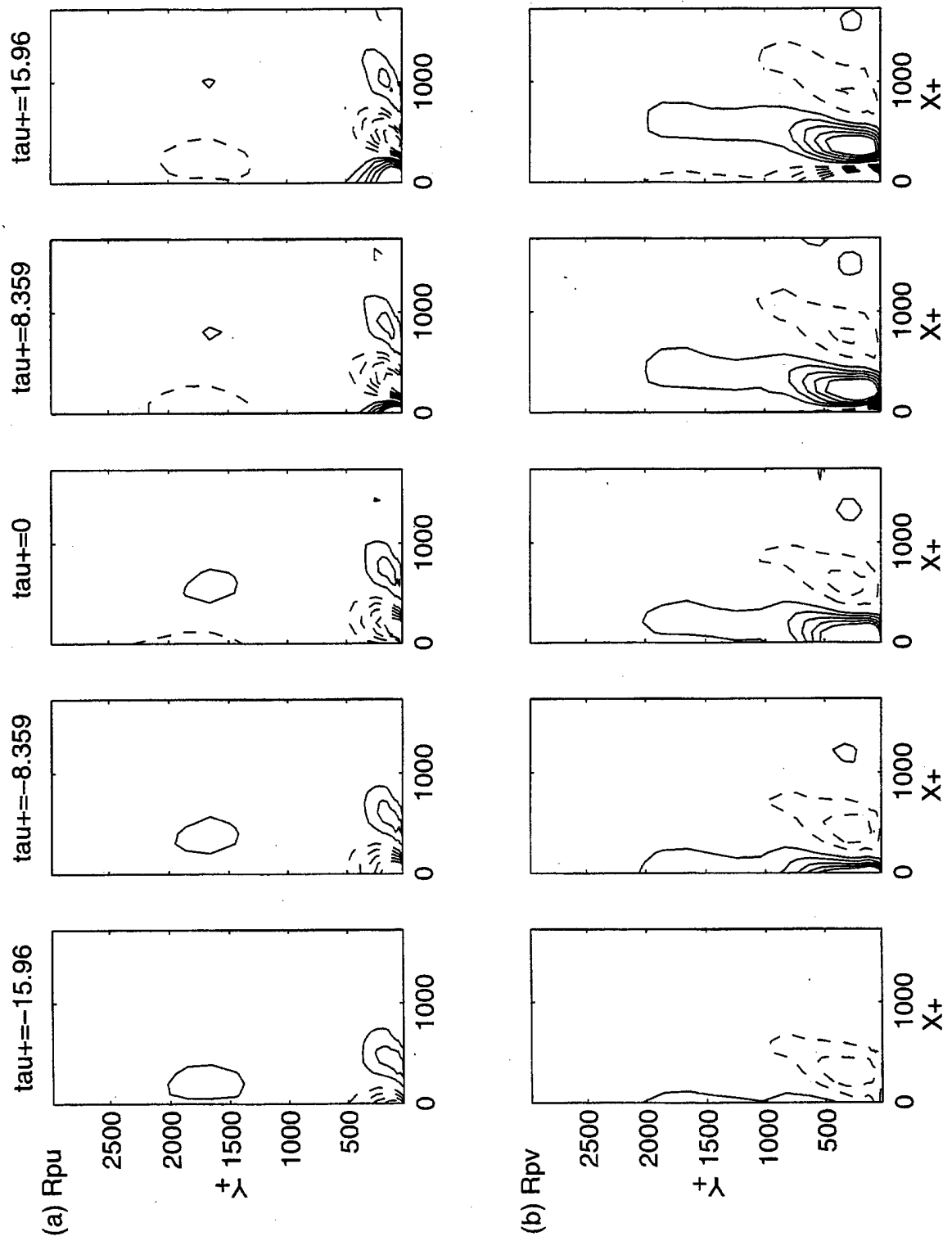
Figure 5.8: Streamwise filter 2 pressure-velocity correlation contours at selected time delays

5.9. Due to the small streamwise scale of these structures, these data were not smoothed in the x-direction. Nonetheless, the streamwise scale of these structures is nearly too small to resolve with the transducers used. However, the sign change between R_{pu} and R_{pv} contours with streamwise distance, though it occurs within the diameter of one transducer, suggests that the mean streamwise characteristics of these structures is being captured. Some of the features of the filter 2 structures are evident in these data. These features include the dominance of the pv correlation seen in the vertical extent of the contours, and the 180-degree phase shift between R_{pu} and R_{pv} contours. These contours also indicate as many as three vortical structures (6 contours) in the streamwise direction.

Other features unique to the filter 3 pressure-velocity contours are more subtle and require careful examination. One feature is the inclination angle of the structures. One could argue, based on the $\tau = 0$, R_{pu} contour, that the structures are distorted by the mean flow, having no inclination up to $y^+ = 100$ and becoming more inclined as y^+ increases to 200. This feature is very subtle and the pv correlation contours show no measurable inclination.

The second feature unique to the filter 3 pu correlation contours is the phase reversal within the vertical extent of the structure. These smaller contours above $y^+ = 100$ would be consistent with secondary motions associated with the near-wall ejection/sweep type motions that are responsible for wall pressure fluctuations at these frequencies. The fact that these secondary flow effects are not evident in the R_{pv} contours could be due to the resolution of the array but is more likely an artifact of the strong pv correlation that exists throughout the flow field.
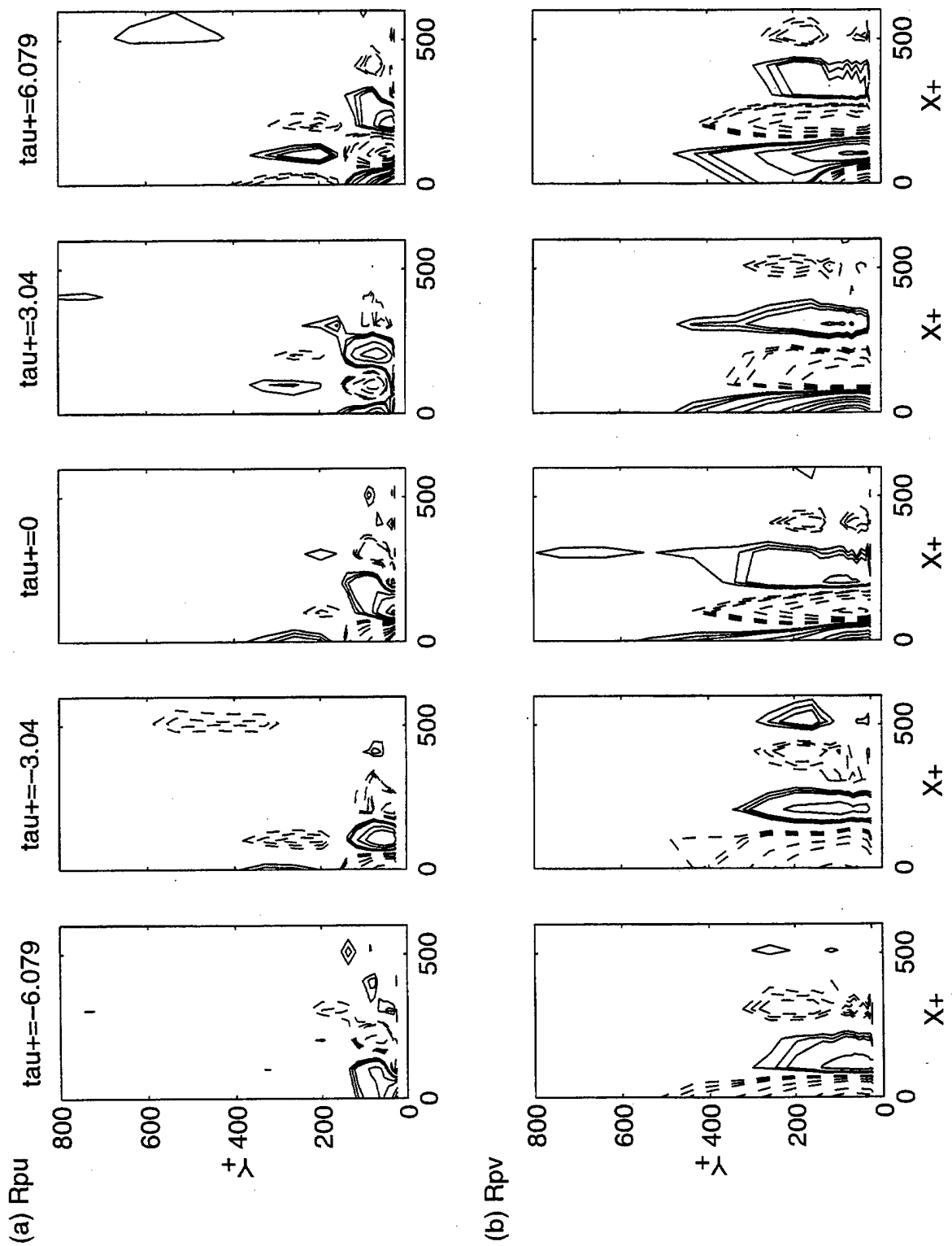
Figure 5.9: Filter 3 pressure-velocity correlation contours at selected time delays

5.1.2 Spanwise Analysis

The last set of measurements performed in this investigation was the simultaneous wall pressure and flow field measurements utilizing the spanwise array. This experiment consisted of three boundary layer surveys to one side of the transducer array such that the total measurement plane measured 3000 x 1000 viscous units in an 18x30 rectangular grid. Cross-spectral and cross-correlation measurements made at each pressure-velocity station within the spanwise grid are presented in this section.

Cross-Spectral Analysis

Contours of mean pu and pv coherence in the frequency bands of filters 1, 2, and 3 are shown in figures 5.10, 5.11, and 5.12 respectively. Many of the global features shown by the coherence contours in the spanwise measurement grid are consistent with those shown in the streamwise data. However, some of the more detailed features of the organized motions are visible in the spanwise coherence and correlation data.

The very large scale structures (irrotational and near-wall δ-scale) are depicted in contours in figure 5.10 for the **filter 1 band**. These results strongly confirm the findings of the streamwise coherence contours in figure 5.2. In fact, the relative scales of the irrotational versus the near wall structures is more evident when viewed in the spanwise plane. The irrotational motions appear to have a vertical coherent extent of as much as 3δ and a comparable spanwise extent. The flattening of the contours due to inclination and convection are not present in these data and the structures appear to be spanwise symmetrical. The near wall structures isolated by filter 1 have a spanwise extent (as measured by Γ_{pu}) of only 300 to 400 viscous wall units ($\sim 0.3\delta$). The discrimination of near-wall and irrotational motions in the pv coherence contours is obscured by the strong correlation between v and p which causes the contours to overlap. There are however, two distinct coherence peaks (near-wall and irrotational)

120
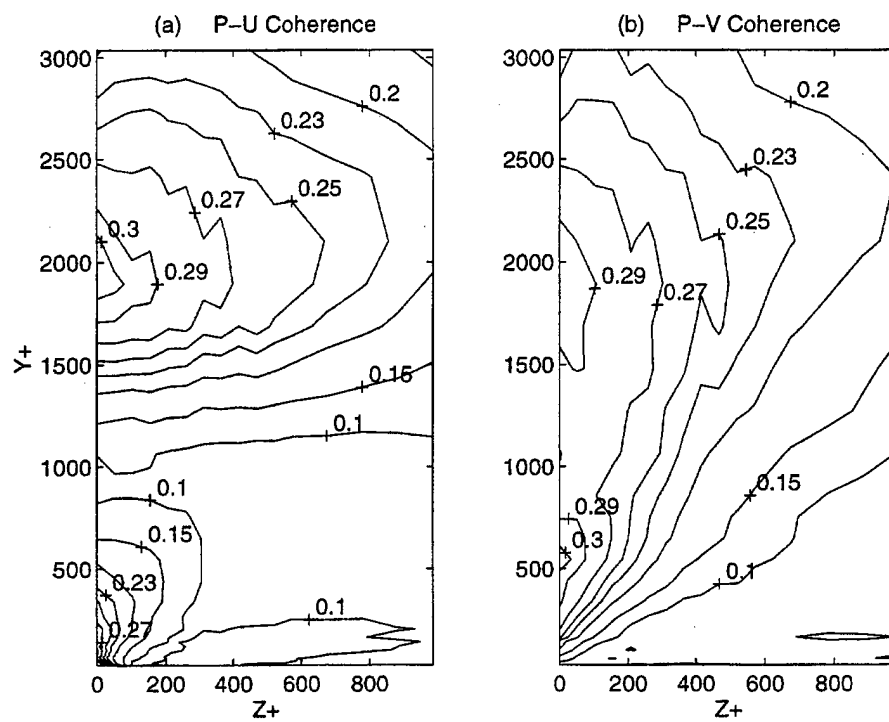
Figure 5.10: Filter 1 pressure-velocity coherence contours in the spanwise measurement grid

in both Γ_{pu} and Γ_{pv}. The near wall Γ_{pv} peak is at a higher y^+ location than the Γ_{pu} peak. This is consistent with the streamwise contours and indicates that the mean structure responsible for fluctuating wall pressure is characterized by near wall shear stress and large v components at a finite distance above the wall, i.e., Reynolds stress activity.

The apparent secondary flow structure seen in the near wall Γ_{pu} contours is evidence that the δ-scale near wall structures in the filter 1 frequency band contain secondary flow effects. However, the pv coherence contours do not indicate the secondary flow. This behavior is currently unexplained.

In general, the spanwise filter 1 coherence contours confirm the idea that two dominant pressure producing turbulent scales exist within the frequency band of filter 1. These structures, the irrotational (3δ) and the near-wall δ-scale motions coexist in the turbulent boundary layer. The low frequency double hump in the near wall velocity spectra in figure 2.10 occur at approximately 100 Hz and 300 Hz, consistent with the presence of two dominant scales in the filter 1 frequency band. The wall pressure signatures of these structures are similar enough so as to reveal them both in the pressure-velocity coherence contours.

Coherence contours for the **filter 2 band** are shown in figure 5.11. The global features of these data are consistent with the streamwise contours in figure 5.3. While Γ_{pu} peaks at the wall (or the closest measurement station to the wall), Γ_{pv} peaks at approximately $y^+ \approx 150$. Also, the dominance of the pv correlation is evident in the large vertical extent of the pv contours. The filter 2 coherence contours do not show measurable secondary flow effects like the filter 1 data, however, the bulge in the $\Gamma_{pu} = 0.1$ contour below $y^+ \approx 100$ may be evidence of some secondary structure in that region. The most noteworthy difference in the filter 1 and filter 2 Γ_{pu} shapes is the behavior below $y^+ \approx 100$. While the filter 1 contours neck down in this region,
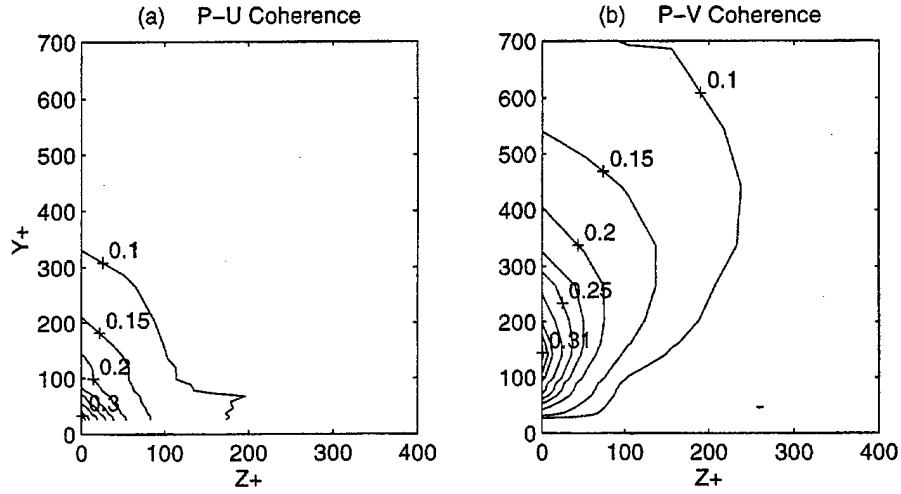
Figure 5.11: Filter 2 pressure-velocity coherence contours in the spanwise measurement grid

the filter 2 contours expand with decreasing y^+. This could also be an artifact of a small scale secondary flow, too small to accurately resolve with the measurement grid.

Finally, the high frequency pu and pv coherence contours for the **filter 3 band** are given in figures 5.12a and b. Along with the lower overall coherence levels and the small spatial extent, these data are consistent with the streamwise contours in figure 5.4. The peak in Γ_{pv} occurs at $y^+ \approx 50$ and Γ_{pu} peaks nearer or at the wall. No measurable secondary flow effects are visible other than the slight bulge in the near wall ($y^+ < 50$) contours. This behavior is very subtle and is not yet considered reliable evidence of secondary flow effects.

The spanwise coherence contours are in general agreement with the streamwise coherence contours and confirm the multi-layer, multi-scale structure of the turbulent boundary layer. The measured spanwise extent relative to the streamwise extent of the pressure producing structures illustrates the streamwise alignment and convection effects of the large and small scale turbulent structures.
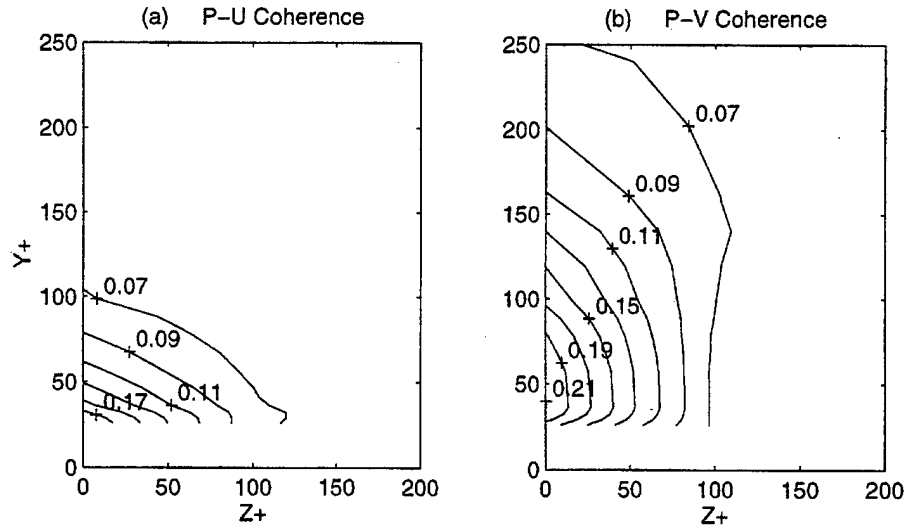
Figure 5.12: Filter 3 pressure-velocity coherence contours in the spanwise measurement grid

Cross-Correlation Results

Figure 5.13 shows the spanwise contours of R_{pu} and R_{pv} for **filter 0 (unfiltered) time records**. These results are presented at the same time delays as the data for the streamwise contours in figure 5.6. The multi-layer features (irrotational and near-wall structures) of these data are consistent with the spanwise filter 1 coherence contours (figure 5.10) as well as the streamwise filter 0 and filter 1 correlation contours. Furthermore, the near-wall spanwise contours displayed at $z^+ = 0$ are consistent with the streamwise contours at $x^+ = 0$ contours in figure 5.6. These curves may then be considered spanwise 'snapshots' of the convecting structures shown in figure 5.6. However, these 'snapshots' do not indicate streamwise vorticity, and their interpretation will be strictly qualitative.

The weak near-wall secondary flows identified in the spanwise pu coherence contours previously shown in figure 5.10 can be seen in the R_{pu} contours in figure 5.13a. It should be noted that these are streamwise counter flows, or regions in which u changes sign from the primary contour. They do not necessarily indicate a sec-

124
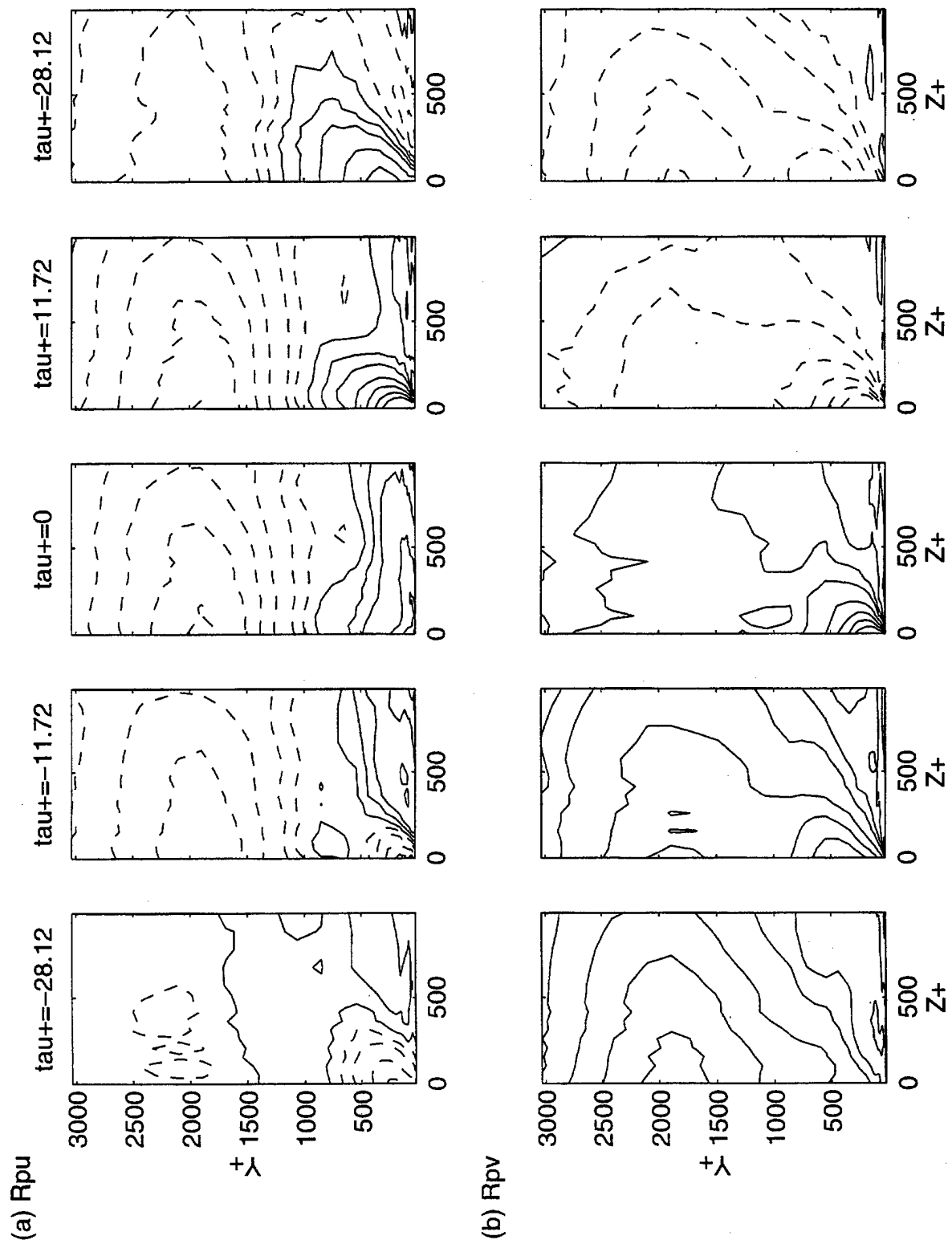
Figure 5.13: Streamwise filter 0 pressure-velocity correlation contours at selected time delays

ondary, streamwise oriented vortical structure. In fact, these secondary flows do not appear to be associated with a v component strong enough to be seen in the R_{pv} contours of figure 5.13b. However, they could be obscured by the strong pv correlation throughout the flow field. By comparing the streamwise unfiltered correlations in figure 5.6a with the spanwise unfiltered correlations in figure 5.13a, it appears that the secondary flow contours are most visible when the peaks of the near-wall, streamwise pu correlation contours are located at approximately $x^+=0$, i.e., when the strongest R_{pu} level (streamwise velocity fluctuation) occurs directly above the reference transducer (at $\tau^+ \sim$-12 and +12).

By comparing the signs of the near-wall contours in figures 5.13a and b, it is possible to track the orientation of the velocity field as these structures convect downstream. The sequence at the five time delays shown in figure 5.13, in terms of the quadrant method (discussed in Chapter 1) is Q2-Q2-Q1-Q4-Q4. This sequence indicates that these motions are Reynolds stress producing structures. It is possible that the counter flows seen in the R_{pu} contours are part of the composite ejection/sweep process. The Q2-Q1-Q4 quadrant motion was shown by Nagano and Tagawa [35] to be one of the dominant contributors to Reynolds stresses in the near wall boundary layer. In suppport of this observation, Jayasundera, Casarella, and Russell [22] demonstrated that the Q2-Q1-Q4 trajectory is the dominant contributor to RMS wall pressure across the entire boundary layer.

Contours of R_{pu} and R_{pv} for the **filter 1 time records** are shown in figure 5.14a and b. As with the streamwise correlation contours, these data strongly resemble the unfiltered results in figure 5.13. The $\tau=0$, R_{pu} contours show the near wall secondary flow slightly better, as do the non-zero time delay contours. The R_{pv} contours still fail to show the secondary flow effects and have, in fact, lost some of the near wall structural features present in the unfiltered data. This is consistent with the
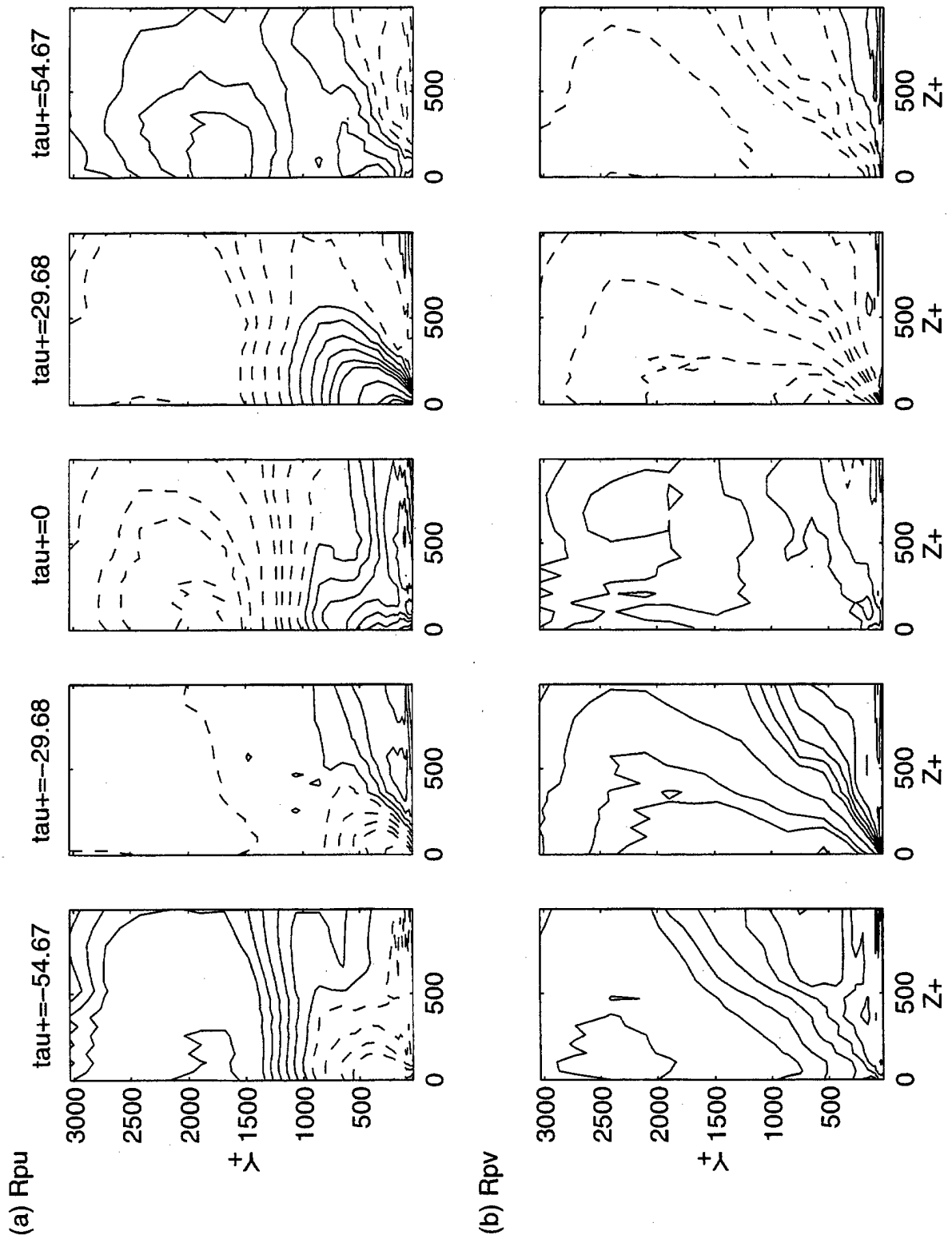
Figure 5.14: Streamwise filter 1 pressure-velocity correlation contours at selected time delays

127

behavior of the streamwise R_{pv} contours when subject to filter 1; the discrimination between irrotational and near-wall structures becomes more difficult as the contour lines begin to overlap.

The quadrant sequence of the near wall structures is identical to that for the unfiltered data (Q2-Q2-Q1-Q4-Q4) despite the larger time delays at which the contours are computed. This result suggests that the values of τ chosen, based on peaks and axis crossings in R_{pp}, may be characteristic times in the ejection/sweep cycle of large and small scale motions. Further evidence of this finding is contained in the high frequency data.

Spanwise pressure-velocity correlation contours of the **filter 2 time records** are shown in figure 5.15. As with the filter 0 and filter 1 data, the small scale, near-wall secondary flows seen in the R_{pu} contours do not appear to be coupled with a strong enough v component to show up in the R_{pv} contours. And like the large scale structures seen in the filter 0 and filter 1 contours, the secondary flows are most visible when the peak near-wall correlation in figure 5.8a is centered above the transducer at $x^+=0$, i.e., in a region of strong streamwise velocity (τ^+=-8 and +15 in figure 5.8). The quadrant sequence of the primary contours in the filter 2 correlations are also identical to the near wall filter 0 and filter 1 structures (Q2-Q2-Q1-Q4-Q4). This result confirms that the the values of τ chosen may be characteristic in the ejection/sweep cycle of the large and small scale structures. These data also support the argument that the spanwise secondary motions are strongest at periods of large streamwise velocity (shear stress) in the ejection/sweep cycle.

The high frequency spanwise correlation contours for the **filter 3 time records** are shown in figure 5.16. As with the streamwise correlations, these data have not been smoothed in the Z-direction. The phase relationships of these scales are more difficult to observe but are still visible in the data and are consistent with the
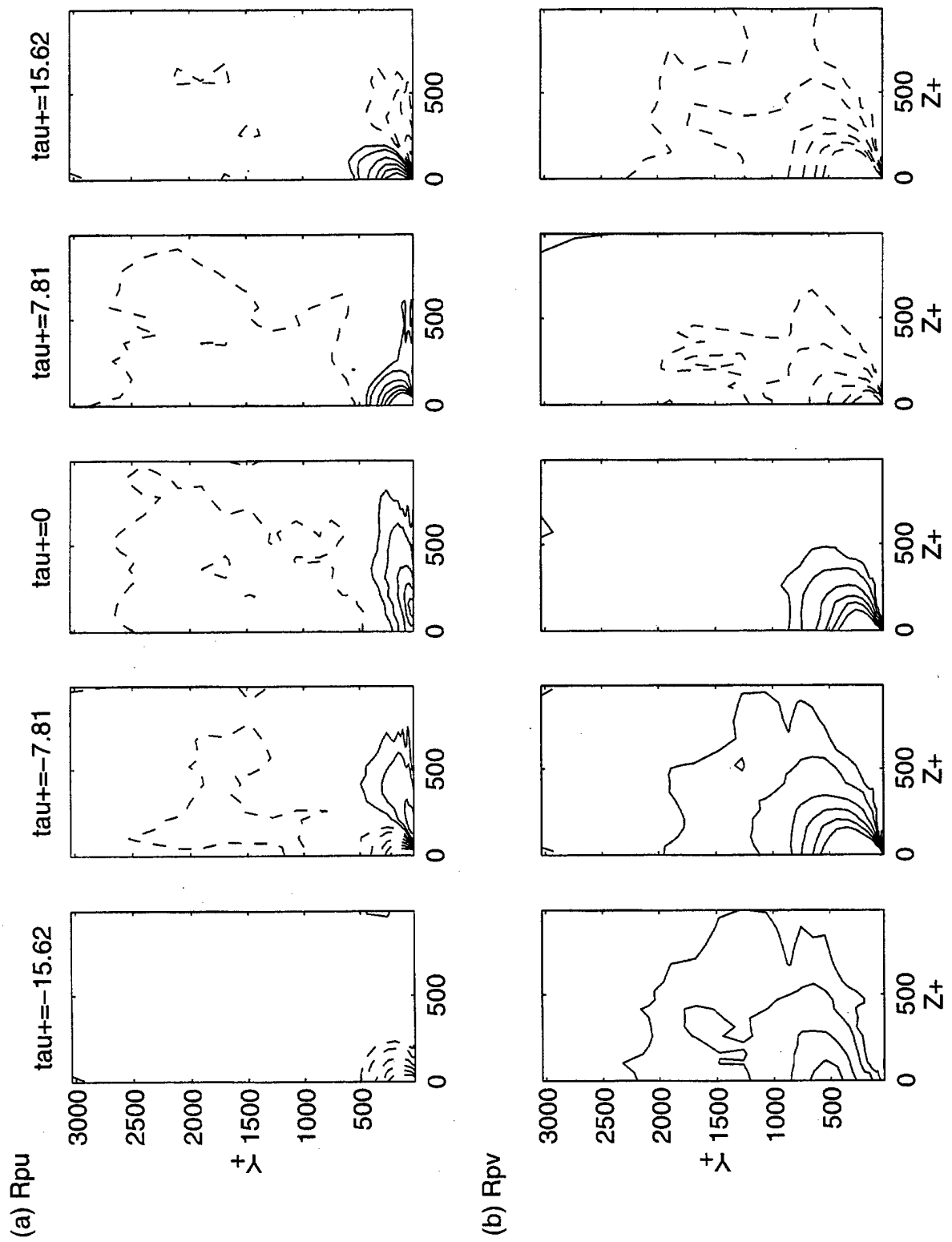
Figure 5.15: Streamwise filter 2 pressure-velocity correlation contours at selected time delays

general trends shown by the filter 1 and 2 contours. The spanwise secondary flows are most visible at times when the streamwise contours exhibit strong streamwise activity (peak R_{pu}). Furthermore, the secondary motions seen above the near-wall structures in the streamwise R_{pu} contours are also seen in these data. These data also support the findings from the filter 2 data that these secondary motions occur at times of large near wall streamwise shear stress. (τ^+=0 and 6.2 in figures 5.9 and 5.16). Finally, the quadrant sequence of the primary filter 3 contours at the given time delays (Q3-Q2-Q2-Q1-Q4) is consistent with the results of filters 0, 1, and 2, indicating the expected correlation between high frequency wall pressure fluctuations and near wall Reynolds stress activities.

In summary, by collectively examining the cross-spectral and cross-correlation measurements between filtered pressure and velocity signals in both the streamwise and spanwise grids, important characteristics of the pressure producing turbulent structures have been elucidated. In addition to the spatial extent of the observed structures isolated by filters 1, 2, and 3, the phase relationships between turbulent components of these structures and the wall pressure were determined. The inner layer flow structure appears to be a composite of filter 2 and filter 3 scales which exhibits a common dynamical behavior consisting of ejection/sweep type motions.

The coherence and correlation results also confirm the inclination and convective features of the large and small scale structures observed by other investigators. On the other hand, it could be argued from these data that the behavior of the small scale ($y^+ \leq 200$) near-wall turbulent production activity, cited by most investigators as the dominant source of Reynolds stresses in a turbulent boundary layer, can only be revealed from pressure-velocity correlation measurements by filtering out the large scale, irrotational motions which would otherwise dominate the results.

Finally, the visual display format allowed by the pressure-velocity correlation
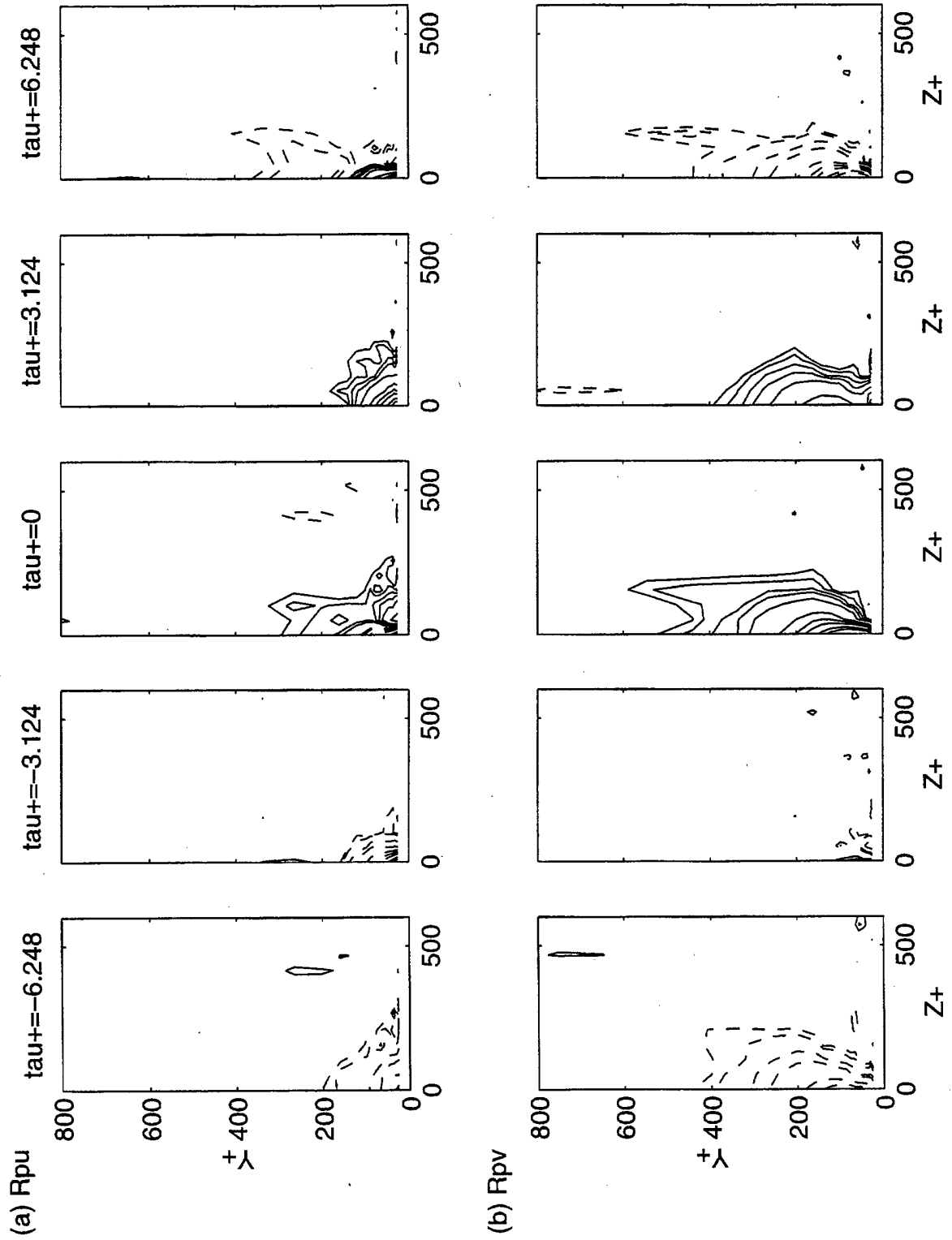
Figure 5.16: Streamwise filter 3 pressure-velocity correlation contours at selected time delays

contours was able to identify secondary flow structures associated with the large and small scale ejection/sweep type motions, particularly during periods of strong streamwise near-wall shear stress. The conditional sampling results to be presented will further illustrate features of the flow structures inferred from the pressure-velocity correlation results.

5.2   Conditional Sampling Results

At every pressure-velocity station in the streamwise measurement grid, wall pressure and the u and v components of velocity were simultaneously sampled for 10 seconds. The cross-spectral and cross-correlation computations between each pressure-velocity pair were presented in the previous section. Those correlation results successfully defined the spatial extent of the pressure producing turbulent structures and provided important phase information which allowed inferences to be made about the dynamics of these structures. Another technique for visualizing the flow field associated with wall pressure events is to conditionally sample the velocity field based on the detection of wall pressure events and then ensemble average the results.

In Chapters 3 and 4, the complexity of conditional sampling was discussed in detail. The sensitivity of the results to the detection criteria as well as the added complexity of filtering are a few of the factors to be considered when interpreting conditional sampling results. Up to this point, only wall pressure signals have been sampled and averaged. Now, by sampling the flow field (u, v) on wall pressure events, several more variations have been added to the already complex nature of this technique. In addition to the detection criteria and filtering issues, there are now different methods of presentation to choose from, each of which must be carefully interpreted.

Two basic techniques for flow field visualization will be used. The first technique

utilizes the entire array of transducers to produce a database of pressure and velocity time records in the streamwise measurement grid. At each station in the streamwise measurement grid, the velocity vectors (u and v) are sampled at times corresponding to large amplitude wall pressure events ($k = \pm 2$) at location $(x^+, y^+)=(0,0)$. The velocity samples are then ensemble averaged. Vector or 'quiver' plots of the average velocities are then plotted in a map in which the quivers are physically located at the measurement position (x^+, y^+) relative to the fixed reference pressure transducer. Quiver plots presented in this fashion will be hereinafter referred to as conditionally averaged 'maps' of the flow field. This technique will be heavily relied upon since it provides what is thought to be the most realistic depiction of the flow field associated with large amplitude wall pressure events.

The second technique for presenting conditionally sampled velocity data is that pioneered by Kammeyer [25] using a single pressure transducer and a single velocity (u, v) survey. For this technique, in which the ensemble averaged velocity time records are played back, an effective streamwise (x) axis is computed from an assumed convection velocity ($x^+ = U_c^+ t^+$). The average velocity time record from each y location in the survey is then vector plotted at that y location. The 'Taylor plots' created using this method are based on an assumption of a frozen, convecting flow field which changes negligibly in the time window viewed. While this technique is not as well based as the flow field maps, it has the distinct advantage of an essentially unlimited streamwise resolution, limited only by the sample time ($1/f_s$). This improved resolution will prove to to have an advantage in visualizing the small scale, near-wall, filter 3 flow structures.

The conditional sampling results given in this chapter are based on a common set of wall pressure event detection criteria: large amplitude, positive and negative ($k = \pm 2$) peak events. These peak events were detected in unfiltered (filter 0) as well

133

Table 5.2: Conditionally Averaged Flow Field Data to be Presented

Wall Pressure Events	Cond. Avg. (u,v)
Filter 0 (k=±2)	Filter 0
Filter 1 (k=±2)	Filter 0, Filter 1
Filter 2 (k=±2)	Filter 0, Filter 2, Filter 3
Filter 3 (k=±2)	Filter 0, Filter 3

as filter 1, 2, and 3 wall pressure time records. In addition, the u and v time records subject to the same filtering were ensemble averaged at peak pressure detection times. Table 5.2 summarizes the ensemble averaged velocity data to be presented and discussed in this section. It will be shown that the features of the ensemble averaged flow field associated with wall pressure events are highly dependent the filtering applied to the flow field (u and v). Many variations of pressure and velocity filtering were tested but are too numerous to include in this document. The data to be presented are believed to best illustrate the relationships between wall pressure and velocity, as well as relationships between different turbulent scales.

A final issue for the presentation of these results is the manner in which the quivers are scaled in the figures. One choice is to scale the length of the vectors by their absolute magnitude (m/s). This method is the most realistic but has an important drawback. The near wall velocity excursions associated with large amplitude wall pressure events tend to be more violent than the velocity excursions in the outer and irrotational flow regions. So by uniformly scaling the velocity vectors, the irrotational motions are not seen. The second choice is to scale the length of the vectors by their RMS value at each y location. The irrotational motions as well as the near-wall structures are then both clearly visible in the flow map. To illustrate the entire extent of the large and small scale motions, the second method will be used exclusively.

5.2.1 Flow Field Mapping Results

The four conditionally averaged maps in figure 5.17 show the **unfiltered** (filter 0) **average flow field** conditionally sampled on **filter 0** and **filter 1**, for both positive and negative peak **wall pressure events**. It should be noted that the detection of peak wall pressure events occurs at location $(x^+, y^+) = (0,0)$, therefore, the flow field maps depicted in this section illustrate the behavior of u and v downstream of a peak wall pressure event.

As seen in figures 5.17a and b, the RMS normalization of u and v at each y location enables both the induced irrotational and near wall motions associated with positive wall pressure events to be displayed in the same figure. In fact, by inflating the size of the outer and irrotational flow quivers (regions of low u'_{rms} and v'_{rms}), the near wall and irrotational motions begin to appear as parts of a single structure. This effect is even more dramatic in figures 5.17c and d where the flow field is strictly sampled on the filter 1 wall pressure events. This effect should be considered an illusion, and the irrotational and near wall motions only appear together in these data due only to their similar wall pressure signatures.

Figures 5.17b and 5.17d are the unfiltered flow fields associated with filter 0 and filter 1 negative wall pressure events, respectively. As discussed in Chapter 4, peak events, in any wall pressure time record, tend to occur in groups, or at least pairs of positive and negative peaks. For this reason, the flow fields associated with positive and negative wall pressure peaks are shown side by side in these figures so that a composite picture of an entire flow structure can be inferred.

Outside the boundary layer, the unfiltered flow fields conditionally averaged on unfiltered wall pressure events (figures 5.17a and b), and low frequency (filter 1) pressure events (figures 5.17c and d) are nearly identical. At x=0, positive peak pressure appears to follow a region of strong positive upward velocity while negative

135
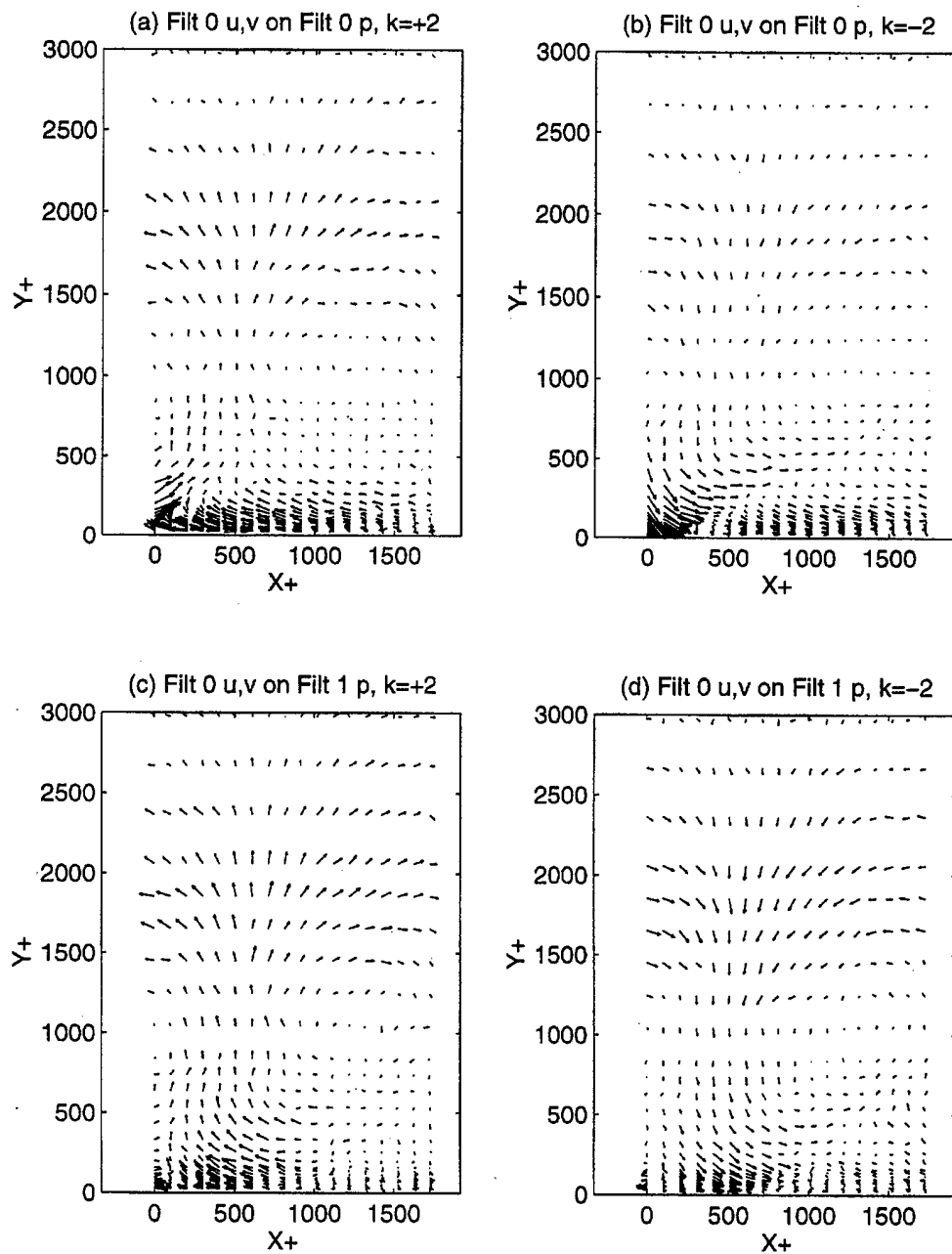
Figure 5.17: Unfiltered average flow field conditionally sampled on filter 0 and filter 1 positive and negative peak wall pressure events

peak pressures appear to follow strong inward flow. By sampling exclusively on large scale events, the consistency of the vector lengths and directions in figure 5.17c and d appear more uniform or organized. Recall from table 3.2 that there are typically 10 times as many large amplitude wall pressure events detected in the filter 0 time records than in the filter 1 time records. In other words, by averaging the velocity signals over 1/10 as many, scale biased (filter 1) events, the unfiltered flow field retains its dominant features and appears "cleaner".

The near-wall motions depicted for the positive and negative peak events in figures 5.17a and b are similar in their basic structure. The most significant difference is the behavior near $x^+=0$, where the positive pressure event shows an ejection, and the negative pressure event shows a sweep. Downstream of the sweep in figure 5.17b there appears to be an extended region of negative shear stress, coupled with an ejection type motion. In other words, the unfiltered flow field downstream of a negative wall pressure peak is characterized by ejection and sweep type motions, which when combined, appear like an inclined shear layer. One could argue that the flow field associated with a positive peak event in figure 5.17a is a phase shifted duplicate of figure 5.17b, i.e., we are seeing snapshots of the same structure at two different times. The same general features are shown in figures 5.17c and d, however, the near wall motions are more difficult to discriminate from the irrotational motions.

The four conditionally averaged maps in figure 5.18 show the **filter 0 (unfiltered) average flow field** conditionally sampled on **filter 2** and **filter 3** positive and negative peak **wall pressure events**. When the unfiltered flow field is conditionally averaged on filter 2 wall pressure events, the irrotational motions no longer appear as organized vector fields in the flow field maps. This is further confirmation that the near-wall filter 2 scale structures are not directly correlated with irrotational scales. For this reason, only the boundary layer regions ($y^+ < 1000$) are shown in
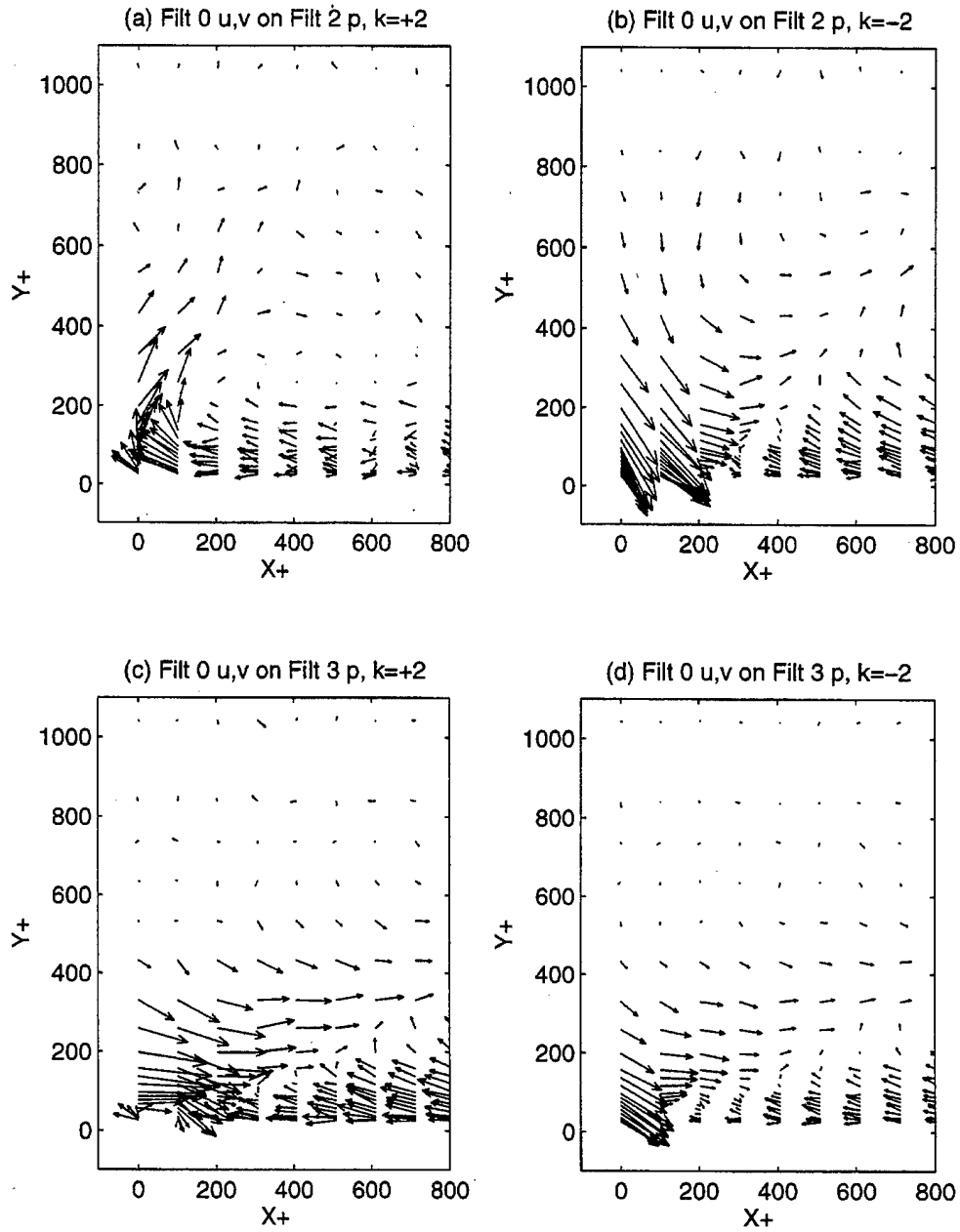
Figure 5.18: Unfiltered average flow field conditionally sampled on filter 2 and filter 3 positive and negative peak wall pressure events

these figures. The flow field associated with filter 2 wall pressures shown in figures 5.18a and b resembles the near wall structures in the unfiltered maps shown in figures 5.17a and b, however, the spatial extent of the organized vector fields is slightly reduced. The positive pressure event is again characterized by the reverse flow and ejection motion, whereas the negative pressure event is characterized by a sweep, which happens to follow a negative shear stress and ejection motion. The coupling of the positive and negative peaks as components of the total footprint of large scale ejection/sweep type motions is clearly demonstrated in these data.

The results presented earlier in Chapter 4 indicated a correlation between high frequency (filter 3) clusters of wall pressure activity and larger scale (filter 2) peak events. The maps in figures 5.18c and d similarly illustrate a relationship between large and small scale structures. In these figures, the unfiltered flow field is conditionally averaged on filter 3, positive and negative wall pressure events. Two important features should be noted. The first is the familiar large scale, near-wall shear stress region which extends far beyond the streamwise extent of the plots (out to at least $x^+ \approx 1800$). The large scale sweep of fluid, coupled with the near wall shear stress region combine to form an inclined shear layer across the boundary layer. This large scale shear layer, by virtue of its strong presence in these data, is correlated with high frequency (filter 3) wall pressure activity.

The second observation is of activity in the near-wall region ($y^+ \leq 100$ and $x^+ \leq 200$). Upon close examination of figures 5.18c and d in this region, the near wall turbulent structure associated with the filter 3 wall pressure event is visible. The first two x locations of velocity vectors in figure 5.18c indicate a small ejection (Q2) and sweep (Q4), respectively. Since the scale of these structures are on the order of the transducer spacing, their detailed shape is not clear, however, they clearly contain Q2 and Q4 motions. The flow field associated with a negative pressure event shown

in figure 5.18d contains further evidence of the small scale structure at $x^+ \approx 200$. In this figure, the rotational motion of the structure is weakly visible. It appears as though the small scale structure rotates clockwise as it is swept along by the large scale shear layer. The resemblance between figures 5.18c and d is again strong, and they appear only to differ by a finite phase shift. Though the small scale activity may have a larger vertical and streamwise extent than is indicated in figures 5.18c and d, the dominance of the large scale shear layer in these data appears to have a masking effect. By removing the large scale component of the velocity signals, it is hoped that a more refined image of these near wall structures will be revealed.

The velocity data presented in figure 5.19 are subject to the same filtering as the wall pressure on which their sampling was based. Figures 5.19a and b show the **filter2 average flow field** conditionally sampled on **filter 2,** positive and negative, peak **wall pressure events**; while figures 5.19c and d show the **filter 3 average flow field** conditionally sampled on **filter 3,** positive and negative, peak **wall pressure events**. It should be noted that the filter 1 flow field conditionally averaged on filter 1 events is almost identical to the unfiltered flow fields shown in figures 5.17c and d and is therefore not presented.

The filter 2 flow structures are nominally consistent with the unfiltered flow results in figures 5.18a and b. However, the filtered flow field reveals a more organized, inclined structure, exhibiting the same ejection type motion. It also exhibits a near-wall "splat" feature at $x^+ \approx 400$ for the positive peak pressure detection in figure 5.19a. This splat motion, introduced in Chapter 1, appears to be a component of the ejection/sweep process for structures of filter 2 scale. The splat motion observed by other investigators is most likely the near wall component of any large or small sweep type motion.

The average flow field downstream of filter 2 negative wall pressure events, de-
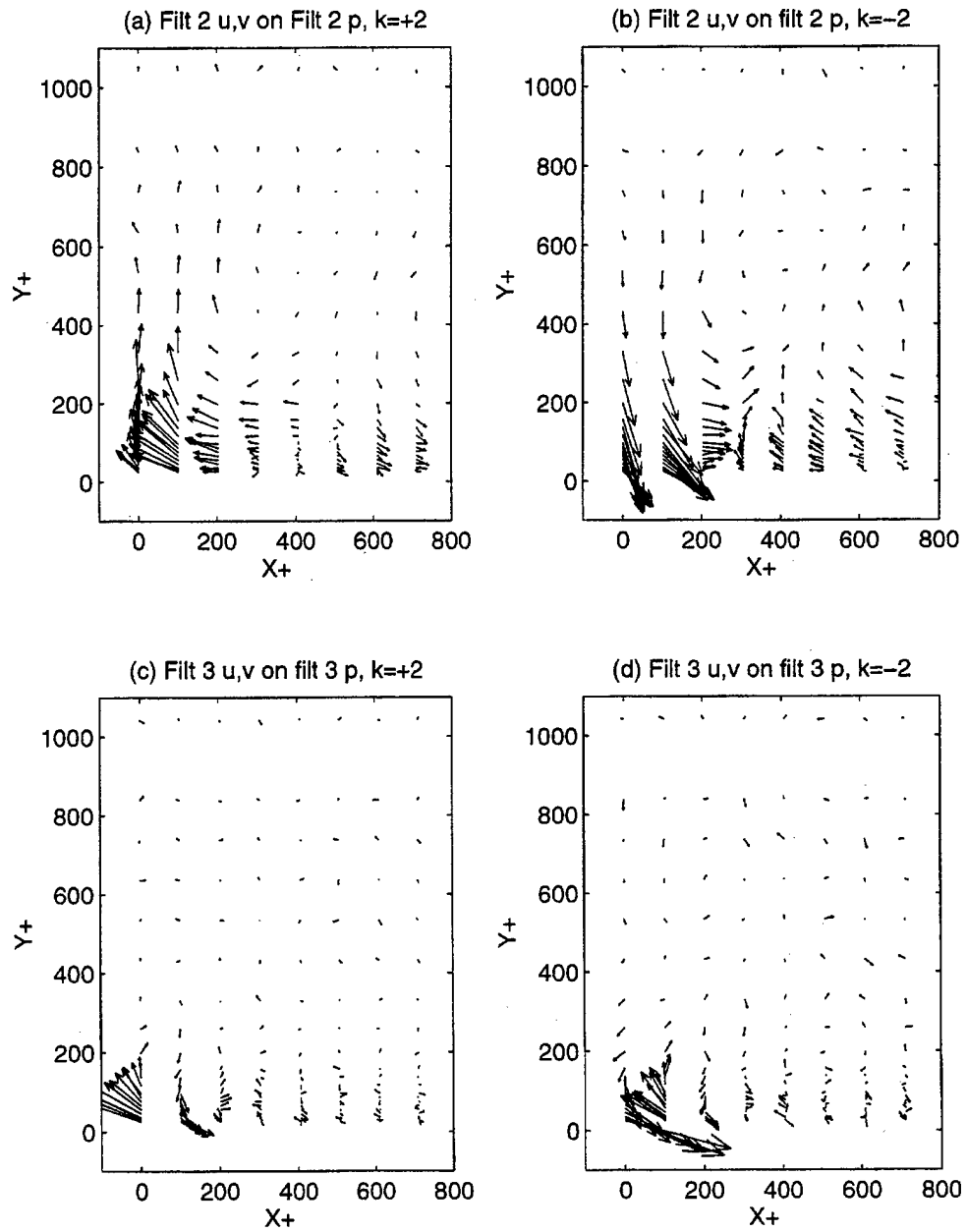
Figure 5.19: Filter 2 and filter 3 average flow fields conditionally sampled on positive and negative peak wall pressure events

picted in figure 5.19b, contains the characteristic sweep motion above the reference transducer. This is followed downstream by an ejection which occurs upstream of a region of strong near wall negative shear stress. These motions combine to form an inclined shear layer similar to that seen in the filter 0 flow fields. It should also be noted that by subjecting both the flow field (u, v) and wall pressure signal to filter 2, the conditional sampling results shown in figure 5.19 are consistent with the pressure-velocity correlation contours in figure 5.8.

For the unfiltered flow results in figures 5.18c and d, small scale near wall ejection/sweep motions associated with high frequency wall pressure fluctuations were shown to be associated with the passage of larger scale motions. By removing the larger scales from the velocity signals, a clearer image of the small scale motions is revealed. This is illustrated in figures 5.19c and d. The average filter 3 flow field associated with a positive peak pressure consists of a strong Q2 ejection directly above the transducer and a simultaneous Q4 sweep of fluid at the next transducer (100 viscous units downstream). There is evidence of organized activity up to 400 viscous units downstream. Similarly, the negative wall pressure event consists of a sweep and ejection motion in the opposite order. For example, a closer examination of the near-wall region ($y^+ \leq 200$) shows evidence of the small scale, rolling structure, however, since the large scale shear layer has been stripped away, the rolling structures appears larger, possibly 200 viscous units in diameter.

Since filter 3 peak events were shown to occur in clusters, one would expect to see a multitude of ejections and sweeps in figures 5.19c and d. These data do indicate the presence of additional near-wall organized activity, however, the resolution of the measurement grid, combined with the short correlation lengths of these scales, make it difficult to map the entire cluster of activity. An alternative method is needed to view the near wall turbulent activity with greater resolution. This is the primary

motivation for utilizing the Taylor method presented in the next section.

5.2.2   Flow Field Visualization Using Taylor's Assumption

The Taylor method described earlier was employed for two basic purposes: to qualify the results from the flow field mapping technique and to provide better resolution of the small scale turbulent motions associated with mid and high frequency (filters 2 and 3) wall pressure activity. It will be shown that the higher spatial resolution of this method compliments the flow field mapping technique and verifies the wall pressure signatures of the small scale motions. The correlation between small scale, near-wall (filter 3) turbulent activity and larger scale (filter 2) motions is also demonstrated.

In the previous section, comparisons were made between the filtered and unfiltered flow fields associated with various wall pressure events. These comparisons demonstrated the advantage of viewing conditionally averaged velocity signals subject to the same filtering as the pressure signal on which event detection is based. On the other hand, by viewing the unfiltered flow field, the correlation between large and small scale turbulent motions could be observed. For these reasons, both the unfiltered and filtered flow fields will be shown in this section using the Taylor method. The spatial regions to be depicted will be restricted to the near-wall and log-law regions ($y^+ < 600$). It should be also noted when observing the Taylor plots that the flow field upstream and downstream of the reference pressure transducer will be displayed.

The two flow fields shown in figure 5.20 are a Taylor plot of the **filter 0** (unfiltered) and **filter 2 average flow field** conditionally sampled on **filter 2**, positive (k=+2), peak **wall pressure events**. The ensemble averaged filter 2 wall pressure signature is shown at the bottom of the figure. The general features of the downstream unfiltered and filter 2 flow fields ($x^+ \geq 0$) in these figures are consistent with

143

Figure 5.20: Taylor plot of unfiltered and filter 2 flow fields conditionally sampled on filter 2 positive peak wall pressure events

the equivalent flow maps in figures 5.18a and 5.19a. This observation confirms that the turbulent motions isolated by filter 2 remain generally intact as they convect the span of the streamwise array. Furthermore, by viewing the filtered flow field with the enhanced streamwise resolution of this method, the rotational features of these structures is revealed, as are the rotating secondary motions upstream and downstream of the primary structure. In other words, rather than the large scale, inclined shear layer as this motion appears in the unfiltered flow field, by filtering, the vortical characteristics of these structures are revealed. The backs of these vortical structures are believed to comprise the shear layers described by Kline [29].

Relative to the pressure signatures, the ensemble averaged flow fields shown in these figures exhibit the same features previously observed in the flow field maps of positive and negative wall pressure events. The temporal increases in pressure are associated by ejection motions, while a drop in pressure signifies an inrush or sweep of fluid toward the wall. As previously proposed, these motions may be associated with the passage of counter rotating vortical structures, or alternatively, the vortical structures are a product of the mean flow interaction with the ejection/sweep process. The mechanism which initiates these structures cannot be determined from the data and is clearly beyond the scope of this investigation.

The advantage of the enhanced streamwise resolution from Taylor plots is best illustrated by viewing the flow field associated with high frequency (filter 3) wall pressure events. The two flow fields shown in figure 5.21 are the **filter 0 and filter 3 averaged flow field** conditionally sampled on **filter 3**, positive, peak **wall pressure events**. The ensemble averaged wall pressure signature of the event is shown at the bottom of the figure. The ensemble averaged unfiltered flow field in figure 5.21 is nearly identical to that measured by Laadhari [33] based on positive peak wall pressure events. These data are also in excellent agreement with the equiv-

alent flow maps in figures 5.18c and 5.19c. The Taylor plots allow a much improved view of the small scale rolling vortical structure below the shear layer in the unfiltered flow field. Furthermore, this figure dramatically demonstrates the benefit of filtering the flow field to reveal small scale vortical structures which are masked by the large scale motions associated with the small scale events. As many as six, counter-rotating near-wall vortical structures can be identified in the filter 3 flow field.

The separation distance between the wall pressure transducers ($\Delta x^+ \approx 100$) which limits the capability of the flow field mapping technique, is shown in figure 5.21 to be nominally the diameter of the vortical structures captured by filter 3. The difficulty of the mapping technique to resolve these structures is therefore not surprising. The wall pressure signature of these motions also follows the ejection and sweep pattern demonstrated by the larger scale motions.

The flow field Taylor plots previously shown confirm the correlation between large scale motions and small scale, near-wall turbulent activity. This question is directly addressed with the next calculation. Figure 5.22 shows the **filter 3 average flow field** conditionally sampled on **filter 2** positive **wall pressure events**. The results clearly demonstrate the correlation between filter 2 wall pressure events and small scale, filter 3 turbulent activity. The u and v velocity signals subjected to filter 0 and filter 2, shown in figure 5.20, are shown in figure 5.22 subjected to filter 3. In other words, this is the ensemble averaged high frequency (filter 3) flow field associated with filter 2 scale, positive peak wall pressure events.

Recalling the wall pressure time records presented in section 4.2, it was observed that many filter 2 peak wall pressure events were not accompanied by clusters of high frequency (filter 3) activity. It is not surprising that the Taylor plot of the high frequency flow field in figure 5.22 does not show clear vortical structures. This is due
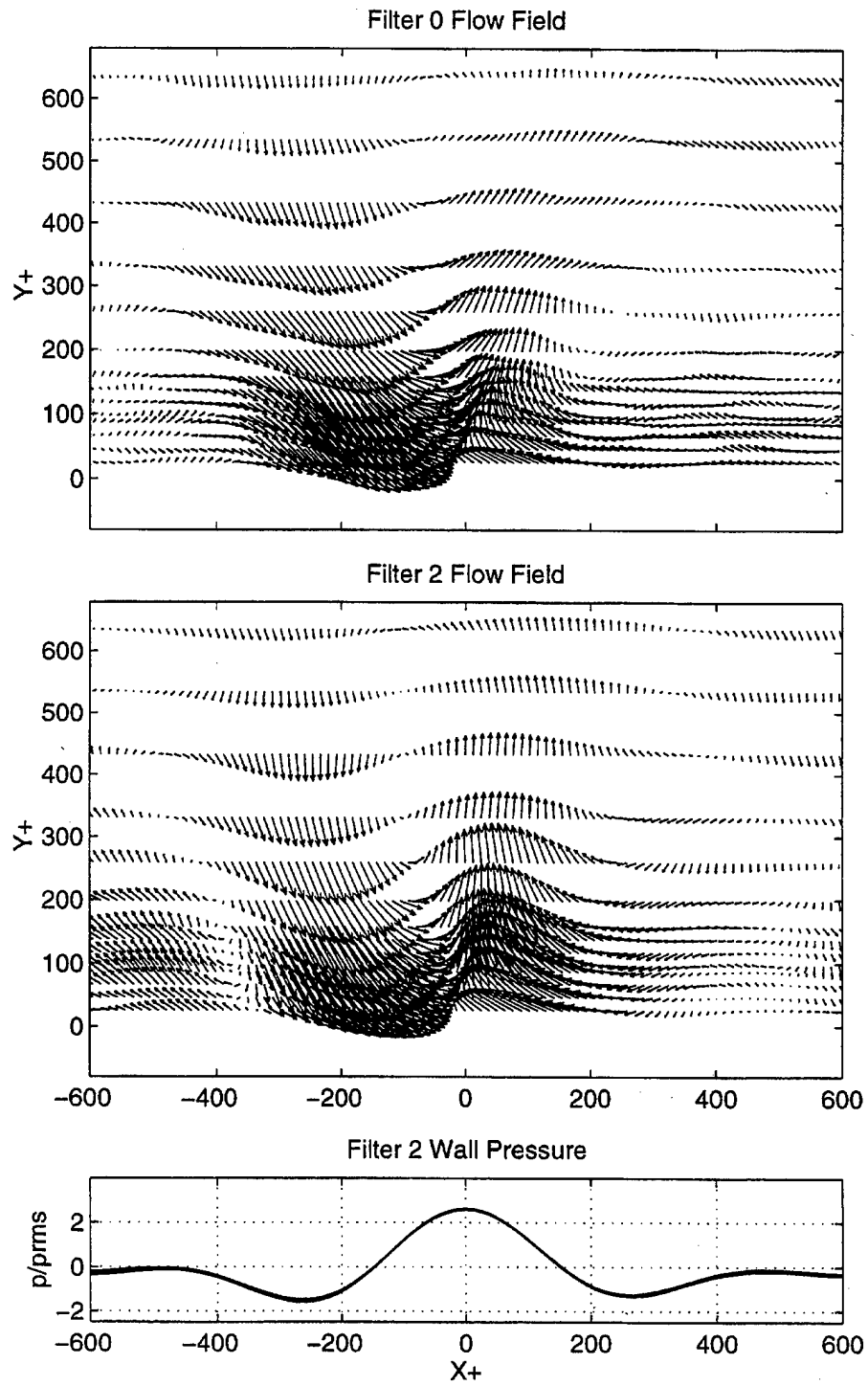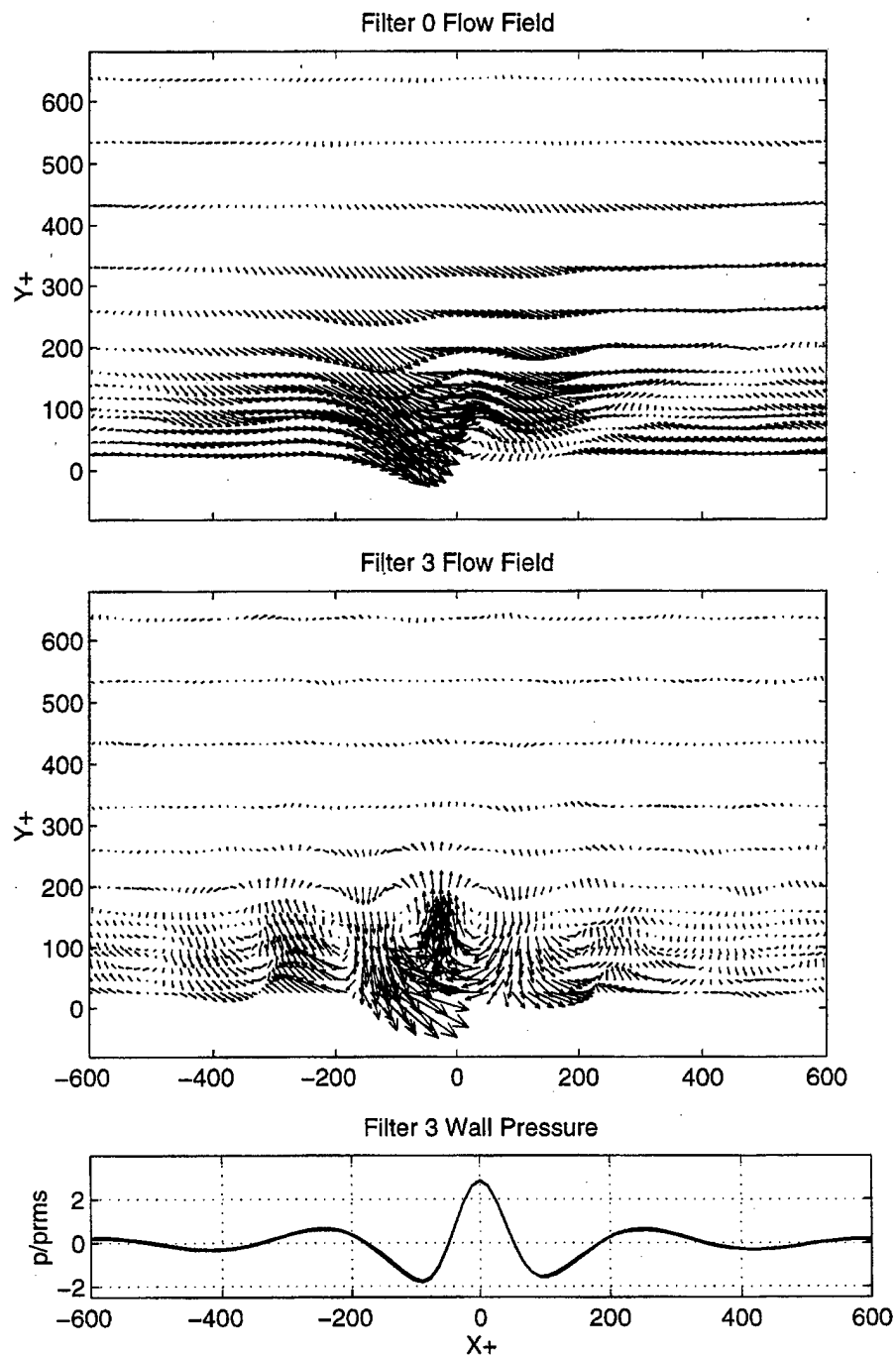
Figure 5.21: Taylor plot of unfiltered and filter 3 flow fields conditionally sampled on filter 3 positive peak wall pressure events
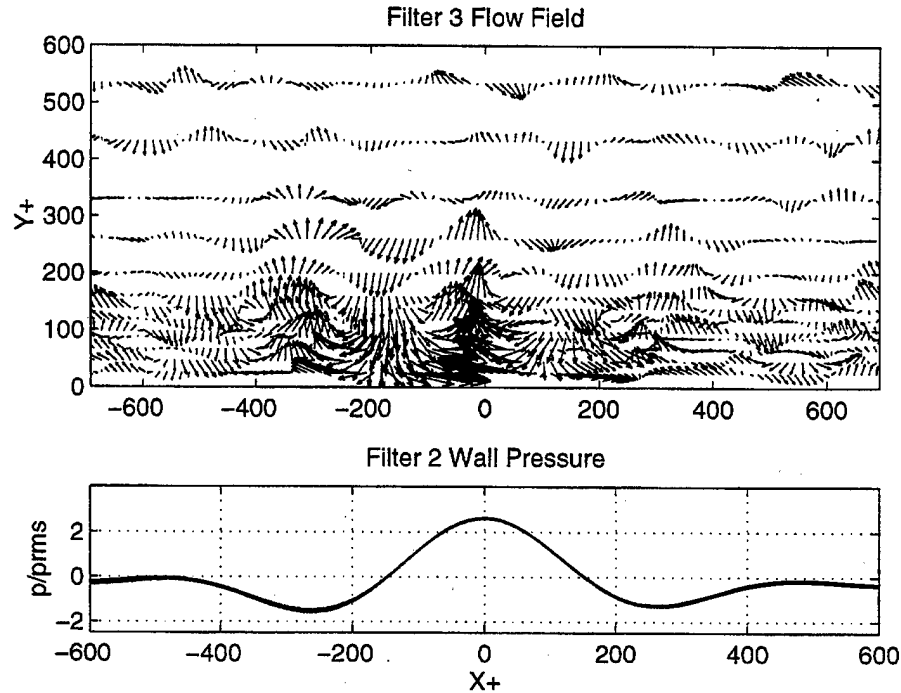
Figure 5.22: Taylor plot of filter 3 flow field conditionally sampled on filter 2 positive peak wall pressure events

to the inclusion of the high frequency velocity signals associated with every filter 2 peak event. There are, however, obvious regions of organized activity, primarily ejection and sweep type motions depicted in these data. So although not all filter 2 peak events are accompanied by high frequency turbulent activity, enough of them are to produce the patterns shown in figure 5.22. The ensemble averaged filter 2 wall pressure signature is shown in this figure to illustrate the difference in scale of the filter 3 motions and the filter 2 wall pressure events on which they are sampled.

5.3   Summary of Findings

In Chapter 4, the space-time characteristics of wall pressure events were examined with an array of pressure transducers. The wall pressure footprints of large and small scale structures were studied and an attempt was made at tracking the convective

structures using the streamwise array. A correlation between the large and small scale motions was identified.

The purpose of the flow field measurements presented in this chapter was to capture and identify the coherent structures that are the source of the wall pressure signatures identified in Chapter 4. To a large extent, this was accomplished. Furthermore, the conjecture on the correlation between large and small scale turbulent motions was confirmed using both cross-correlation and conditional sampling techniques between wall pressure and velocity measurements. Flow field results were presented for both the streamwise and spanwise measurement grids. These results will be summarized according to the technique employed; spectral, correlation, or conditional sampling.

Wall pressure-velocity **cross-spectral** (coherence) measurements were examined to establish the overall spatial extent of the pressure producing turbulent structures. The measured spatial extent of these structures was demonstrated to be a function of frequency. In general, the lowest frequency band (filter 1) was shown to contain two dominant structures, the δ-scale motions within the boundary layer and the induced irrotational motions observed outside the boundary layer. The δ-scale structures within the boundary layer were characterized by strong pu coherence near the wall and strong pv coherence in the outer boundary layer ($y^+ \approx 700$). Smaller scale structures, isolated by the filter 2 band, and the near-wall structures, isolated by the filter 3 band, exhibited similar features to the δ-scale motions. These trends included a strong u component near the wall coupled with a strong v component farther from the wall.

Cross-correlation measurements between filtered wall pressure and the u and v components of velocity proved to contain significant physical information about the dynamics of the turbulent structures. The findings revealed a consistency in the

features of the motions within the boundary layer. The δ-scale structures isolated by filter 1 as well as the near-wall motions isolated by filter 2 and filter 3 were all characterized by ejection/sweep motions. The phase relationships between the pu and pv correlation contours confirmed that these motions behave like Reynolds stress activities. The inclination and convective features of these structures were also demonstrated. The smaller scale motions identified by filters 2 and 3 were shown to contain multiple vortical components. Similarly, spanwise correlation contours revealed streamwise secondary motions associated with periods of strong near wall shear stress (large $-u$).

A more practical finding from these measurements was the realization that unfiltered pressure-velocity correlation measurements are dominated almost exclusively by the large scale (filter 1) irrotational and δ-scale motions. The δ-scale motions appear to globally represent features of the active structures but tend to mask the details of the (high frequency) near-wall structures. To examine the features of the small scale, near-wall turbulent activity, both scales must be removed from the turbulent signals prior to cross-correlation measurement.

Conditional sampling results best illustrated the flow field associated with large and small scale wall pressure events. Both the instantaneous flow mapping technique and the Taylor plotting method were shown to have their own advantages. Flow field results from both techniques were consistent with each other and the fine resolution allowed by the Taylor method proved essential in resolving the details of the small scale motions. Both techniques confirm the ejection/sweep motions associated with the occurence of wall pressure events. Ejection motions corresponded to positive wall pressure peaks and sweeps corresponded to negative pressure peaks for all scales of motion. Furthermore, all ejection motions were shown to be preceded by regions of strong near-wall, negative shear stress, confirming the results of the

correlation contours.

By comparing the filtered versus unfiltered flow fields associated with peak wall pressure events, a definitive structural pattern in the results was observed within the boundary layer. The large scale motions associated with filtered wall pressure events all display ejection/sweep type motions in the inner layer of the boundary layer. When viewing the entire unfiltered flow field associated with these events, the large scale motions appeared to comprise an inclined shear layer. However, by matching the filters of the velocity signals and the wall pressure signals, the vortical or rotational features of these large scale structures were revealed. By sampling the flow field on high frequency (filter 3) wall pressure events, the mapping and Taylor plotting methods both illustrated the correlation between large scale vortical motions (or shear layers) and near-wall, small scale turbulent motions. In general, the passage of the large scale structures correlated with a cluster of several small scale, near-wall burst events.

Chapter 6

SUMMARY AND CONCLUSIONS

The primary objectives of the investigation were first, to identify those organized structures related to turbulent production, to measure the spatial and temporal characteristics of these intermittent activities and to obtain a description of their wall pressure signatures. These objectives were met by acquiring extensive experimental data and performing analyses using a variety of signal processing techniques which included spectral analyses, cross-correlation measurements, and conditional sampling. These techniques were applied to four databases of simultaneously obtained wall pressure and velocity measurements.

The first two experiments (Chapter 4) consisted exclusively of wall pressure measurements from a streamwise and spanwise array of pressure transducers. In the next two experiments (Chapter 5), simultaneous velocity and wall pressure measurements were obtained to map the streamwise and spanwise flow fields associated with wall pressure events. By band-pass filtering the pressure and velocity signals and comparing the results of correlation and conditional sampling for the respective filters, a statistical relationship between large and small scale turbulent structures and their wall pressure signatures was obtained. Detailed summaries of the findings from each set of experiments are included at the end of each chapter. These results will be col-

lectively highlighted in Section 6.1. A more global interpretation of the findings will be presented in Section 6.2 in the form of a conceptual model for coherent motions within the turbulent boundary layer. This model is based primarily on the results of the flow field measurements presented in Chapter 5. Finally, a brief discussion of recommended future work is given in Section 6.3.

6.1 Accomplishments and Findings

The first objective, to identify and discriminate between active and passive turbulent structures was an issue at every phase of the investigation. In the first set of experiments, in which only wall pressure measurements were considered, discrimination between active and passive structures was achieved by band-pass filtering the wall pressure signals at frequencies believed to correspond to scales dominated by the irrotational motions (filter 1), large scale organized structures (filter 2) and near-wall turbulent activity (filter 3). Wall pressure activity in the band of high frequencies had been shown by Kammeyer [25] as well as others to be associated with near-wall, small scale Reynolds stress activity. By using a variety of post processing techniques on the wall pressure signals subjected to high (filter 3) and low (filter 2) frequency filtering, a correlation was observed between low and high frequency wall pressure activity. This correlation was the first evidence that the high frequency filter did not locate all organized activities associated with turbulent production, and that large scale structures may be coupled to the near-wall bursting process.

In the second set of experiments where simultaneous velocity and wall pressure measurements were obtained, the distinction between active and passive turbulent structures was more definitive. In general, it was determined that the discrimination between active and passive turbulent structures could be achieved by filtering the induced irrotational motions from the large amplitude wall pressure activity. Thus,

the flow structures observed by filter 2 and filter 3 wall pressure events represent the large scale and small scale active motions, respectively. By observing the phase relationship between u and v for Reynolds stress activity in the pressure-velocity cross-correlation results for these active motions, evidence of large scale turbulent producing structures within the boundary layer was confirmed. Large scale vortical structures which exhibited Q2/Q4, ejection/sweep-type motions were also observed in the conditional sampling of the wall pressure events. Actual ensemble averaged flow field maps of pressure producing structures showed the classic ejection/sweep characteristics for both large scale outer motions as well as small scale, near-wall motions.

Tracking the active flow structures with a streamwise transducer array was also attempted. By examining the streamwise wall pressure database with the peak event tracking algorithm, many subtle features of the wall pressure field were discovered. Low frequency (filter 2) peak events were successfully tracked across the length of the array. The flow field analyses of the motions associated with these events showed them to exhibit 'active' features as well as to be correlated with near-wall, small scale structures. A high level of confidence was obtained that these turbulent structures could indeed be tracked with an array of pressure transducers. The tracking experiments also identified the need for a more sophisticated cluster detection and tracking algorithm, such as one which employs the VITA technique on wall pressure in order to track higher frequency (filter 3) activity. Filtering the wall pressure signals (filter 2) prior to tracking the events was paramount to the success of the algorithm. The application of a short time VITA detection scheme could possibly circumvent the need for filtering.

The distinct features of the 'total' wall pressure footprint of the small and large scale turbulent producing structures are not easily defined. Based on the results

of this investigation, it is clear that a simple characteristic signature of a turbulent producing structure is not feasible. A hierarchy of structures that induce wall pressure signatures exists within and outside of the boundary layer. For the purposes of this investigation, the structures may be considered active if the trajectory of the motions within the structure exhibit Q2/Q4 patterns. In general, the ensemble averaged flow field associated with both high (filter 3) and low (filter 2) frequency wall pressure events exhibit these Reynolds stress characteristics. Although dominant Reynolds stress production has been historically found to occur near the wall, the large scale structures across the boundary layer exhibit similar Q2/Q4 motions and, more importantly, appear to be coupled to the near wall burst events. Many models of organized motions suggest this relationship [29, 50].

Examination of the wall pressure time records, as well as correlation and conditional sampling results, revealed a temporal relationship between large scale motions across the boundary layer and small scale, near-wall turbulent production activity. Given the scale of a structure, the wall pressure signature of that structure, as seen in a pressure signal filtered to isolate that scale, is characterized by a cluster of positive and negative peaks which correspond to ejection and sweep motions, respectively. On average, the near-wall, small scale motions are characterized by a large number of peaks within a cluster. The instantaneous spatial extent of the footprint is also proportional to the scale of the structure, however, because the large and small scale structures appear to convect together, the total spatial influence of the large and small scale motions are similar.

From a turbulence control standpoint, the results of this investigation are promising. Since the focus of any active control technique would most likely be to affect the near-wall, small scale production motions, the findings associated with these scales are of primary interest. The occurrence of these motions in clusters (best visible

in a filtered time record) indicates the advantage of a VITA type detection criteria. Since these motions were also shown to occur simultaneously with large scale, inclined vortical structures or shear layers, the possibility is raised of an early warning mechanism based on the detection of large scale motions. These large scale motions were successfully tracked in this investigation using conventional wall pressure transducers.

6.2 Conceptual Model of Coherent Motions

Of the eight categories of coherent motions proposed by Kline and Robinson [29] and summarized in Chapter 1, evidence of all but the first (low speed streaks) were found in the conditionally averaged flow field measurements. An idealized model of these structures as well as their wall pressure footprints are shown in figure 6.1. The regions of the flow field which represent these motions are labeled 2 through 8 in figure 6.1a. Furthermore, some of the structures which would be isolated by filters 1, 2, and 3 are also labeled. A crude example of the wall pressure signal subject to the same filters is shown in figure 6.1b. The primary features of this model require some explanation.

Motions 2 and 3 from Kline and Robinson's list (lift-up and ejection of near-wall fluid and the subsequent sweep) are indicated near the wall. Spanwise vortical structures (ω_z) of varying scale (motion 4) are shown throughout the boundary layer region. A sloped near wall shear layer with high spanwise vorticity (motion 5) is indicated by the dashed line above the cluster of small scale structures. A splat motion (motion 6) is shown as the near wall effect of incoming fluid from two adjacent, large scale counter-rotating vortical structures. A large scale (δ-scale) motion capped by the turbulent / non-turbulent interface (motion 7) is indicated along with the large scale shear layer back of this motion (motion 8).
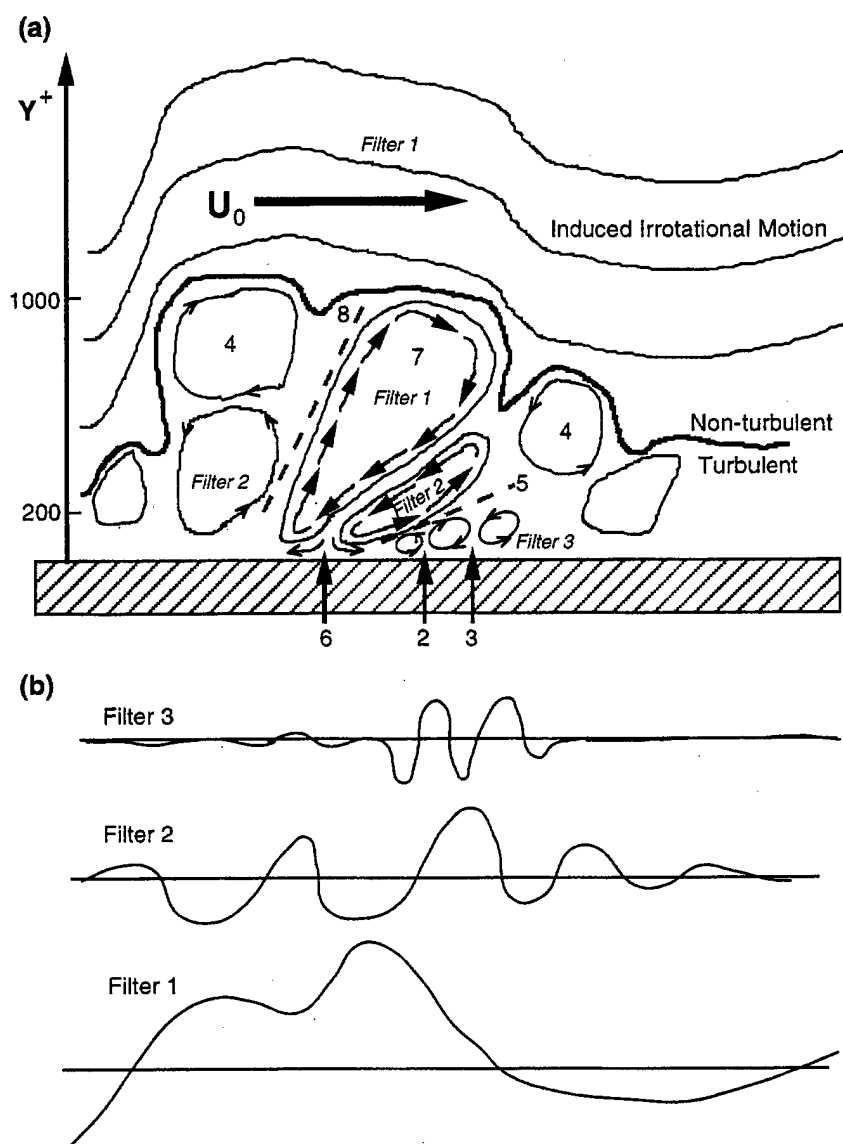
Figure 6.1: Conceptual model of observed motions associated with large amplitude wall pressure events, (a) idealized flow field, (b) filtered wall pressure signals

The shear layers indicated by dashed lines in figure 6.1 were included to illustrate one of the principal findings in this investigation. That is, large and small scale shear layers reported by other investigators are most likely to be artifacts of the interaction between two or more vortical structures. They appear in the unfiltered conditionally averaged flow field measurements because they are correlated with large irrotational motions as well as small scale turbulent activity. It is also believed that the vortical motions from which the shear layers are derived can be revealed in the ensemble average flow field by filtering the velocity and wall pressure signals at matched frequencies.

Another noteworthy finding from this investigation is illustrated in figure 6.1. Based primarily on the analysis of wall pressure time records from the streamwise array, it was determined that while high frequency (filter 3) activity appeared often to be accompanied by low frequency (filter 2) fluctuations, many low frequency peak events appeared alone. So in figure 6.1a, some filter 2 scale structures are shown convecting without the presence of small scale near-wall structures.

The wall pressure activity associated with each of the structures depicted in figure 6.1a are shown in figure 6.1b. The clustering features of the filter 3 and filter 2 scale motions are illustrated along with the wave-like behavior of the filter 1 signal which contains footprints of the δ-scale vortical structures within the boundary layer as well as the footprint of the induced irrotational motions outside the boundary layer.

The physical features of organized motions proposed by Kline and Robinson [29] and reviewed in Chapter 1 warrant further examination. Kline [28] presented a summary of boundary layer structures as observed from low Reynolds number direct numerical simulation (DNS) studies. He concluded that two types of vortical structures are defined as "central" structures:

1. Inner Layer: tilted streamwise (Legs)

2. Outer Layer: transverse (Heads)

and that the two forms appear to overlap in the log-law region. Hairpin or horseshoe vortices do appear but are rare compared to heads and legs. He further comments on the relationship between the turbulent production process (Q2 and Q4 motions) and the appearance of heads and legs.

The three dimensional characteristics of the motions observed in this investigation could not be determined from the data collected. However, the model for coherent motions proposed in figure 6.1 would not be inconsistent with the hierarchy of legs and heads discussed by Kline. These are shown in figure 6.2. In Robinson's model, the buffer layer ($y^+ \leq 30$) contains primarily the streamwise legs of the hairpin-like structures which are formed by the lifting and stretching of low speed streaks. The log-law region ($30 \leq y^+ \leq 200$) is populated by a mixture of components (heads and legs) whereas the outer-boundary layer, or wake region ($y^+ \geq 200$) is dominated by the large scale remnants of the near wall production process (heads).

This highly idealized model would be difficult to verify experimentally for the high Reynolds number flow pursued in this study, however, its general features are consistent with the observations made in this investigation. The near-wall vortical motions observed in this investigation, which are responsible for a large portion of the RMS wall pressure field, are undoubtedly related to turbulent production. The dynamical relationship between large scale heads and small scale legs in the hairpin model may explain the correlation between large and small scale motions measured in this investigation. However, three dimensional resolution of the scales at which this process takes place would require experimental techniques beyond the scope of this investigation.
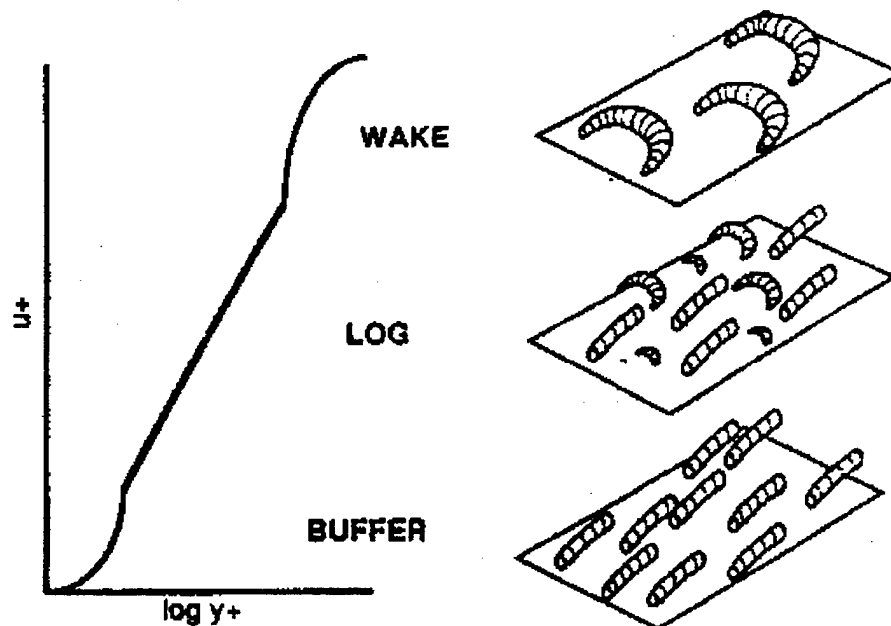
Figure 6.2: Idealized schematic of vortical structure populations in different regions of the turbulent boundary layer, from Robinson (1990)

6.3 Recommendations for Future Work

One of the more important findings of this investigation was the clustering of activity in the high frequency wall pressure signals. Although simple peak detection yielded promising results on both wall pressure event tracking and flow field visualization (conditional sampling), a more sophisticated cluster detection and tracking scheme would be desirable. This scheme could be based on the VITA technique which was demonstrated here to successfully capture the wall pressure activity associated with large and small scale coherent structures in the boundary layer. It would also be interesting to apply such a detection method to turbulent signals which have been subjected to a wavelet based filter, customized to capture the scales of active motions identified in this investigation with filters 2 and 3.

Many coherent structures were identified in this investigation in the flow fields

conditionally averaged on peak wall pressure events. The cluster detection and tracking scheme could also be used with the streamwise wall pressure array to establish a more definitive criteria for conditional sampling flow variables. The flow field associated exclusively with convecting clusters of high and low frequency wall pressure activity may yield more detailed physical characteristics of the near-wall active motions. In this respect, any tracking scheme developed for use in an active turbulence control process could be evaluated using the database collected in this investigation.

In general, there are many potential uses for the database established in this work, including testing alternative signal processing techniques or filtering schemes. It may also be worthwhile for investigators, whose findings based on direct numerical simulation have been cited throughout this work, to attempt to numerically duplicate the measurements made in this investigation. This type of study could qualify many of the physical interpretations made from the experimental measurements presented.

Appendix A

TRANSDUCER QUALIFICATION

A comparative study was performed early in the investigation to determine the feasibility of using Endevco pressure transducers (described in detail in Chapter 2) as elements of an array for tracking large amplitude wall pressure events. All prior wall pressure studies conducted in the Catholic University Low Noise Flow Facility employed Bruel & Kjaer (B&K), condenser-type microphones. The cost and size of the smallest available B&K microphones were prohibitive for a multi-element array. In this appendix, the results of the comparative study are presented.

The performance of the Endevco Transducers will be compared to the B&K microphones according to the following categories:

1. Sample time records.

2. Noise floor.

3. Wall pressure spectra for equilibrium flow.

    (a) Signal to noise ratio (f).

    (b) Broad-band frequency response.

4. Large amplitude event statistics.

(a) Ensemble averaged event shapes.

(b) Number of events detected.

Wall pressure data were acquired from both the Endevco and B&K trandsucers using the experimental setup illustrated in figure 2.4. Figures A.1a and b show sample time records from a B&K microphone and an Endevco 8507C-2 transducer. In each figure, raw, high-pass filtered (100 Hz), and band-pass filtered (filter 0) signals are shown. The removal of the DC component by high pass filtering is evident in both signals. The most noticeable difference between the B&K and Endevco signals is the high frequency "choppiness" of the Endevco time record. This very high frequency component of the Endevco signal is dominated by electrical noise. By band pass filtering the Endevco signal at 100 Hz and 5 kHz, the noise component is effectively removed and the overall features of the original signal are retained. It is clear from these data that the removal of high frequency noise from the Endevco signal is necessary before peak detection or VITA techniques can be applied. Details of the high-frequency noise floor will be further illustrated next.

The reason for the high frequency noise contamination is illustrated in figure A.2 where the noise floors (wall pressure spectra at $U_0=0$ m/s) are shown for both the Endevco and B&K sensors. While both systems contain strong 60 cycle harmonics, the noise floor of the B&K system at 10 kHz is over 20 dB lower than the Endevco system. The effects of this noise floor are shown as signal to noise for $U_0=50$ m/s in figure A.3. The broadband S/N ratio for the B&K system is nominally 30 dB while that for the Endevco system is just over 20 dB. The frequency at which the noise floor meets the turbulent boundary layer signal is approximately 10 kHz for the B&K microphones and 6 kHz for the Endevco system. The upper cutoff frequency for filter 0 was chosen as 5 kHz based on a minimum S/N ratio of 3 dB at that frequency. It should be noted that the sensitivities of the B&K and Endevco transducers were
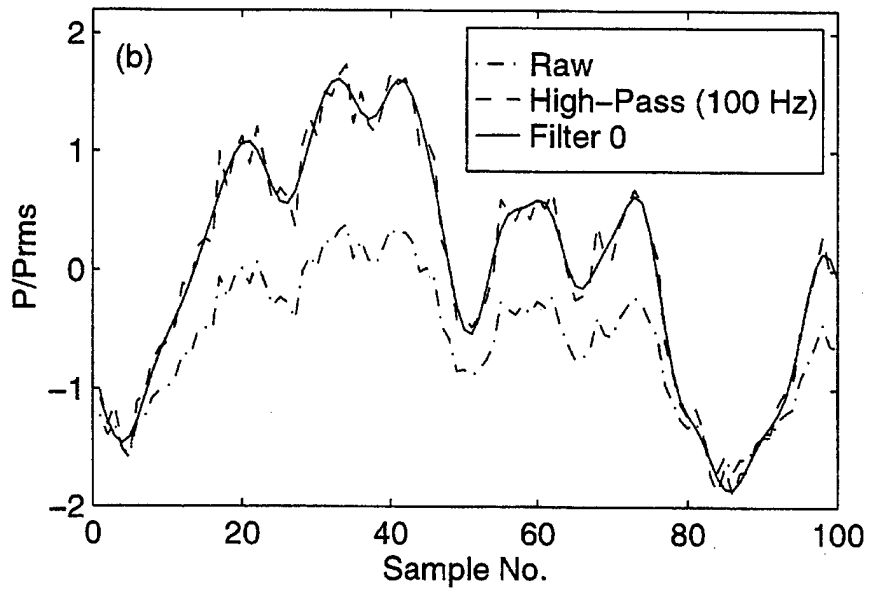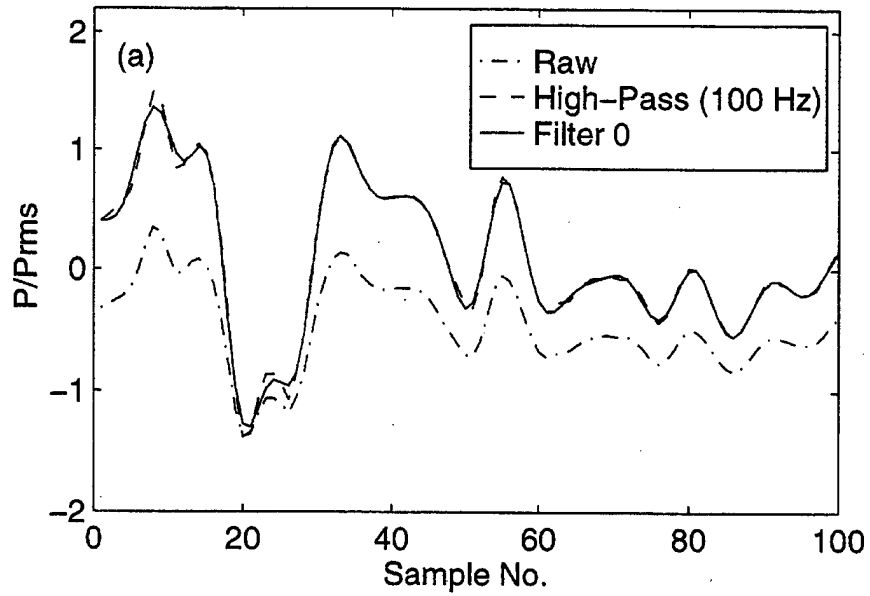
Figure A.1: Sample raw and filtered wall pressure time records (U0=15 m/s), (a) B&K 1/8-in. condenser type microphone, (b) Endevco 8507C-2 piezoresistive transducer
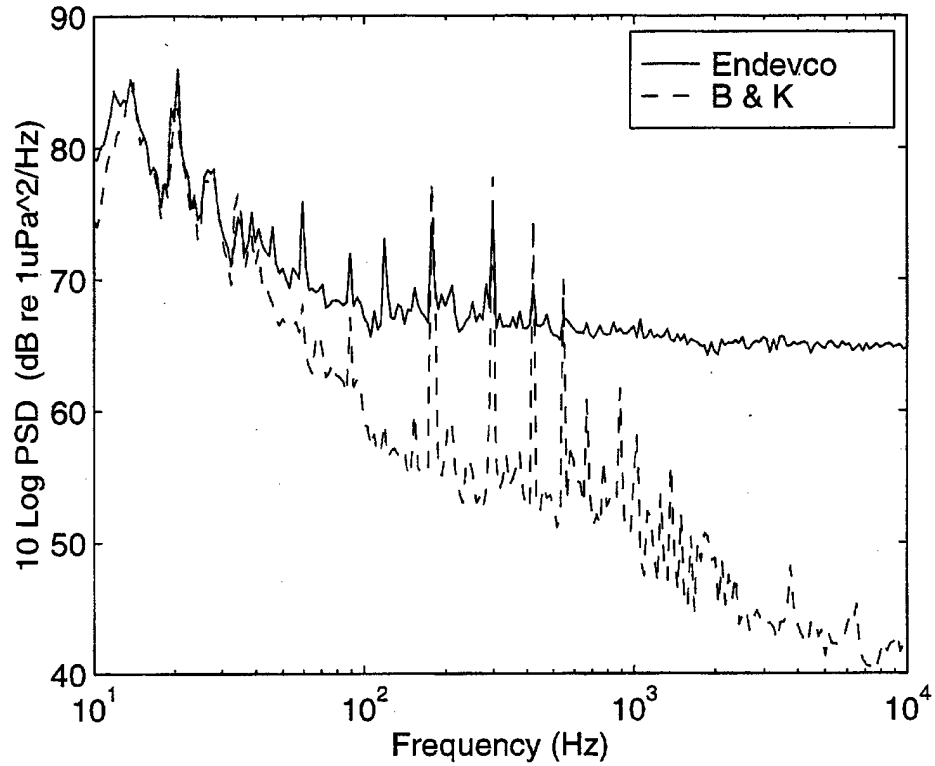
Figure A.2: Comparison of wall pressure sensor noise floors

approximately 0.77 mV/Pa and 0.02 mV/Pa respectively.

The wall pressure spectra shown in figure A.4 are the result of ensemble averaging the six Endevco spectra (solid line) and two B&K spectra (dashed line). These data were obtained at U_0=50 m/s from a spanwise array (6 Endevco sensors and 2 B&K sensors). The Endevco spectra collapsed on each other to within 1.5 dB and the B&K spectra collapsed to within 1 dB. Below 30 Hz, facility noise clearly dominates both signals. Out to approximately 1000 Hz, both sensors have essentially the same response. Above 1000 Hz, the roll-off of the Endevco sensors is slightly steeper and the noise floor is reached at approximately 6 kHz. The B&K signal is essentially noise free out to 10 kHz. The steeper high frequency roll-off for the Endevco sensors is believed to be due to a combination of two dominant factors. First, the sensing diameter of the Endevco sensors is known to be slightly larger than that of the B&K
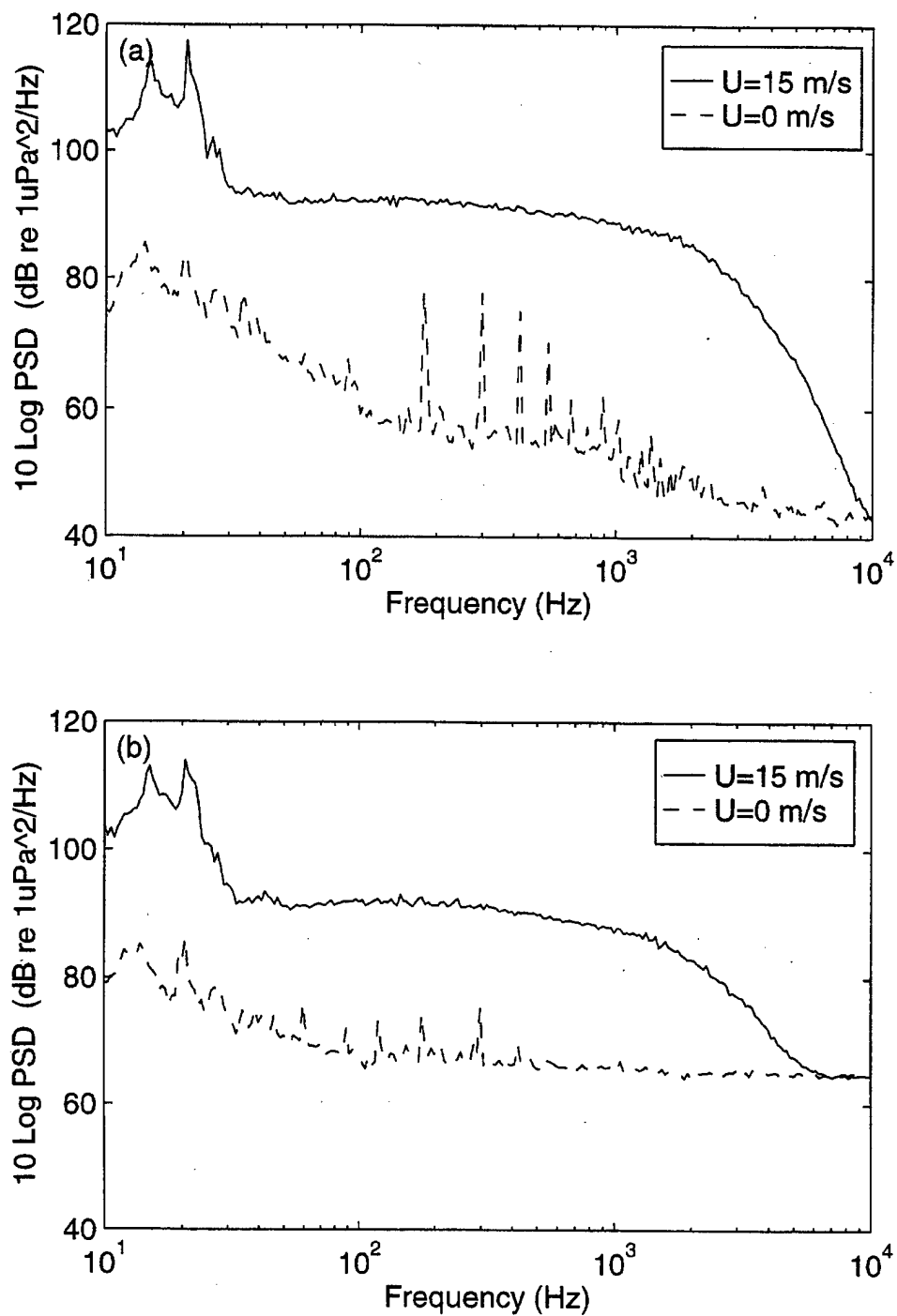
Figure A.3: Signal to noise ratios of wall pressure sensors (U0=15 m/s), (a) B&K 1/8-in condenser type microphone, (b) Endevco 8507C-2 piezoresistive transducer
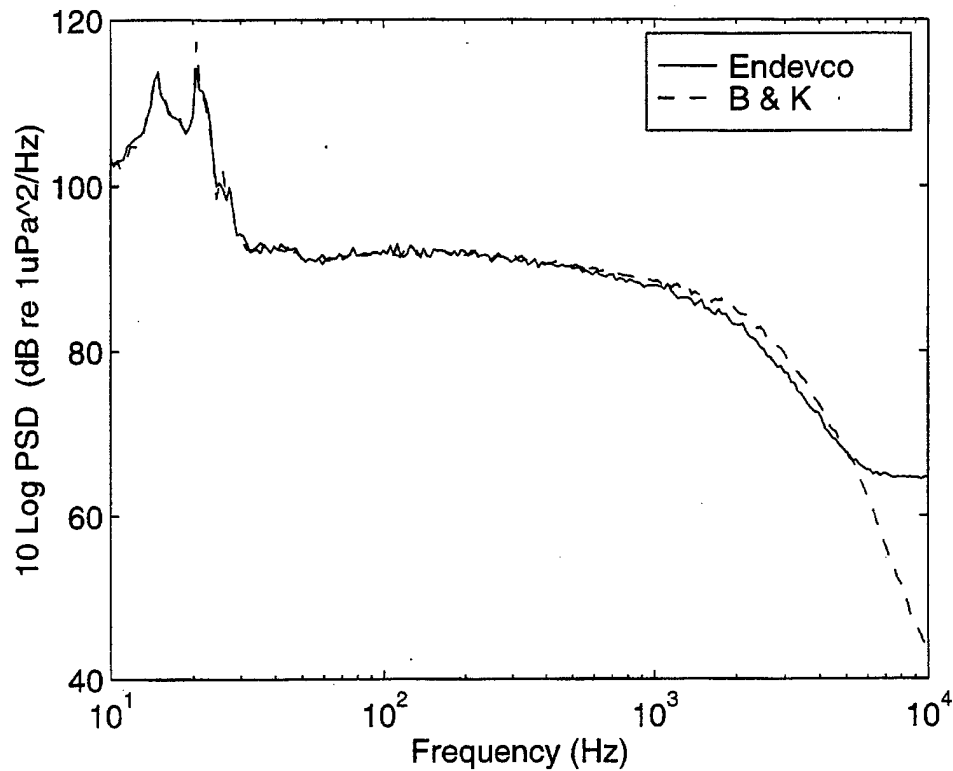
Figure A.4: Comparison of mean wall pressure spectra at U0=15 m/s

pinhole microphones ($d^+_{B\&K}$=31, $d^+_{Endevco}$=39) which would result in attanuation of higher frequency pressure fluctuations. Secondly, the frequency response of the Endevco transducers may not be as flat as claimed by the manufacturer (white noise response data were not available).

Peak event statistics were computed for each transducer in the qualification test (6 Endevco and 2 B&K sensors). Events were compiled for each transducer at thresholds of $k = \pm$ 1, 2, and 3 for high pass filtered (100 Hz) and band pass filtered (filter 0) wall pressure signals. The ensemble average event shapes for k=+3 for the Endevco sensors were then averaged for the 6 transducers. The resulting event shape along with the equivalent shape for the B&K microphones for the filter 0 wall pressure signals are shown in figure A.5. The event shapes from the B&K and Endevco sensors are almost indistinguishable.. The only subtle difference is the
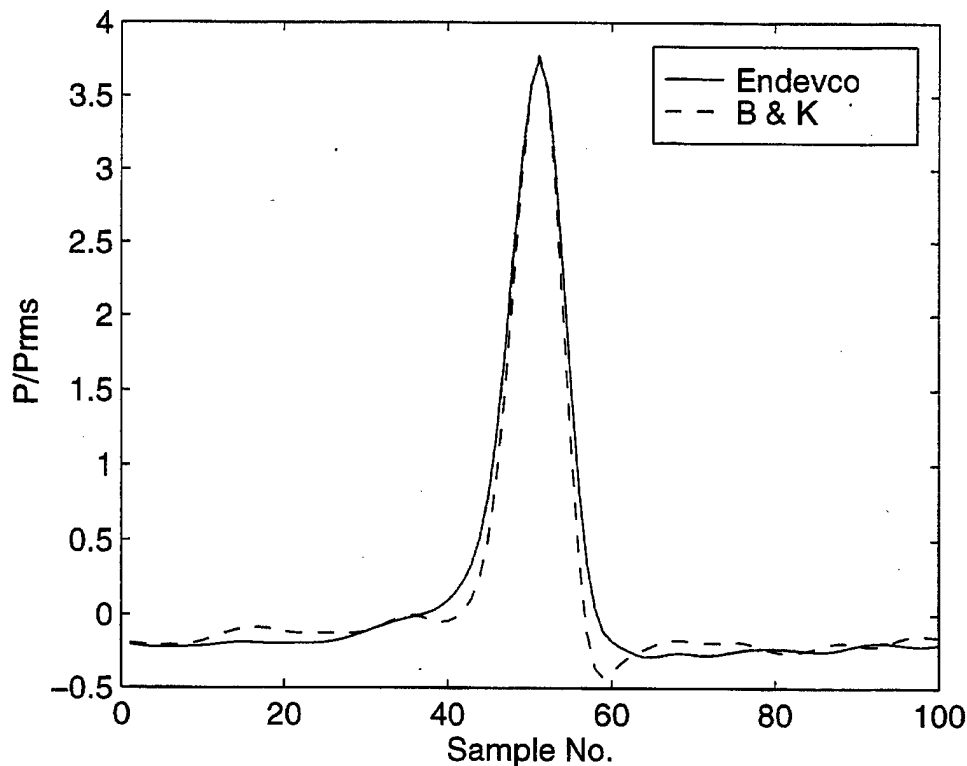
Figure A.5: Comparison of average positive peak event shapes (k=3) for wall pressure signals subjected to filter 0 (U0=15 m/s)

slightly more detailed over shoot of the B&K event shape. This can be attributed to the slightly better high frequency response of the B&K system. However, from the standpoint of peak event shapes, by applying filter 0 to the Endevco signal, the mean features of the wall pressure signal seen by both transducers is essentially the same.

The total number of peak events detected in the high-pass filtered 10 second time records of the B&K and Endevco wall pressure signals are given in table A.1 for each transducer at thresholds values of $k = \pm$ 1, 2, and 3. The event statistics for the filter 0 signals are given in table A.2 to illustrate the effect of the 5 kHz cutoff frequency on peak event detection.

The number of events detected in the high-pass filtered data given in table A.1

Table A.1: Total peak events detected for high pass filtered B&K and Endevco wall pressure signals

Sensor	k=±1	k=±2	k=±3
B&K #1	10442	3313	928
B&K #2	11136	3442	914
Endevco #1	10862	3191	834
Endevco #2	11449	3413	831
Endevco #3	11391	3478	845
Endevco #4	10834	3215	830
Endevco #5	11635	3493	840
Endevco #6	11097	3244	795

Table A.2: Total peak events detected for band-pass (filter 0) B&K and Endevco wall pressure signals

Sensor	k=±1	k=±2	k=±3
B&K #1	10317	3248	908
B&K #2	10965	3387	879
Endevco #1	9520	2803	769
Endevco #2	9853	2989	738
Endevco #3	9812	3028	775
Endevco #4	9708	2918	771
Endevco #5	9877	3013	740
Endevco #6	9583	2839	721

shows a consistency between the B&K and the Endevco results for threshold values of $k = 1$ and 2. Slightly more large amplitude events ($k=3$) are detected by the B&K sensors. This effect is most likely due to the steeper high frequency roll-off for the Endevco sensors. In fact, if not for the high frequency noise contaminating the high pass filtered Endevco signal (see figure A.1b), this effect would probably more dramatic. The results in table A.2 confirm this conjecture. By removing the high frequency noise component from the Endevco signals, the number of peak events detected is greatly reduced for all threshold values. Whereas the number of events detected by the B&K sensors is essentially unchanged. The high frequency roll-off of the Endevco sensors results in nominally 10% fewer peak events detected.

Other statistics such as percent of the time record occupied by peak events, percent contribution of the events to RMS pressure, average time between events and the average duration of events was computed for all sensors subject to high-pass and band-pass filtering. This extensive list of statistics shows a general consistency between the B&K sensors and the Endevco transducers and is therefore not presented here.

Since the time between peaks seen in signals from various wall pressure sensors was used extensively in this investigation to characterize convection velocity and other phase relationships, it was important to verify that the sensors in the array were synchronized. The array containing the six Endevco transducers and the two B&K microphones was subjected to an impulse acoustic signal while the signals were being sampled. The response of the sensors (not shown) indicate that the Endevco sensors appear to be synchronized to within .03 msec (0.68 viscous time units).

Based on the event statistics presented in this appendix, as well as on the higher order statistics not presented, the Endevco sensors were determined to be adequate for this investigation. Similarly, for the frequency range of interest for the wall pres-

sure measurements (100 Hz to 5 kHz) the Endevco 8507C-2 transducer systems were determined to have an adequate signal to noise ratio at tunnel speeds of approximately 15 m/s (50 ft/s).

Bibliography

[1] R. J. Adrian, P. Moin, and R. D. Moser. Stochastic estimation of conditional eddies in turbulent channel flow. In *Proc. 1987 Summer Program Cent. Turb. Res.*, pages 7–19. Center for Turbulence Research, Stanford, CA, 1987.

[2] J. A. Astolfi and B. E. Forestier. Flow noise associated with near-wall turbulence structure. In Farabee, Keith, and Lueptow, editors, *Flow Noise Modeling, Measurement, and Control*, number NCA 15/FED 168, pages 1–11. ASME, 1993.

[3] J. S. Bendat and A. G. Piersol. *Engineering Applications of Correlation and Spectral Analysis*. Wiley-Interscience, 1980.

[4] R. F. Blackwelder and H. Eckelmann. Streamwise vortices associated with the bursting phenomenon. *J. Fluid Mech.*, 94:577–594, 1979.

[5] R. F. Blackwelder and R. E. Kaplan. On the wall structure of the turbulent boundary layer. *J. Fluid Mech.*, 76:89–112, 1976.

[6] W. K. Blake. Turbulent boundary layer wall pressure fluctuations on smooth and rough walls. *J. Fluid Mech.*, 44 Part 4:637–660, 1970.

[7] W. K. Blake. Aero-hydroacoustics for ships. Technical Report DTNSRDC Report 84/010, David Taylor Naval Ship Research and Development Center, Bethesda, MD, 1984.

[8] T. F. Brooks and T .H. Hodgson. Trailing edge noise prediction from measured surface pressures. *J. Sound and Vib.*, 78 No. 1:69–117, 1981.

[9] M. K. Bull. Wall-pressure fluctuations associated with subsonic turbulent boundary layer flow. *J. Fluid Mech*, 28:719–754, 1967.

[10] K. J. Bullock, R. E. Cooper, and F. H. Abernathy. Structural similarity in radial correlations and spectra of longitudinal velocity fluctuations in pipe flow. *J. Fluid Mech.*, 88:585–608, 1978.

[11] K. S. Choi. Turbulent drag reduction strategies. In Choi, Prasad, and Truong, editors, *Emerging Techniques in Drag Reduction*, pages 77–100. Mechanical Engineering Publications Ltd., 1996.

[12] F. H. Clauser. The turbulent boundary layer. In *Advances in Applied Mechanics*, volume 4, pages 2–51. Academic Press, 1956.

[13] A. Dinkelacker. Do tornado-like vortices play a role in the turbulent mixing process? In *Proc. IUTAM/ICHMT Symp.* Hemisphere, 1982.

[14] Endevco. *Piezoresistive Pressure Transducers, Instruction Manual, Rev A*, 1990.

[15] R. E. Falco. New results, a review and synthesis of the mechanism of turbulence production in boundary layers and its modification. *AIAA Paper No. 83-0377*, 1983.

[16] T. M. Farabee. An experimental investigation of wall pressure fluctuations beneath non-equilibrium turbulent flows. Technical Report DTNSRDC-86/047, David Taylor Naval Ship Research and Development Center, Bethesda, Maryland 20084-5000, 1986.

[17] T. M. Farabee and M. J. Casarella. Spectral features of wall pressure fluctuations beneath turbulent boundary layers. *Phys. Fluids A*, 3(10):2410–2420, 1991.

[18] H. E. Fiedler. Coherent structures. In *Advances in Turbulence*, pages 320–336. Springer-Verlag, 1986.

[19] K. Hijikata, Y. Suzuki, and K. Iwana. Flow visualization by velocity pressure cross-correlation. *J. Fluids Engineering*, 118:486–493, 1996.

[20] J. O. Hinze. *Turbulence*. McGraw Hill, New York, 1975.

[21] A. Hussain. Coherent structures—reality and myth. *Phys. Fluids*, 26(10):2816–2850, 1983.

[22] S. Jayasundera, M. Casarella, and S. Russell. Identification of coherent motions using wall pressure signatures. Technical Report Progress Rept. to Office of Naval Research, Catholic University of America, Washington, DC, 1996.

[23] J. Jimenez, P. Moin, R. D. Moser, and L. R. Keefe. Ejection mechanisms in the sublayer of a turbulent channel. In *Proc. 1987 Summer Program Cent. Turb. Res.*, pages 37–47. Center for Turbulence Research, Stanford, CA, 1987.

[24] A. V. Johansson, J. Her, and J. H. Haritonidis. On the generation of high-amplitude wall pressure peaks in turbulent boundary layers and spots. *J. Fluid Mech.*, 175:119–142, 1987.

[25] M. Kammeyer. *An Experimental Investigation of Organized Turbulent Motions and Wall-Pressure Fluctuations in Complex Flows*. PhD thesis, The Catholic University of America, 1995.

[26] C. C. Karangelen. *Temporal and Spectral Features of Wall Pressure Fluctuations Beneath a Turbulent Boundary Layer*. PhD thesis, The Catholic University of America, 1991.

[27] J. Kim. On the structure of pressure fluctuations in simulated turbulent channel flow. *J. Fluid Mech.*, 205:421–451, 1989.

[28] S. J. Kline. Boundary layer structure - a summary. In *Turbulence Research - Joint AFOSR/ONR Grantee and Contractors Meeting*, pages 157–173. Illinois Institute of Technology, Fluid Dynamics Research Center, 1992.

[29] S. J. Kline and S. K. Robinson. Quasi-coherent structures in the turbulent boundary layer. Part I: Status report on a community-wide summary of the data. In Kline and Afgan, editors, *Near-Wall Turbulence: Proceedings of the 1988 Zoran Zaric Memorial Conference*, pages 200–217. Hemisphere, 1990.

[30] Y. Kobashi and M. Ichijo. Wall pressure and its relation to turbulent structure of a boundary layer. *Experiments in Fluids*, 4:49–55, 1986.

[31] L. S. G. Kovasznay. The turbulent boundary layer. *Annu. Rev. Fluid Mech.*, 2:95–112, 1970.

[32] T. P. Krauss, L. Shure, and J. N. Little. *Signal Processing TOOLBOX for Use with MATLAB*. The MathWorks, Inc. Natick, Mass., 1994.

[33] F. Laadhari, R. Morel, and E. Alcaraz. Combined visualization and measurements in transitional boundary layers. *Eur. J. Mech., B/Fluids*, 13 No. 4:473–489, 1994.

[34] J. Laufer. New trends in experimental turbulence research. *Annu. Rev. Fluid Mech.*, 7:307–326, 1975.

[35] Y. Nagano and M. Tagawa. Coherent motions and heat transfer in a wall turbulent shear flow. *J. Fluid Mech.*, 305:127–157, 1995.

[36] A. M. Naguib and C. E. Wark. An investigation of wall-layer dynamics using a combined temporal filtering and correlation technique. *J. Fluid Mech.*, 243:541–560, 1992.

[37] N. Narayan and R. Plunkett. Pressure cross spectra in turbulent boundary layers in water. In *NCA Vol 1*, pages 97–103. ASME Winter Annual Meeting, Miami Beach, FL, 1996.

[38] G. R. Offen and S. J. Kline. A proposed model of the bursting process in turbulent boundary layers. *J. Fluid Mech.*, 70:209–228, 1975.

[39] R. L. Panton, A. L. Goleman, R. L. Lowery, and M. M. Reischman. Low-frequency pressure fluctuations in axisymmetric turbulent boundary layers. *J. Fluid Mech.*, 97:299–319, 1980.

[40] P. B. Penafiel. VXI driver for the HP-9000/735 workstation using the HP-E1489I MXIbus controller interface. Technical report, Dept. of Mech. Engineering, The Catholic University of America, Washington, D.C. 20064, 1994.

[41] P. B. Penafiel, M. J. Casarella, and M. E. Kammeyer. Application of wavelet-filtering techniques to intermittent turbulent and wall pressure events, part II — detection of cluster patterns. Technical report, Dept. of Mech. Engineering, The Catholic University of America, Washington, D.C. 20064, 1995.

[42] A. K. Praturi and R. S. Brodkey. A stereoscopic visual study of coherent structures in turbulent shear flow. *J. Fluid Mech.*, 89:251–272, 1978.

[43] S. K. Robinson. *Kinematics of Turbulent Boundary Layer Structure.* PhD thesis, Stanford University, 1990.

[44] S. K. Robinson. Coherent motions in the turbulent boundary layer. *Annu. Rev. Fluid Mech.*, 23:601–639, 1991.

[45] G. Schewe. On the structure and resolution of wall-pressure fluctuations associated with turbulent boundary-layer flow. *J. Fluid Mech.*, 134:311–328, 1983.

[46] S. R. Snarski and R. M. Lueptow. Wall pressure and coherent structures in a turbulent boundary layer on a cylinder in axial flow. *J. Fluid Mech.*, 286:137–171, 1995.

[47] P. R. Spalart. Direct simulation of a turbulent boundary layer up to re=1410. *J. Fluid Mech.*, 187:61–98, 1988.

[48] H. Tennekes and J. L. Lumley. *A First Course in Turbulence.* The MIT Press, 1972.

[49] T. Theodorsen. Mechanism of turbulence. In *Proc. Midwest Conf. Fluid Mech. 2nd*, pages 1–18, 1952.

[50] A. S. W. Thomas and M. K. Bull. On the role of wall-pressure fluctuations in deterministic motions in the turbulent boundary layer. *J. Fluid Mech.*, 128:283–322, 1983.

[51] J. M. Wallace. The vortical structure of bounded turbulent shear flow. *Lect. Notes Phys.*, 235:253–268, 1985.

[52] C. E. Wark and H. M. Nagib. Experimental investigation of coherent structures in turbulent boundary layers. *J. Fluid Mech.*, 230:183–208, 1991.

[53] V. Wilczynksi. *Organized Turbulent Structures and Their Induced Wall Pressure Fluctuations.* PhD thesis, The Catholic University of America, 1992.

[54] W. W. Willmarth and S. S. Lu. Structure of the reynolds stress near the wall. *J. Fluid Mech.*, 55:65–92, 1972.

[55] W. W. Willmarth and B. J. Tu. Structure of turbulence on the boundary layer near the wall. *Phys. Fluids*, 10:134–137, 1967.

[56] Y. Yuan and M. Mokhtarzadeh-Dehghan. A comparison study of conditional-sampling methods used to detect coherent structures in turbulent boundary layers. *Phys. Fluids*, 6(6):2038–2057, 1984.

DISTRIBUTION

Copies   Copies

DoD - CONUS

ATTB CODE 1132 SM DR PB ABRAHAM   1
OFFICE OF NAVAL RESEARCH
800 N QUINCY ST
ARLINGTON VA 22217-5660

ATTB CODE 804 (DR JAMES MENG)   1
NAVAL UNDERSEA WARFARE CENTER
  DIVISION
NEWPORT RI 02841-5047

ATTB CODE 102 (STUART DICKINSON)   1
NAVAL UNDERSEA WARFARE CENTER
  DIVISION
117 HOWELL ST
NEWPORT RI 02841-1708

ATTB CODE 2133 (DR H SCHLOEMER)   1
NAVAL UNDERSEA WARFARE CENTER DET
NEW LONDON CT 06320

ATTB CODE 2133 (DR S SNARSKI)   1
NAVAL UNDERSEA WARFARE CENTER DET
NEW LONDON CT 06320

ATTB CODE 7253 (DR ROBERT HANDLER) 1
NAVAL RESEARCH LABORATORY
4555 OVERLOOK AVE SW
WASHINGTON DC 20375-5343

ATTB CODE 122 (DR KAM NG)   1
OFFICE OF NAVAL RESEARCH
BALLSTON TOWER ONE
800 N QUINCY STREET
ARLINGTON VA 22217-5660

ATTN ONR 333 (DR L P PURTELL)   1
OFFICE OF NAVAL RESEARCH
800 NORTH QUINCY ST
ARLINGTON VA 22217-5660

ATTN ONR 333 (DR EDWIN ROOD)   1
OFFICE OF NAVAL RESEARCH
800 NORTH QUINCY ST
ARLINGTON VA 22217-5660

ATTB CODE 1215 (MR JAMES FEIN)   1
OFFICE OF NAVAL RESEARCH
800 N QUINCY ST
ARLINGTON VA 22217-5660

ATTN DR JAMES MCMICHAEL   1
AFOSR/NA
BOLLING AFB DC 20332

MR GARY JONES   1
ADVANCED RESEARCH PROJECTS AGENCY
3701 NORTH FAIRFAX DRIVE
ARLINGTON VA 22203-1714

NON-DoD
DR LUCIO MAESTRELLO   1
NASA LANGLEY RESEARCH CENTER
MAIL STOP 163
HAMPTON VA 23665

DR S K ROBINSON   1
MS 163
NASA LANGLEY RESEARCH CENTER
HAMPTON VA 23665-5225

PROF AMY ALVING   1
107 ACKERMAN HALL
UNIV OF MINNESOTA
110 UNION ST SE
MINNEAPOLIS MN 55455

DR GAL BERKOOZ   1
MECH AND AERO ENG
238 UPSON HALL
CORNELL UNIVERSITY
ITHACA NY 14853

DR L P BERNAL   1
UNIVERSITY OF MICHIGAN
DEPT OF AERO ENGINEERING
ANN ARBOR MI 48109

DR PETER BERNARD   1
UNIVERSITY OF MARYLAND
DEPT OF MECH ENGINEERING
COLLEGE PARK MD 20742

(1)

DISTRIBUTION (Cont.)

Copies   Copies

PROF DAVID BOGARD   1
UNIVERSITY OF TEXAS
DEPT OF MECHANICAL ENG
ETC 11 5 160
AUSTIN TX 78712-1063

PROF KENNETH BREUER   1
DEPT OF AERO AND ASTRO
MASS INSTITUTE OF TECH
77 MASSACHUSETTS AVE
CAMBRIDGE MA 02139

PROF DAVID BOGER   1
PENN STATE UNIVERSITY
P O BOX 30
STATE COLLEGE PA 16804

DR FREDERICK BROWAND   1
UNIV OF SOUTHERN CALIFORNIA
DEPT OF AERO ENGINEERING
UNIVERSITY PARK
LOS ANGELES CA 90089-1191

DR ALAN BRANDT   1
JOHNS HOPKINS UNIVERSITY
APPLIED PHYSICS LAB
LAUREL MD 20723-6099

DR COURTNEY BURROUGHS   1
APPLIED RESEARCH LAB
PENN STATE UNIVERSITY
P O BOX 30
STATE COLLEGE PA 16804

DR B J CANTWELL   1
DEPT OF AERO & ASTRO
STANFORD UNIVERSITY
STANFORD CA 94305

DR MARIO CASARELLA   1
DEPT OF MECH ENGINEERIN
CATHOLIC UNIVERSITY OF AMERICA
WASHINGTON DC 20064

PROF T CEBECI   1
DEPT OF AERO ENG
CAL STATE UNIV LONG BEACH
1250 BELLFLOWER BLVD
LONG BEACH CA 90840

DR K L CHANDIRAMANI   1
ATLANTIC APPLIED RESEARCH CORP
4 A STREET
BURLINGTON MA 01803

PROF D COLES   1
MS 105-50
CALIFORNIA INSTITUTE OF TECH
PASADENA CA 91125

DR FREDERICK DEMETZ   1
BENDIX OCEANICS DIVISION
15825 ROXFORD ST
SYLMAR CA 91342

DR STEVEN DEUTSCH   1
APPLIED RESEARCH LAB
P O BOX 30
STATE COLLEGE PA 16804

PROF W J DEVENPORT   1
VPI&SU
DEPT OF AERO & OCEAN ENGR
BLACKSBURG VA 24061

PROF MANHAR DHANAK   1
FLORIDA ATLANTIC UNIVERSITY
DEPT OF OCEAN ENGINEERING
777 GLADES RD
BOCA RATON FL 33431-0991

PROF R E FALCO   1
DEPT OF MECH ENG
MICHIGAN STATE UNIVERSITY
EAST LANSING MI 48824

DR HERMANN FASEL   1
UNIVERSITY OF ARIZONA
DEPT OF AERO & MECH ENG
AERO BUILDING 16
TUCSON AZ 85721

PROF JOEL FERZIGER   1
STANFORD UNIVERSITY
DEPARTMENT OF MECH ENG
STANFORD CA 95305

PROF M GAD-EL-HAK   1
AERO AND MECH ENGINEERING
UNIV OF NOTRE DAME
NOTRE DAME IN 46556

DR ARI GLEZER   1
AERO AND MECH ENGR
UNIVERSITY OF ARIZONA
TUCSON AZ 85721

PROF J HARITONIDIS   1
DEPT OF AERO & ASTRO ENGR
OHIO STATE UNIVERSITY
COLUMBUS OH 43212

(2)

DISTRIBUTION (Cont.)

Copies | | Copies

	Copies		Copies
PROF T HODGSON DEPT OF MECH & AERO ENGR NORTH CAROLINA STATE UNIV RAYLEIGH NC 27650	1	HENRY MCDONALD APPLIED RESEARCH LABORATORY PENN STATE UNIVERSITY P O BOX 30 STATE COLLEGE PA 16804	1
DR M HOWE COLLEGE OF ENGINEERING BOSTON COLLEGE 110 CUMMINGTON ST BOSTON MA 02215	1	DR DENNIS MCLAUGHLIN PENN STATE UNIVERSITY DEPT OF AEROSPACE ENG 233 HAMMOND BLVD UNIVERSITY PARK PA 16802	1
MR SRINATH JAYASUNDERA 14146 CASTLE BLVD APT 302 SILVER SPRING MD 20904	1	PROFESSOR W MEECHAM DEPT OF MECH ENGR UNIV OF CALIFORNIA AT LOS ANGELES LOS ANGELES CA 90024	1
DR JOSEPH KATZ JOHNS HOPKINS UNIVERSITY CHARLES AND 34TH STREET MECHANICAL ENG DEPT BALTIMORE MD 21218	1	DR CHARLES MENEVEAU JOHNS HOPKINS UNIVERSITY CHARLES AND 34TH STREET MECHANICAL ENG DEPT BALTIMORE MD 21218	1
DR C VON KERCZEK UNIV OF MARYLAND BALT COUNTY DEPT OF MECHANICAL ENG CATONSVILLE MD 21228	1	PROF PARVIS MOIN DEPT OF MECH ENG STANFORD UNIVERSITY STANFORD CA 94305-4020	1
PROF S J KLINE DEPT OF MECH ENG STANFORD UNIVERSITY STANFORD CA 94305	1	PROF HASSAN NAGIB DEPT OF MECHANICAL ENG ILLINOIS INST OF TECHNOLOGY 10 WEST 32ND STREET CHICAGO IL 60616	1
PROF G C LAUCHLE APPLIED RESEARCH LABORATORY PENN STATE UNIVERSITY P O BOX 30 STATE COLLEGE PA 16804	1	PROF STEVEN ORSZAG PRINCETON UNIVERSITY MECH & AERO ENGINEERING FORRESTAL CAMPUS PRINCETON NJ 08544	1
PROF PATRICK LEEHEY MASS INSTITUTE OF TECHNOLOGY DEPT OF OCEAN & MECH ENG CAMBRIDGE MA 02139	1	PROF RONALD PANTON MECH ENGINEERING DEPT THE UNIVERSITY OF TEXAS AUSTIN TX 78712	1
DR RICHARD LEUPTOW DEPT OF MECH ENG NORTHWESTERN UNIVERSITY 2145 SHERIDAN RD EVANSTON IL 60208	1	DR PABLO PENAFIEL 1713 URBY DRIVE CROFTON MD 21114	1
PROFESSOR J LUMLEY SIBLEY SCHOOL OF MECHANICAL AND AEROSPACE ENGINEERING CORNELL UNIVERSITY ITHACA NY 14853	1	PROF DONALD ROCKWELL DEPT OF MECH ENGINEERING LEHIGH UNIVERSITY BUILDING NO 19 BETHLEHEM PA 18015	1

(3)

DISTRIBUTION (Cont.)

	Copies		Copies

DR W SAUNDERS — 1
VPI&SU
DEPT OF MECH ENG
BLACKSBURG VA 24061-9632

DR CHAO SHI — 1
FLORIDA ATLANTIC UNIVERSITY
P O BOX 3091
BOCA RATON FL 33431-0991

PROF ROGER SIMPSON — 1
VPI&SU
DEPT OF AERO & OCEAN ENG
BLACKSBURG VA 24061-9632

DR CHARLES SPEZIALE — 1
BOSTON UNIVERSITY
DEPT OF AERO & MECH ENG
110 CUMMINGTON ST
BOSTON MA 02215

PROF KYLE SQUIRES — 1
UNIVERSITY OF VERMONT
DEPT OF MECH ENG
201 VOTEY BUILDING
BURLINGTON VT 05405-0156

PROF TIMOTHY WEI — 1
DEPT OF MECH ENG
RUTGERS UNIVERSITY
PO BOX 909
PISCATAWAY NJ 08855

PROF F WHITE — 1
DEPT OF MECH ENG
UNIVERSITY OF RHODE ISLAND
KINGSTON RI 02881

DR KRAIG WINTERS — 1
UNIVERSITY OF WASHINGTON
1023 NE 40TH STREET
SEATTLE WA 98105-6698

DR ISRAEL WYGNANSKI — 1
UNIVERSITY OF ARIZONA
AERO & MECH ENGINEERING
TUCSON AZ 85721

Non-DoD - EXCONUS
PROFESSOR MAX BULL — 1
DEPT OF MECH ENGINEERING
UNIVERSITY OF ADELAIDE
ADELAIDE SA 5000
AUSTRALIA

PROFESSOR DG CRIGHTON — 1
DAMTP
UNIVERSITY OF CAMBRIDGE
SILVER STREET
CAMBRIDGE CB3 9EW
ENGLAND

DR ERIC MANOHA — 1
OFFICE NATIONAL D'ETUDES ET DE RECHERCHES
AEROSPATIALES
29 AVENUE DE LA DIVISION
LECLERC
923220 CHATILLON FRANCE

PROFESSOR JA ASTOLFI — 1
UNIVERSIT, D'AIZ-MARSEILLE II
INSTITUT DE M,CANIQUE DES FLUIDES DI
MARSEILLE
UM 34 DU CNRS
1 RUE HONNORAT 13003
MARSEILLE FRANCE

PROFESSOR BE FORESTIER — 1
UNIVERSIT, D'AIZ-MARSEILLE II
INSTITUT DE M,CANIQUE DES FLUIDES DI
MARSEILLE
UM 34 DU CNRS
1 RUE HONNORAT 13003
MARSEILLE FRANCE

DR CGIANGRECO — 1
CERDSN
DIRECTION DES CONTRUCTINS NAVALES LE
BRUSC
83140 SIX FOURS LES
PLAGES FRANCE

DR PHILIPPE OLIVERO — 1
AERO TOULON
ALLEE J GIONO CHEMIN DE LERY
83500 LA SEYNE SUR MER
FRANCE

DR A JOHANSSON — 1
DEPT OF MECHANICS
ROYAL INSTITUTE OF TECHNOLOGY
S-100 44
STOCKHOLM SWEDEN

PROFESSOR J FFOWCS WILLIAMS — 1
DEPARTMENT OF ENGINEERING
CAMBRIDGE UNIVERSITY
TRUMPINGTON ST
CAMBRIDGE CB2 1 PZ
UNITED KINGDOM

INTERNAL

CODE 01	(R METREY)	1		CODE 722	(A LUNA)	1
CODE 01B	(M SEVIK)	1		CODE 725	(P SHANG)	1
CODE 54	(W FALLER)	1		CODE 725	(K BEER)	1
CODE 54	(J GORSKI)	1		CODE 725	(G CARROLL)	1
CODE 54	(T HUANG)	1		CODE 725	(L COLE)	1
CODE 54	(Y LEE)	1		CODE 725	(M CRAUN)	1
CODE 54	(W MORGAN)	1		CODE 725	(T FARABEE)	1
CODE 54	(F PETERSON)	1		CODE 725	(F FARMER)	1
CODE 54	(W SMITH)	1		CODE 725	(F GEIB)	1
CODE 542	(T FU)	1		CODE 725	(J GERSHFELD)	1
CODE 54	(C SUNG)	1		CODE 725	(J GONZALES)	1
CODE 542	(M GRIFFIN)	1		CODE 725	(L GREGA)	1
CODE 652	(H GARALA)	1		CODE 725	(K JONES)	1
CODE 70	(P KOVICH)	1		CODE 725	(S KIM)	1
CODE 701	(G SMITH)	1		CODE 725	(M KIM)	1
CODE 7015	(D VENDITTIS)	1		CODE 725	(E LEIBOLT)	1
CODE 7015	(S FISHER)	1		CODE 725	(M LEIBOLT)	1
CODE 7015	(R HAMLEY)	1		CODE 725	(L LOUIE)	1
CODE 7016	(G SZILAGYI)	1		CODE 725	(L LUCENA)	1
CODE 7018	(M MONTROLL)	1		CODE 725	(L MAGA)	1
CODE 7020	(M STRASBURG)	1		CODE 725	(J NIEMIEC)	1
CODE 7030	(G MAIDANIK)	1		CODE 725	(M O'LEARY)	1
CODE 7051	(W BLAKE)	1		CODE 725	(E O'NEIL)	1
CODE 7052	(D FEIT)	1		CODE 725	(L O'NEIL)	1
CODE 7053	(Y LIU)	1		CODE 725	(G RAPPL)	1
CODE 712	(T THOMPSON)	1		CODE 725	(S RUSSELL)	1
CODE 713	(C SHERWOOD)	1		CODE 725	(J SU)	1
CODE 713	(W BAICK)	1		CODE 725	(R SZWERC)	1
CODE 713	(A GONZALES)	1		CODE 725	(R VASUDEVAN)	1
CODE 713	(T JOYNT)	1		CODE 725	(J VIGNALI)	1
CODE 713	(M PINTO)	1		CODE 725	(D WARWICK)	1
CODE 72	(J KING)	1		CODE 725	(P ZOCCOLA)	1
CODE 7200	(C WELLER)	1		CODE 731	(M STOCKMAN)	1
CODE 7200	(M RUMMERMAN)	1		CODE 732	(M CHO)	1
CODE 7200	(Y HWANG)	1		CODE 732	(M MALO)	1
CODE 722	(K LEWIS)	1		CODE 734	(R WASSERMAN)	1